

Unveiling the Reddest Galaxies in the Universe with VIDEO and Spitzer

Author:

George Douglas REAVLEY

Supervised by:

Dr. Daniel Smith

PRIMARY SUPERVISOR

Prof. Martin Hardcastle

Dr. Matt Jarvis

SECONDARY SUPERVISORS

Centre for Astrophysics Research
School of Physics, Astronomy and Mathematics
University of Hertfordshire

*Submitted to the University of Hertfordshire in partial fulfilment of the requirements of
the degree of Masters by Research in Astronomy.*

November 2016

Abstract

We used data from the *Visible and Infrared Survey Telescope for Astronomy Deep Extragalactic Observations* (VIDEO) Survey and from the *Spitzer* Extragalactic Representative Survey (SERVS) to generate a sample of Extremely Red Galaxies (ERGs) with colours $H - [4.5] > 4$, by matching H-band (with a bandpass centred on $1.65\mu m$) near-infrared data, and $4.5\mu m$ mid-infrared data. Using optical data from the *Canada-France-Hawaii Telescope* Legacy Survey (CFHTLS) and a pre-release of data from the *European Southern Observatory* Spitzer Imaging Extragalactic Survey (ESIS), extra wavelength bands covering each of the sources in our sample was assembled to increase the wavelengths available. Through the use of Le Phare, a photometric redshift, spectral energy distribution, fitting code, we calculated the probabilities of many different models across a range of redshifts (z) and extinctions (A_V) for these sources, along with what type of model, be it QSO or Galaxy, was the best fit for them. The sample constructed was ~ 3.75 magnitudes brighter than the ERGs previously explored in previous work by Caputi et al. (2012) and were at lower redshifts ($0.4 < z < 3.0$). The sample was also found to be primarily modelled by QSO templates. Using data from the *Herschel* Multi-tiered Extragalactic Survey (HerMES), a far-infrared survey, and assuming a specific dust template model, we converted the $250\mu m$ fluxes to a total infrared luminosity, and then used a standard calibration to convert this to the Star Formation Rate (SFR) for each source. These SFRs were very variable, with one source at $\sim 0 M_{\odot}yr^{-1}$ and one even greater than $1000 M_{\odot}yr^{-1}$. We used all of this information to determine the probabilities of each possibility, and their reliability. We also discussed the best fit solutions and if we can trust them, including the importance of the optical data for deriving reliable source properties. We then related our sample of sources to similar ERGs in the literature before finishing with a simulation calculation to estimate how many galaxies with our chosen colour we would expect to see in the area of sky investigated. It was found that current semi-analytical models such as Henriques' work, based on the Millenium Simulation (Henriques et al., 2009), predicts an ERG density ~ 54 times less than that found in this work. Finally we discuss a potential for follow up work, including different SED fitting techniques, an extra sample of templates, and spectroscopic follow-up.

Declaration

I declare that no part of this work is being submitted concurrently for another award of the University or any other awarding body or institution. This thesis contains a substantial body of work that has not previously been submitted successfully for an award of the University or any other awarding body or institution.

Except where indicated otherwise in the submission, the submission is my own work and has not previously been submitted successfully for any award.

Acknowledgements

The authors would like to thank Shaun Read, Ryan Cheale, Chris Haynes, and Gareth Martin for productive discussions, as well as their family and friends for support throughout the Masters.

Contents

Abstract	i
Acknowledgements	iii
Contents	iv
1 Introduction	1
1.1 Redshift and the Epoch of Reionization	1
1.2 Photometric Redshift Estimation and Spectral Energy Distributions	2
1.3 Magnitude and Extinction Laws	4
1.4 Colour and Galaxy Selections	7
1.5 Structure	10
2 Surveys	14
2.1 Main Survey data used in this Study	14
2.2 Extra Survey data used	15
2.3 Star Formation	16
3 Sample Selection	18
3.1 VIDEO and SERVS Matching	18
3.2 Detection of ERGs	22
3.3 Optical Matching	23
3.4 Herschel Matching	23
4 Estimating Redshifts and other Characteristics	25
4.1 Le Phare	25
4.1.1 Templates	25
4.1.2 Extinction	26
4.1.3 Extra Parameters	27
4.2 Running Le Phare	28
4.3 Output	28
4.4 Star Formation Rates	29
5 Results	31
5.1 Notes on Individual Objects	34
5.1.1 XMM 1	34
5.1.2 XMM 2	38

5.1.3	XMM 3	41
5.1.4	XMM 4	44
5.1.5	XMM 5	47
5.1.6	XMM 6	50
5.1.7	ES1 1	53
5.1.8	ES1 2	56
5.1.9	CDFS 1	59
6	Discussion	62
6.1	What are the Reddest Galaxies in the Universe?	62
6.2	Redshifts and Extinctions	63
6.3	Star Formation Rate	66
6.4	Investigation of the Usefulness of the Optical Data	67
6.5	Extinction Laws	68
7	Simulations	70
7.1	Query	70
7.2	Findings	71
8	Conclusions	72
9	Future Work	74
	Appendices	75
	Bibliography	80

Chapter 1

Introduction

1.1 Redshift and the Epoch of Reionization

One of the fundamental tools used by astronomers to investigate distant galaxies in the universe is redshift, with the total generated from three separate contributions. The most common is the relativistic doppler shift, given by:

$$z + 1 = \sqrt{\frac{1 + \frac{v}{c}}{1 - \frac{v}{c}}} \quad (1.1)$$

where z is the redshift, and v and c the speed of the source and the speed of light respectively. This is due to the relative motion of the object, with movement away leading to a redshift and a movement towards (such as the galaxy Andromeda) giving a blueshift.

The second contribution to total redshift is equally as important; called the cosmological redshift:

$$z + 1 = \frac{a_o}{a(t)} \quad (1.2)$$

where a_0 and $a(t)$ are the scale factors at the current (taken as 1 for the present) and observed time, a value that measures the expansion factor of the universe (Serjeant, 2010). This version of redshift is caused by the expansion of the universe, and is a by-product of distance alone.

The final potential contribution to the redshift of a source is called the gravitational redshift, and is the reddening of light when it escapes from a gravitational well, such as a black hole or a highly compact galaxy (Pound and Rebka, 1960).

All these contributions to the redshift of a source can be measured with the following equation:

$$z + 1 = \frac{\lambda_o}{\lambda_e} \quad (1.3)$$

with λ_o and λ_e the observed and emitted wavelengths of the source respectively.

Probing into the early universe is important for understanding how the first galaxies were formed. In the very beginning, the universe was too hot and energetic for protons to capture electrons (forming neutral hydrogen). After about 370,000 years the universe had expanded and sufficiently cooled for recombination to occur. From then the universe was completely neutral and transparent. After about 400 million years, the first stars began to form, ionising bubbles of hydrogen forming HII regions. After about 1 billion years reionization was complete, thought to happen at around $z \sim 6$. The techniques used in this study could potentially find galaxies within the epoch of reionization ($z \geq 6$). It is important to investigate galaxies within this epoch as they give us insight into how galaxies formed and evolved.

1.2 Photometric Redshift Estimation and Spectral Energy Distributions

Redshift is a fundamental characteristic of distant galaxies, and by assuming a cosmology we can estimate other properties. These assumptions are the Hubble constant H_0 , which can relate distance to recession velocity for very local sources, and the universe's matter and dark-energy fractions; Ω_M and Ω_Λ respectively. Assuming values for these constants enables us to infer physical properties of the sources, such as galaxy type, mass and luminosity, rather than just the apparent brightness and angular size. To determine the redshift of distant galaxies it is common to study the spectra of light emitted. A spectrum is a continuum of fluxes over a specific wavelength range, as shown in Figure 1.1. Measuring a spectrum of a faint star or galaxy requires a long observation time, whereas a large bandwidth of photometric observations enables the detection of much fainter sources in shorter time-scales. This is because the comparatively large resolution of spectrographs relative to broadband photometry means that the photons detected are spread out, reducing the signal to noise ratio in an individual resolution element. Deep surveys such as VIDEO (Jarvis et al., 2013) and SERVS (Mauduit et al., 2012), only have photometric data for every source, which when plotted against wavelength, give a spectral energy distribution (SED). To estimate redshifts for the high redshift galaxies that we are looking for, we will implement a template fitting method using a program called PHotometric Analysis for Redshift Estimations (Le Phare, Arnouts et al., 1999; Ilbert et al., 2006). This works by fitting thousands of SED templates, including galaxies, active galactic nuclei (AGN) and stars, onto the photometric data for a given source. Le Phare identifies the best fit template primarily as

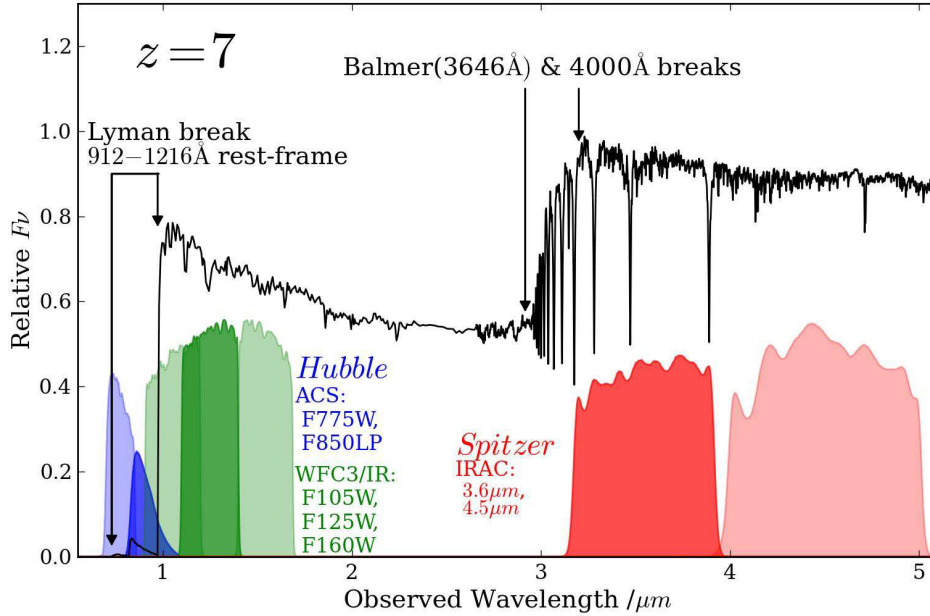


FIGURE 1.1: Graph of relative flux against observed wavelength for a redshift 7 galaxy depicting the Lyman, Balmer and 4000 Å breaks, further discussed in section 1.3. The blue and green shaded areas at the bottom are bands used in the Hubble Space Telescope, showing a similar wavelength range to the Near-Infrared wavebands used in this work, while the red areas are from the Spitzer Space Telescope (bands that are used in this paper). This figure is reproduced from Dunlop (2013).

a function of redshift, but also of other properties such as dust attenuation (discussed in §1.3), using the chi squared (χ^2) minimising technique, given by:

$$\chi^2 = \sum_{i=1}^n \frac{(O_i - E_i)^2}{\sigma_i^2} \quad (1.4)$$

where O_i and E_i are the observed and expected fluxes respectively and σ_i is the uncertainty on the flux in the i th band. Chi squared works by minimising the differences between the observed fluxes and the values given by the model weighted with the uncertainty estimate for flux. Instead of selecting the best fit template and returning the corresponding χ^2 value, which can be converted into an individual probability value, Le Phare creates a probability distribution function (PDF) of all the possible redshifts. How Le Phare works, and how it generates these PDFs is discussed in §4.1.

When using photometric data to constrain redshifts, certain features need to be identified in the spectral energy distributions as a featureless model would poorly constrain the redshifts. The first is the Lyman limit break. In neutral hydrogen clouds, electrons can be ionised from the ground state forming hydrogen ions, corresponding to an energy increase of 13.6eV (91.2nm). Star formation in young galaxies produces a lot of ultraviolet light (UV), which has more than

the required energy to excite these electrons. Lyman alpha absorption on the other hand, is the excitation of electrons from the $n = 1$ to $n = 2$ state, again from UV light, at 121.6 nm. As with the Lyman limit break, the absorption takes place in neutral hydrogen clouds. The slight difference however is that while the Lyman limit break is due to absorption near to the star forming regions, Lyman alpha absorption is caused by clouds between the source and the observer. As these clouds are at varying redshifts, it creates a so called forest of absorption lines. Both these absorptions are seen in the bottom left of Figure 1. When studying the spectra of galaxies within the epoch of reionization, the flattening of the Lyman alpha forest (as shown in Figure 1.2 with increasing redshift), gives a good indicator that a galaxy is in this era of the Universe.

The second two breaks occur at much lower energies. The Balmer break is the ionisation occurring from the $n = 2$ energy level (at 3.4 eV). It is significantly smaller than the Lyman limit break as there aren't as much excited hydrogen to ionise. The final break is brought on by an accumulation of absorption lines due to the ionisation of metals such as Calcium and Potassium. It is called the 4000 Å break and is largest in stellar populations that are old and metal-rich. These two breaks are shown in the middle of Figure 1.1.

A final important feature of the spectra of galaxies are other atomic emission and absorption lines, you can see the absorption lines to the right of the 4000 Å break in Figure 1.1, while emission lines are not shown on this plot. These characteristics are used to calculate spectroscopic redshifts for galaxies but could play an important role when calculating the photometric counterpart. How these lines could effect the redshift estimation will be explored later, in §4.1.3

1.3 Magnitude and Extinction Laws

Searching for either the Lyman or 4000Å/Balmer break in the optical/NIR is a powerful way to identify high redshift galaxies based on photometric data. Generally the logarithmic measurement of brightness, magnitude, is used to compare the fluxes from each wavelength band. There are two systems commonly used to calculate magnitude, first is called the Vega Magnitude (Vega mag). This system is a comparison of the target source's brightness and the apparent brightness of the star Vega (defined as having 0.0 magnitude in all wavelength bands). The other magnitude system, the one which we will be using throughout this report, is called AB magnitude (Oke and Gunn, 1983). It is defined as:

$$AB = -2.5 \log_{10} f_{\nu} + 8.9 \quad (1.5)$$

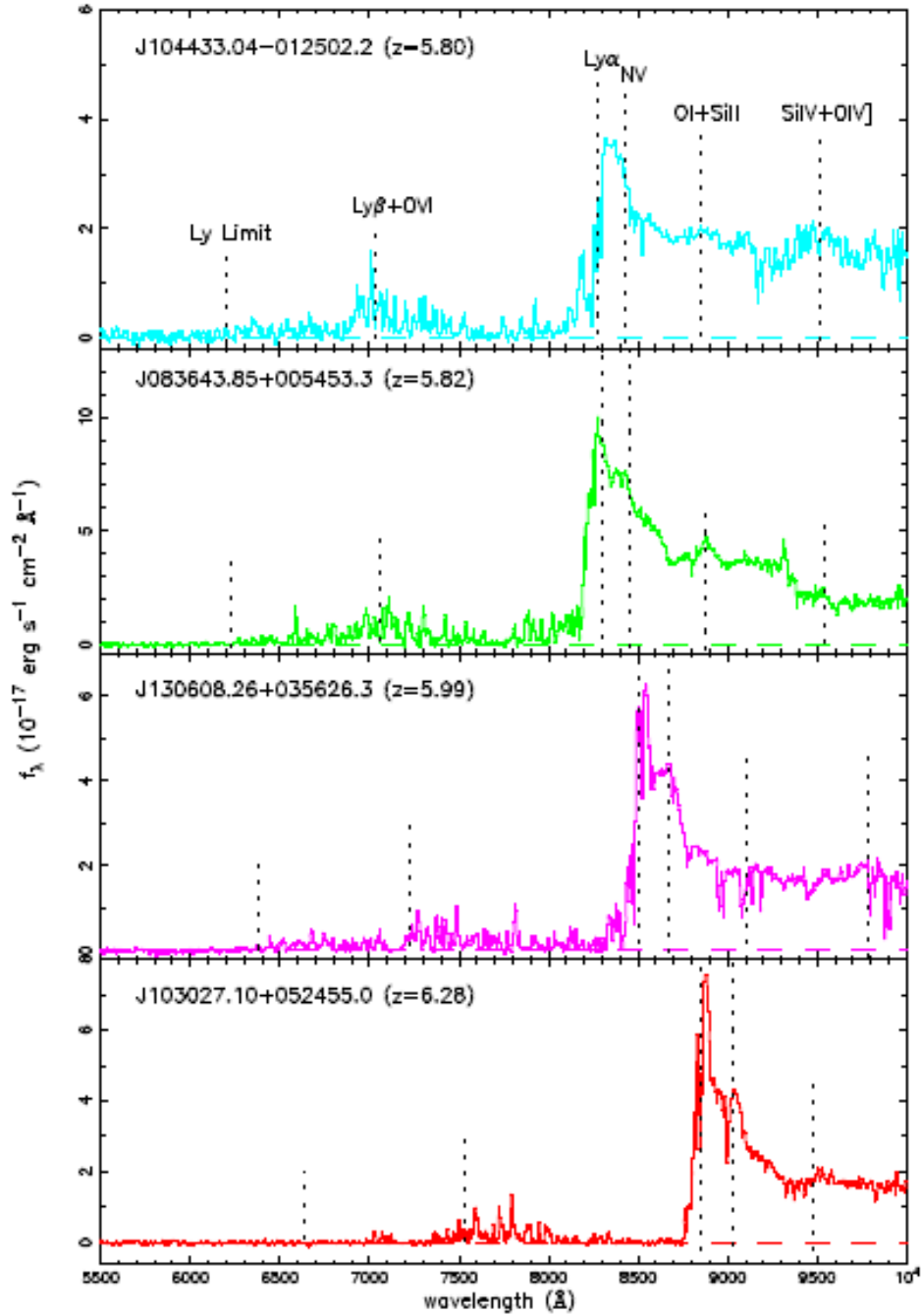


FIGURE 1.2: Optical spectra of 4 quasars reproduced from Becker et al. (2001) shown in flux against wavelength. The ID of each galaxy is shown, with the corresponding redshift, as well as positions of emission lines shown with dashed lines.

where f_ν is the spectral flux density in units of Janskys (Jy), with $1\text{Jy} = 10^{-26}\text{WHz}^{-1}\text{m}^{-2} = 10^{-23}\text{erg s}^{-1}\text{Hz}^{-1}\text{cm}^{-2}$.

Extinction is the dimming of light emitted by galaxies, caused by dust. It is an important characteristic of galaxies to measure, as by not correcting for dust effects you will infer incorrect intrinsic colours, which in turn, will cause calculations of the redshift, luminosities and any other properties to be false. The amount of this dimming has a wavelength dependence because interstellar dust absorbs and scatters blue light more than red light. There are many differing models that describe this dependence, as we can't measure the dust law in distant galaxies. We therefore have to assume a standard law derived from local systems. Five of the most commonly used models are shown in Figure 1.3. These are two Milky Way (MW) extinction laws, where we will be using the Allen MW extinction law (Allen, 1976), rather than the Seaton MW law (Seaton, 1979), as well as the Small Magellanic Cloud (SMC, Prevot et al., 1984) and Large Magellanic Cloud laws (LMC, Fitzpatrick, 1986). The SMC and LMC are dwarf galaxies in the Local Group, their extinction laws are known because they are sufficiently bright and close to the Milky Way for individual stars to be resolved. Looking at Figure 1.3, you can see that the LMC law is very similar to the the Milky Way's, while the SMC is vastly different at wavelengths below $0.5\ \mu\text{m}$, leading to large discrepancies in the optical and UV SEDs. A final law that is often used is the Calzetti extinction law (Calzetti et al., 1994), commonly used to describe high redshift, starburst galaxies, which is potentially the best law for our sample of galaxies. This law follows a similar wavelength dependence, however it gives larger extinction at lower wavelengths and doesn't have the characteristic *bump* (commonly called the $2175\ \text{\AA}$ *bump*) that the other three laws contain (Xiang et al., 2011).

Aside from the extinction laws themselves, it is also important to determine the exact amount of extinction, and hence dust, present in distant galaxies. This amount of reddening is stated as follows:

$$E_{B-V} = (B - V)_{\text{observed}} - (B - V)_{\text{intrinsic}} \quad (1.6)$$

where B and V are the magnitude in the B and V bands. It is important to model the extinction of distant galaxies due to the cause of this reddening; dust in the inter-stellar medium (ISM). Dust blocks out stellar light and permeates throughout all spiral galaxies (as ellipticals are widely thought to be dust free). The discrepancies between the laws that have been observed in our galaxy and neighbouring dwarf galaxies were originally thought to be caused by the different metallicities of the galaxies, as the LMC's and SMC's metallicities are approximately 40% and 10% of the Milky Way's respectively (Gordon et al., 2003). However, more recently the differences are thought to be caused by star-formation, and how the light produced processes dust grains in the ISM. The fact that the Calzetti law doesn't contain the $2175\ \text{\AA}$ bump supports

this, as it models galaxies that are undergoing periods of high star formation, also referred to as star-bursts (Calzetti et al., 2000).

The amount of reddening present is not a straightforward indicator of the total extinction, as mentioned earlier there is a wavelength dependence. The total extinction at wavelength λ is given by the following equation:

$$A_\lambda = A_V k(\lambda) = R_V E_{B-V} k(\lambda) \quad (1.7)$$

where A_V is the explicit extinction of a source (which we will determine in our work), $E(B-V)$ the reddening as shown in Equation 1.6 and $k(\lambda)$ is a function of wavelength for each reddening curve shown in Figure 1.3. R_V is a scaling factor that takes different values depending on the extinction law chosen, 2.72 ± 0.21 for the Small Magellanic Cloud, 4.05 ± 0.80 for the Calzetti Law, and 3.1 for the MW and LMC.

1.4 Colour and Galaxy Selections

Comparing two magnitudes, potentially below and above a specific break (as described in Chapter 1.2), you can produce a colour of a source. Many studies have used this method of ‘‘colour selection’’ to select for a specific type of galaxies.

Important types of galaxies include BzKs, a selection of galaxies based on B, z and K band photometry (with B an extra band at 445 nm), specifically when the colour limit $(z - K)_{AB} - (B - z)_{AB} > -0.2$ is satisfied (Daddi et al., 2004). Each letter corresponds to the magnitude in that waveband. This cut was found to successfully isolate star forming galaxies at *redshift* > 1.4 . Galaxies with $BzK < -0.2$ were split into old, *redshift* > 1.4 galaxies at $(z - K)_{AB} > 2.5$ and *redshift* < 1.4 galaxies $(z - K)_{AB} < 2.5$. Lyman break galaxies (LBGs) are a very popular type of galaxies as they are a very efficient way of identifying high redshift galaxies, they are given by all sources having a large change in brightness between two bands on either side of the Lyman break. Because of this characteristic, many differing colours have been used to search for these. However due to our selection of wavebands we would see a Lyman break between the H and [4.5] bands at a redshift of ~ 15 and ~ 44 , which is infeasible with the depth of the surveys used. It is however probable that we will find sources that generate the extremely red colour due to the Balmer/4000Å break. Franx et al. (2003) employed a $J - K_s > 2.3$ cut on a selection of sources and found many galaxies that they classified as Dusty Red Galaxies (DRGs). Another type of galaxy, called a Dust Obscured Galaxy (DOG) is classified in Hwang and Geller (2013) through a limit on a ratio of fluxes, given by: $S_{9\mu m}/S_{0.22\mu m} > 982$ with S the flux at $9\mu m$ and $0.22\mu m$

respectively. Extremely Red Objects (ERO) are a more specific selection of ERGs. EROs are classified as having a colour $R - K > 6$ (Pierre et al., 2001).

One final type are Extremely Red Galaxies (ERG), and are defined as having $R - K > 5$ or $I - K > 4$ (Pozzetti and Mannucci, 2000). Caputi et al. (2012) described ERGs as being either dusty ellipticals with a redshift range of $0.6 < z < 1.5$ or having a high redshift above 1, by carrying out a colour cut of $H - [4.5] > 4$; producing galaxies at $0.72 < z < 6.3$ ($[4.5]$ is the magnitude from the Spitzer Space Telescope's $4.5\mu\text{m}$ band, as discussed in section §2.1). As discussed through this thesis, this work will follow Caputi et al. (2012), by implementing a similar $H - [4.5] > 4$ colour-cut. Caputi et al. (2012) identified a sample of 17 sources in an area of $\sim 180 \text{ arcminutes}^2$ ($\sim 3 \text{ degrees}^2$), with $H - [4.5] > 4$ using data the HST Cosmic Assembly Near-infrared Deep Extragalactic Legacy Survey, CANDELS (Grogin et al., 2011) and the Spitzer SED (Ashby et al., 2013) survey, and split them up into 3 sub-groups by using photometric information to estimate their redshifts. 11 of their sources were categorised to be at $3 < z < 5$, with extinction values between $1.1 < A_V < 4.2$. The other two sub-groups were at the extremes of redshift and extinction. 4 sources were at redshifts between $0.7 < z < 1$ but had high extinction values of $A_V > 5.0$. The final 2 sources had a low extinction ($A_V \sim 1$) and corresponding redshifts higher than 6. The sub-sampling of these extremely red galaxies showed that a simple colour cut of $H - [4.5] > 4$ is not enough to pick galaxies out to extremely high redshifts (~ 6), especially since the galaxies in the final sub-group had a colour $4 < H - [4.5] < 4.3$. Caputi et al. (2012) suggested an additional colour-colour selection on their sample that could potentially be used to identify high redshift ERGs. They found that the two $z > 6$ sources lay in a region corresponding to $H - K_s \lesssim 1.7$ and $K_s - [3.6] \gtrsim 2.1$, as shown in Figure 1.4. ERGs are a population of galaxies that have not been widely investigated and as will be discussed in Section 2.1, they have not been found in such a wide survey. Finding these sources is important for generating an unbiased view of galaxy evolution over all redshifts, especially since it has been shown that these galaxies could be at very high redshifts, potentially within the epoch of reionization. Comparing these ERGs to the density generated by current semi-analytical simulations can also give an indication on how well our models of galaxy formation since the Big Bang can predict these highly irregular sources.

A more recent study by Wang et al. (2015) employed a $H - [4.5] > 2.25$ colour cut on 350 arcmin^2 of data from the Great Observatories Origins Deep Survey, GOODS (Dickinson et al., 2003). This uses the same colour that we will be carrying out, but with a different limit. They classified their data into two groups called *JH-red* and *JH-blue*, splitting the sources through a cut in the colour-colour plot of $H - [4.5]$ against $J - H$, as shown in Figure 1.5. It was shown that galaxies in the *JH-blue* section were generally at $z > 3$. Wang considered that the $H - [4.5] > 4.0$ cut carried out in the Caputi study could potentially miss high redshift sources, due to the position and/or strength of the 4000 \AA break. Figure 1.6 depicts 3 different galaxy SEDs, all

¹http://webast.ast.obs-mip.fr/hyperz/hyperz_manual1/node10.html

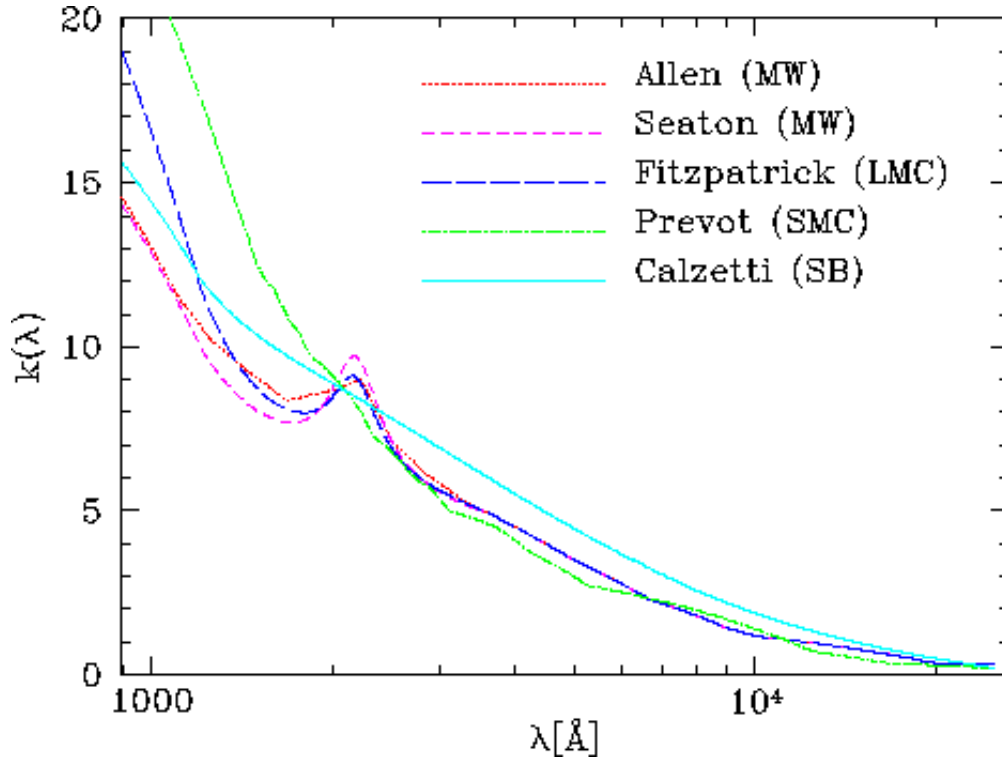


FIGURE 1.3: Plot showing the average extinction curves for the 5 most common extinction laws, in $k(\lambda)$ against wavelength in angstroms (\AA). The laws are as follows, both the Allen and Seaton laws for the Milky Way, the Fitzpatrick law for the Large Magellanic Cloud, the Prevot law for the Small Magellanic Cloud, and finally the Calzetti Law that models high redshift sources (here SB stands for Starburst). Taken from the website for a similar photometric fitting code, *hyperz*¹.

with a similar $H - [4.5]$ colour. The blue SED shows a star-forming galaxy at redshift 3.5, the yellow SED an extremely dusty redshift 2.5 galaxy, and the red SED a passive/old galaxy at redshift 3.5. As mentioned before, an additional $J - H$ colour was used to split up high and low redshift sources. It is important to note, however, that this extra cut was only used to distinguish between sources above and below redshift 3, and it does not address the feasibility of the high redshift *box* in Figure 1.4. Note also that in Figure 1.6 reproduced from Wang et al. (2015), the yellow galaxy template is considered to be extremely dusty, with an A_V value of 0.6.

Caputi et al. (2012) showed that redshift and extinction (A_V values) relate to each other. Figure 1.7 shows examples from their SED fitting results in the redshift - A_V plane, with 1, 2 and 3 σ confidence lines shown with black solid lines around the minimum solutions. The bottom left sub-plot only has one best fit solution for redshift and extinction, however the other 3 examples (especially the sub-plots on the right) show a potential inverse-correlation between the two variables. When a source produced two best fits, there was a low redshift, high extinction solution, as well as a high redshift, low extinction solution, leading to the conclusion that there is a potential inverse relation. A galaxy with an extinction value greater than 1 is considered to be highly obscured, however as Caputi et al. (2012) showed it is important to consider A_V values up to 8.0.

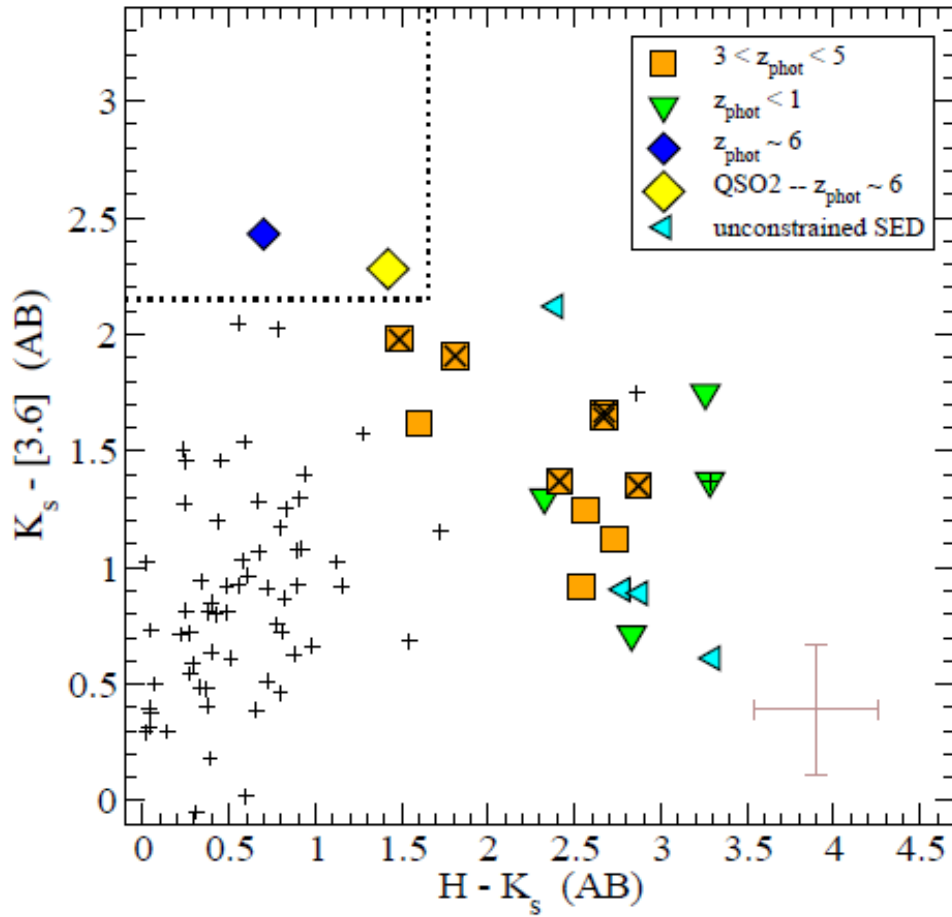


FIGURE 1.4: Colour-colour plot reproduced from Caputi et al. (2012) of $K_s - [3.6]$ against $H - K_s$. The dotted lines in the top left corner identifies a possible area that could identify $z > 6$ galaxies. The small plus-like symbols are IRAC power-law AGN, while the other symbols are part of the Caputi sample (Identified in the legend and discussed in §1.4).

1.5 Structure

This thesis will be structured as follows: in Chapter (§) 2 we will first discuss all the surveys and data, both optical and infrared, that are used to generate our sample of ERGs, as well as how the extra data (optical and far-IR) will be used in our work, more specifically as Star Formation Rate estimators. Chapter 3 will show how we generated our sample, paying particular interest to how the surveys were matched together and how we limited our sources to the galaxies with the properties we are investigating. Chapter 4 will be focused on Le Phare, the photometric SED fitting method used in this study, along with the parameters chosen and the output characteristics. We will then move onto the results in Chapter 5, and the discussion in Chapter 6. We will talk about how we investigated the simulations in Chapter 7, and any results that were found, before finally exploring the conclusions and ideas for future work in Chapters 8 and 9. Throughout this study we will use the AB magnitude system as discussed, and a standard cosmology with $H_0 = 70 \text{ km s}^{-1} \text{ Mpc}^{-1}$, $\Omega_M = 0.3$, and $\Omega_\Lambda = 0.7$

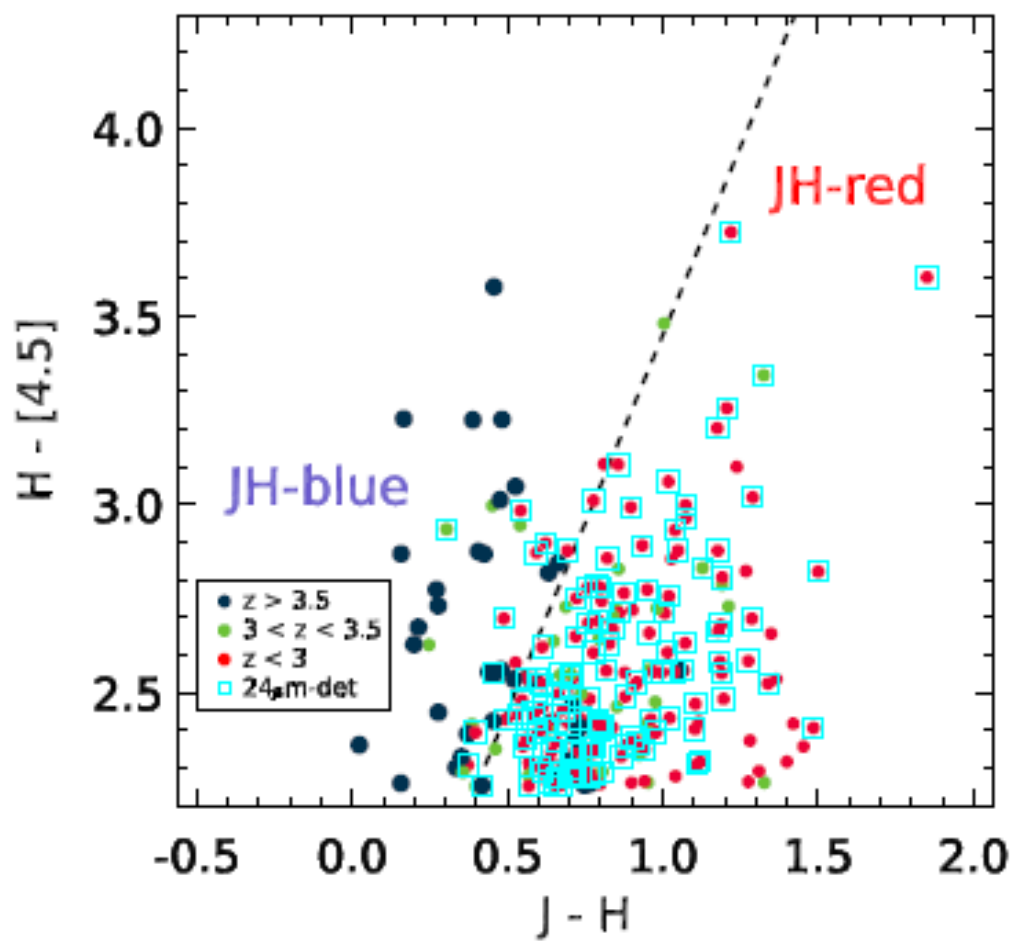


FIGURE 1.5: Colour-colour plot of $H - [4.5]$ against $J - H$, reproduced from Wang et al. (2015). The dashed line show the cut that was implemented to separate JH-blues and JH-reds, further discussed in §6.2. The redshift of all sources are shown by the colour and type of marker, as shown in the legend.

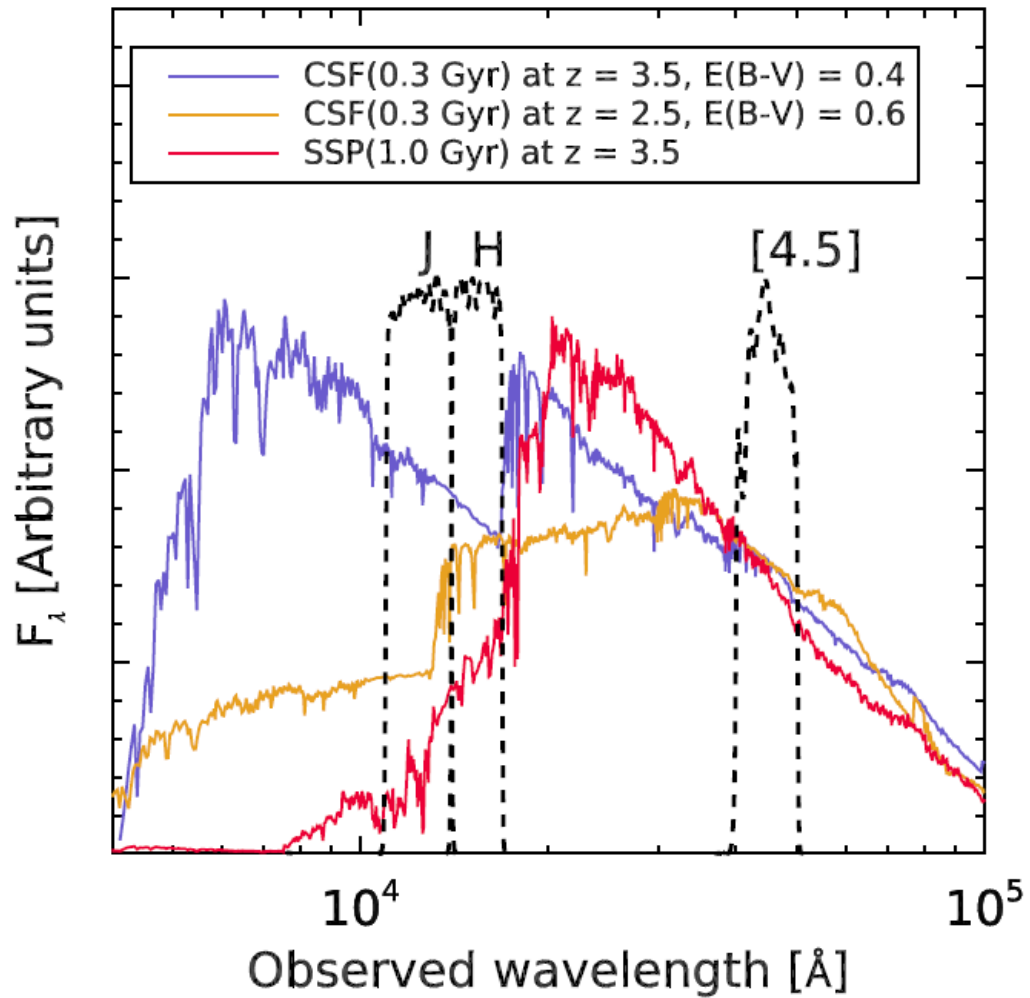


FIGURE 1.6: Example SEDs in normalised flux against wavelength, reproduced from Wang et al. (2015), of a $z = 3.5$ star-forming galaxy, a $z = 2.5$ extremely dusty galaxy, and a $z = 3.5$ passive/old galaxy, depicted in blue, yellow, and red respectively. The J, H, and [4.5] (i.e. B2) filter curves are also shown.

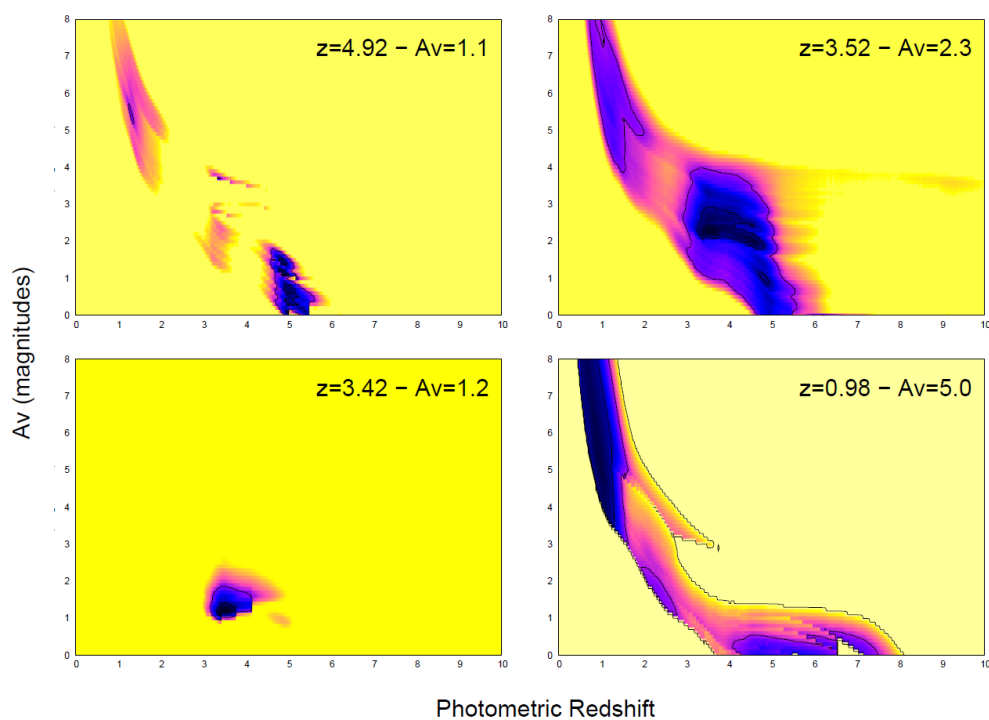


FIGURE 1.7: Example solutions in the redshift - extinction ($z_{phot} - A_V$) plane, reproduced from Caputi et al. (2012). The best fit solution, shown in the top right of each sub-plot, are surrounded by 1, 2 and 3 σ confidence levels. All sources are as constrained by Caputi, $H - [4.5] > 4.0$ galaxies. The colours represent the probability of the $z - A_V$ plane, however there was no bar present in the paper.

Chapter 2

Surveys

2.1 Main Survey data used in this Study

This work primarily makes use of The Visible and Infrared Survey Telescope for Astronomy (VISTA, Emerson et al., 2004) Deep Extragalactic Observations (VIDEO) survey (Jarvis et al., 2013), a ~ 12 degree² survey in the near-infrared (NIR). The five bands included are Z, Y, J, H and K_s with peak wavelengths (in μm) of 0.88, 1.02, 1.25, 1.65, and 2.2 respectively, and 5σ depths of 25.7, 24.6, 24.5, 24.0, and 23.5 AB. The VIDEO survey was split up across three of the most commonly used high-Galactic-latitude fields. Three tiles in the XMM-Newton Large Scale Structure field (XMM) over approximately 4.5 degrees² (XMM 1, 2 and 3), two tiles in the ELAIS-S1 field covering approximately 4.5 degrees² (ES1 North and South) and three tiles in the extended Chandra Deep Field South covering approximately 3 degrees² (CDFS 1, 2 and 3).

For two extra photometric bands, we will use the Spitzer (Werner et al., 2004) Extragalactic Representative Volume Survey (SERVS, Mauduit et al., 2012) another NIR survey which overlaps the XMM, ES1 and CDFS fields. These two bands are at 3.6 μm and 4.5 μm respectively with both going to a depth of 23.1 AB, giving us the required bands to carry out the $H - [4.5]$ selection. These two bands come from the Infrared Array Camera (IRAC) on the Spitzer Space Telescope, which can also take images in two mid-infrared (MIR) bands at 5.8 and 8.0 μm , however the XMM, ES1 and CDFS fields were not covered by these wavelengths so we are unable to make use of these bands.

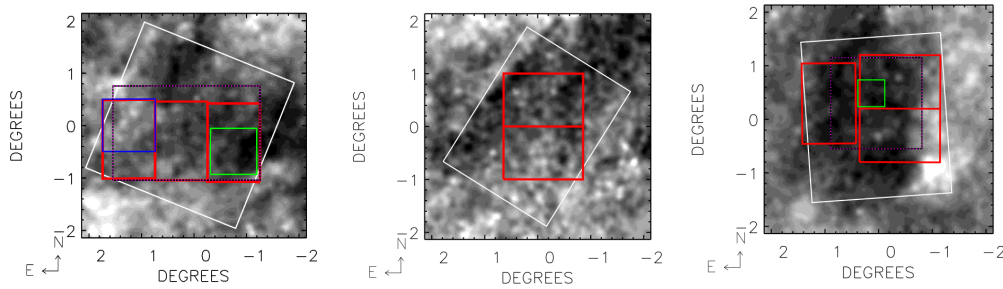


FIGURE 2.1: Infrared Space Observatory (ISO, Kessler et al., 1996), XMM, ES1 and CDFS from the left to the right. The white squares show Spitzer-Space-Telescope Wide-area Infrared Extragalactic (SWIRE, Polletta et al., 2006) imaging data, while the red square show the locations of the VIDEO overlap. For the XMM map, the blue square is the CFHTLS-D1 field (an optical survey) and the green square is the UKIDSS-UDS field (another NIR survey, Lawrence et al., 2007) which could give more data for specific sources. The small green square on the CDFS map is an optical survey called COMBO-17 (Wolf et al., 2001), which again could have overlap for some sources. These maps are reproduced from the VIDEO survey page on the Oxford University website. ²

2.2 Extra Survey data used

It used to be common practice to exclusively use data from one specific wavelength regime, and due to the fact that both VIDEO and SERVS are NIR surveys, they don't offer a very wide wavelength range. Due to the multitude of new surveys covering the same fields in vastly different wavelengths, it is now possible to use a large number of different wavelengths for the same sources. The XMM field has an optical counterpart called the Canada-France-Hawaii Telescope Legacy Survey (CFHTLS ³), covered by the Wide 1 (W1) field (there is deeper part of this survey, D1, however this covers a very small area of the sky and our sample of sources were not covered by this field). Using this survey enables us to obtain more photometry for our sample, leading to more accurate photometric redshifts, as we will demonstrate in later sections. The bands that this survey will add are u, g, r, i, z, and have effective wavelengths of 0.374, 0.487, 0.625, 0.770 and 0.89 μm and depths of 26.0, 26.5, 25.9, 25.7, and 24.6 AB (the z band is actually at the same wavelength as the the Z band in the VIDEO survey, but has a different filter curve so will offer extra data for each galaxy). These data could be potentially very useful because, as mentioned earlier, the four most common extinction laws differ the most at optical wavelengths. Using extra data will also help to constrain the redshifts that will be determined.

While there were many optical surveys that covers the XMM field, data is limited for the CDFS and ES1 fields. Through private communication with Mattia Vaccari, we were allowed access to a pre-release of optical data that covers the ES1 field. The European Southern Observatory ⁴ Spitzer Imaging Extragalactic Survey (ESIS, Berta et al., 2008) is the optical follow up of SWIRE in the ES1 field. This survey used 3 wavelength filter curves, b123, v89, and r162 (hereby referred to as b, v, and r) with central wavelengths of 0.451, 0.539, and 0.651 μm and

depths of 25.0, 25.0, and 24.5 AB. These extra data will be used for the same reasons as the above CFHTLS data, potentially further constraining our sample of ES1 sources.

The final data that we will use during this study is from a Far-IR survey called the Herschel Multi-tiered Extragalactic Survey (Oliver et al., 2012, HerMES) adding a potential 3 more flux values to use at $250\mu\text{m}$, $350\mu\text{m}$ and $500\mu\text{m}$ (henceforth referred to as H1, H2, and H3). The spatial resolution at $250\mu\text{m}$ is $18''$ Full Half Width Maximum (FWHM) compared to $< 0.9''$ in VIDEO and is therefore of much worse quality, however it covers all three fields of the VIDEO survey, so it could allow us to carry out more calculations on all potential extremely red galaxies.

2.3 Star Formation

Star formation rate (SFR) is an important characteristic of galaxies, measured in $M_{\odot}\text{yr}^{-1}$, the number of solar masses per year. It is used to trace a galaxy's history, as well as its potential future. There are a few simple ways to estimate the SFR of a galaxy and we will explore two methods based on emitted stellar light in 2 common wavelength regimes. The first is based on direct stellar light emitted in the Ultra Violet (UV) rest frame ($< 0.3\mu\text{m}$) which can be redshifted and observed at optical wavelengths ($< 1.5\mu\text{m}$). This regime is primarily used to study young stellar populations, commonly known as O and B stars (Walborn, 1990), as they are known to emit most of their energy at these wavelengths, over time-scales of $\approx 100 - 300$ Myrs (Calzetti et al., 2004). This method is the best at inferring the SFR of a galaxy, however it only works in the absence of dust attenuation, due to the dimming of light by extinction. This UV light would be redshifted up to the optical wavelengths taken from CFHTLS (for example at redshift $z = 3$ the g band is the observed flux from the rest frame UV), however it would be less likely to give an accurate SFR as the dust attenuation leads to a lower signal-to-noise ratio of these fluxes, generating an unreliable determination of SFR. Also due to the potentially uncertain redshifts of the sources in our sample, and the fact that the rest frame UV spectrum varies rapidly with wavelength, any star formation rates calculated could be fundamentally inaccurate. One final issue is that in calculating the SFR you need to measure the intrinsic luminosity, and correcting using the short wavelengths (optical and near-IR) can be very hard due to large effect of dust, even if you have a very high signal-to-noise ratio.

The second wavelength regime that can be used to determine SFRs is mid-IR to far-IR at wavelengths between $8 - 1000\mu\text{m}$. Instead of observing the stellar light directly, as above, when using these longer wavelengths, you actually make use of the dust-processed light. This infrared luminosity obviously depends on the dust content, as well as how much the stars heat up the

²<http://www-astro.physics.ox.ac.uk/~video/public/Home.html>

³<http://www.cfht.hawaii.edu/en/news/CFHTLS/>

⁴<http://www.eso.org/public/about-eso.html>

dust (Helou, 1986). Dust can be heated by two different stellar populations, a UV-luminous, young population that generates an IR spectrum which has a peak at a rest-frame wavelength of $\approx 60\mu\text{m}$, or a UV-faint, old population producing a peak at $\approx 100 - 150\mu\text{m}$ (Helou, 1986). Depending on the redshift of the sources in our sample, we could make use of the Herschel bands (as discussed later) to estimate the SFR. An observed wavelength of 250, 350 and 500 μm corresponds to a redshift of 3.2, 5.8 and 7.3 if emitted at $60\mu\text{m}$, which could be the potential redshift range of the extremely red galaxies.

Chapter 3

Sample Selection

3.1 VIDEO and SERVS Matching

The first step in this work was to match the VIDEO survey and SERVS catalogues for the XMM field (as this is the most complete in VIDEO at the time of writing). Figure 2.1 shows the overlap of VIDEO and SERVS for all three fields, as well as the current optical coverage (not including the pre-release of the ESIS data). The program Tools for Operations on Catalogues and Tables (TOPCAT, Taylor, 2005) matches the Right Ascension (RA) and Declination (Dec) using a best symmetrical match method. However, it is important to choose the maximum separation between VIDEO and SERVS co-ordinates, to ensure a source in the one catalogue is not matched to an undetected source in the other catalogue. By setting the matching method to *All Matches* and a maximum separation of 5 arcseconds, we obtained the histogram shown in Figure 3.1.

To determine if the sources in the VIDEO and SERVS catalogues gave a real match, we made use of the data generated when matching with a maximum separation of 5 arcseconds, as shown in Figure 3.1. The false matches are shown by the gradient of matches at the right of the histogram. We decided to fit a quadratic model to the false matches ($N_{false} = Ax^2 + Bx + C$, where N_{false} is the number of false matched sources in the bin, x is the separation, and $A/B/C$ are constants), with an initial constraint that there must be 0 false matches at 0 arcseconds i.e. $C = 0$. We measured these constants by minimising the chi-squared generated between the observed separations and those generated through the model, between 2.0 and 5.0 arcseconds, as also described in §1.2. To determine the maximum separation to use when matching the two catalogues we made use of this model, by choosing a value at which there is an equal amount of real matches as false matches. Looking at Figure 3.1, we can see the example model calculated for XMM ($N_{false} = 115x^2 + 71x$), giving us a separation to use of 1.2 arcseconds.

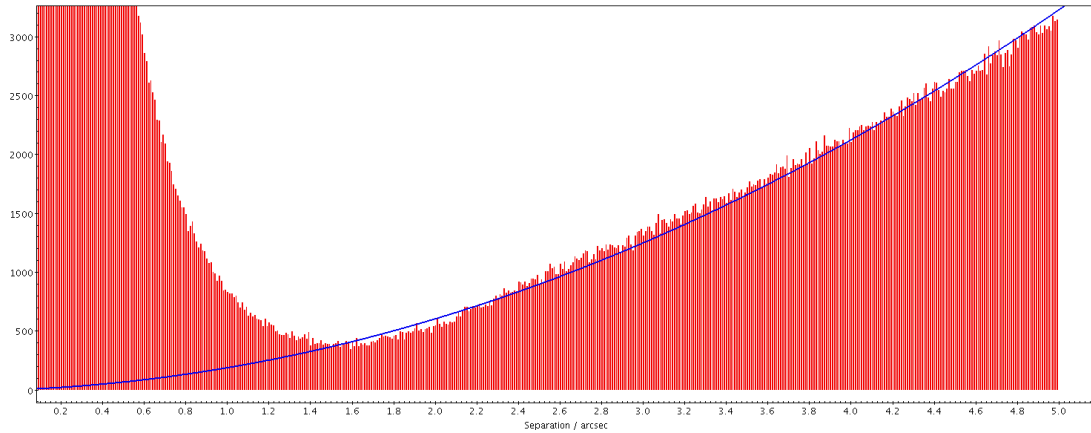


FIGURE 3.1: A histogram of separations when the maximum is set to 5 arcseconds, with all matches shown in the XMM field. The solid blue line is the quadratic model calculated for the number of false matches, given by: $115x^2 + 71x$, where x is the separation in arcseconds.

As shown in Figure 3.2, we also plotted Δ RA against Δ Dec in the first plot and Δ RA against overall RA in the second. The first plot is centred at (0,0), showing that there is no average difference between the VIDEO and SERVS co-ordinates. When looking at the second plot however, the variation in the average offset as a function of Right Ascension reveals residual errors in the Astrometric solutions of either VIDEO or SERVS. The magnitude of this difference is not large enough to affect our results however.

The next step was to use the following equation in conjuncture with the model calculated:

$$P_{match} = 100 \frac{N_{bin} - N_{false}}{N_{bin}} \quad (3.1)$$

where P_{match} is the probability that the source in VIDEO matches the nearby counterpart in SERVS, N_{bin} is the total number of sources from the histogram, and N_{false} is the number of calculated false matches as determined using the quadratic model earlier. Using the information, we decided to apply a limit to the sources in our catalogue, restricting them to have a P_{match} value of greater than 0.9.

Normally when matching with TOPCAT, you would choose the best symmetrical match method, with matches from both catalogues. However, the sources we are trying to find could potentially not be present in the VIDEO catalogue due to extreme reddening. It is therefore better to match the catalogues by choosing all the targets from SERVS, even if this particular source is not in the VIDEO survey.

This method however gives sources that are not covered by the VIDEO field, as shown in the first diagram at the left of Figure 3.3. A simple way around this would be to manually slice around the VIDEO area, but this could potentially not eliminate some sources or cut out successfully matched ones due to inaccuracies. Instead we made use of the confidence map supplied with

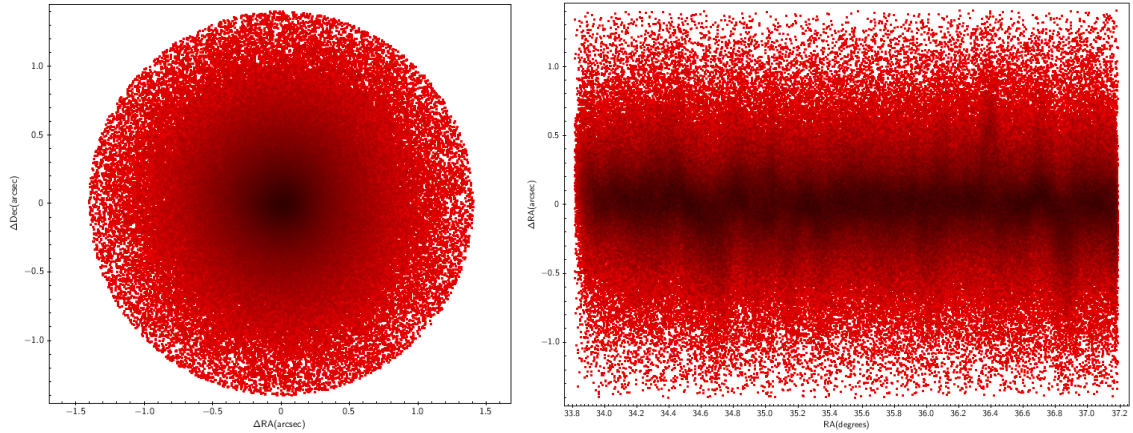


FIGURE 3.2: Two graphs, firstly showing the difference in Right Ascension (RA) and Declination (Dec) for every matched source, and secondly the difference in RA against RA

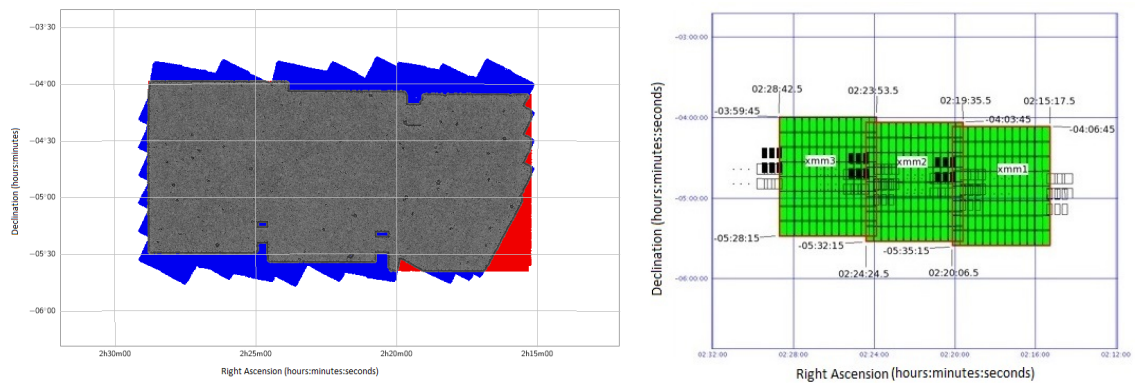


FIGURE 3.3: Two maps of declination against right ascension, the first on the left showing the overlay of surveys in the XMM field. The blue area is only covered by SERVS and the red area only by the VIDEO survey. The grey area in the middle is where the two surveys overlap, where my sample of sources are taken from. The second shows how the three XMM tiles are overlaid over each other, showed with ESO's Survey Area Definition Tool (Jarvis et al., 2013).

the VIDEO catalogue. As shown in the right graph of Figure 3.3, the XMM map is built up from tiles that do not overlap perfectly. The confidence map is a table of values ranging between 0 & 1 for each pixel in the field (with 0 indicating no coverage). These data, as well as most astrometric data, comes in the FITS format, which consists of two parts, the data (which contains all the values of fluxes, flux errors of positions), and the header (which includes how to interpret these data, essentially the column and row information). Using the FITS header, we converted the pixel co-ordinates to RA and Dec values, then selected the nearest pixel to the centre of each source in my catalogue. We then chose sources with a confidence value greater than 0.0 giving me all sources with coverage, and eliminated sources with poor signal to noise ratio (SNR) after (as will be discussing in a following section). As the confidence map came from the VIDEO survey, we just expanded the table with zeros, eliminating any SERVS sources outside the VIDEO survey footprint.

The VIDEO and SERVS catalogues come with many parameters for each source, what they

are and which ones we decided to use will be discussed in the following section. Firstly we will investigate which aperture sizes to use, as the VIDEO survey has 15 aperture possibilities with sizes of 1.0, 1.41, 2.0, 2.83, 3.0, 4.0, 5.0, 5.66, 8.0, 10.0, 12.0, 14.0, 16.0, 20.0 and 24.0 arcseconds while SERVS has 4, with sizes of 1.4, 1.9, 2.9, 4.1, and 5.8. Following Caputi et al. (2012), we decided to match the data from aperture sizes of 2.0 arcseconds in VIDEO and 4.1 arcseconds in SERVS. The reason for the differing aperture sizes between each survey is due to the lower resolution of SERVS compared to the VIDEO survey. We do note that the SERVS aperture fluxes are already aperture corrected, as discussed in Mauduit et al. (2012). Another parameter that each source in the VIDEO catalogue had was the detection flag for each band (H_DET_FLAG is the H band detection for example). This flag was either a 1 or 0 corresponding to a detection or non-detection respectively, however this detection parameter didn't correspond to a greater than 0 flux, or a signal to noise ratio (SNR) of greater than 5, which is often a way to test if a source was detected. This detection flag was rather a leftover from when the VIDEO team ran SExtractor on the catalogue. We therefore determined our own method for determining if a source was detected, as shown in the following Chapter, §3.2.

Something else that needed to be investigated was if there were discrepancies between the fluxes/magnitudes in the VIDEO and SERVS catalogues. The VIDEO survey came with flux values and magnitudes for each source, while SERVS only contained fluxes. However, the VIDEO fluxes were in μJy (which are the correct units that are used in Equation 1.5), whereas SERVS fluxes were in counts s^{-1} . We therefore needed to change these fluxes into μJy before we ran any colour cuts (as described in §3.2)

While matching the surveys, we noticed a problem with the data. The VIDEO catalogue has two versions available, the original, as well as the *error fixed* catalogue. Upon inspection of the flux uncertainty estimates, we found that the original catalogue had errors that were not a linear function of flux, while the “*error fixed*” version had a constant error value for every flux in each photometric band giving a linear function between magnitude and magnitude error. We ascertained, through discussions with the VIDEO survey team, it was simply a missed step when the catalogues were created, we therefore decided that the best step would be to add these two errors in quadrature as follows:

$$\sigma^2 = \sigma_{\text{original}}^2 + \sigma_{\text{error fixed}}^2 \quad (3.2)$$

for every source in the VIDEO catalogue. The original errors, generally called the Read Noise (NR) error, were generated from the object noise of each individual source itself, which is based on the signal of the source and the integration time. The *error fixed* values from the second catalogue are often called the sky or background noise, and measures the noise “under” the object throughout the field of the survey. There are other contributions to the overall noise of

a source, such as the dark current, which is generated from the thermal radiation of the CCD detector itself, however this is including in the errors already presented.

3.2 Detection of ERGs

The next step was applying the colour limit $H - [4.5] > 4$ to all sources in the matched catalogue. It is easier to calculate uncertainties if we use a ratio of fluxes by converting equation 1.5 (For an easier notation, the [4.5] band will henceforth be referred to as B2, with [3.6] referred to as B1): $-2.5 \log_{10} f_H + 8.9 - (-2.5 \log_{10} f_{B2} + 8.9) > 4$ reduces to $\frac{f_{B2}}{f_H} > 39.81$. The general limit used to count a source as detected is called the 5σ limit. We will count a SNR greater than 5 as a sufficient detection in each specific band. Through the propagation of errors, you can check to see if the colour is measured at greater than the 5σ limit:

$$\left(\frac{\sigma_{colour}}{colour}\right)^2 = \left(\frac{\sigma_{B2}}{B2}\right)^2 + \left(\frac{\sigma_H}{H}\right)^2 \quad (3.3)$$

This method gave us some sources in each field, but these were generally the brightest sources with high signal to noise ratio in both bands. It is however important to consider the sources that are very faint in H (potentially due to reddening). Many sources in the catalogue have H band fluxes with a signal to noise detection a lot less than our required value of 5, some even less than 1. When calculating colours for these sources, the low signal to noise ratio means you cannot be sure of the ratio of fluxes ($\frac{f_{B2}}{f_H}$). The way around this is to create 10^5 values for the H and B2 bands separately, with a μ (mean) value of the quoted flux, and a σ (standard deviation) equal to the error. Using Monte Carlo simulations (Kroese et al., 2014), we assumed that the fluxes in each band have Gaussian distributed errors and then applied a prior of $f_H \geq 0$ to the H distribution. By sampling 10^6 values at random from each distribution and calculating a ratio of the two fluxes, we created a similar distribution for colour. We could then calculate a fraction of values where the ratio is greater than 39.81 (the flux ratio corresponding to a magnitude difference of 4). We then used a 90% confidence limit for counting a detected source and at the correct colour. This technique also gives us a method for calculating a colour when there is no value for the flux in the H band (as many sources are only detected in the SERVS catalogue). We can simply create a distribution of H-band flux densities, centred around zero (again eliminating any values ≤ 0). The σ value we used was generated by taking the average value of all sources within 100 arcseconds of the RA and Dec of the source, and then applying the same 90% limit.

3.3 Optical Matching

Once we collated all sources that have an above 90% probability to be a real match between VIDEO and SERVS, as well as an above 90% probability that they have an $H - B2 > 4$ colour, the next step was to match optical data in order to derive the best possible photometric redshifts. The CFHTLS W1 data are not as deep as the D1 counterpart, however the wide data will have more of a chance to contain our sample of sources, and we can extract fluxes if they are too faint to be present in the catalogues. We matched the W1 catalogue with our sample of sources the same way as the earlier matching. As mentioned in §1.3, optical wavelengths are more affected by dust extinction than other parts of the electromagnetic spectrum. It is therefore important to use these extra fluxes in the SED fitting, as they could change the calculated redshifts and extinctions drastically. The SED fitting was carried out both with and without the optical fluxes, and discrepancies in the output results will be discussed in §6.4.

Due to the extremely red nature of the galaxies in our sample (either due to dust extinction or high redshift), the source will be faint at shorter wavelengths. A consequence of this is that some sources may not have detected ($> 5\sigma$) flux values in the optical regime. After matching the optical catalogues to our sample, we found that even though there was optical coverage for the ES1 field, the ERGs from this area had no match in the optical catalogue. To extract extra information we made use of a program called Aperture Photometry Tool (APT, Laher et al., 2012)⁵, that manually measures a flux and error for a generated aperture and input Right Ascension and Declination. We chose the RA and Dec from the VIDEO Survey if the source was detected in VIDEO, or the SERVS RA and Dec if it was not, and found that for a test source that was in the optical catalogue, the output flux was in agreement with other catalogues, however the sky-errors were over-estimated. We therefore used a simple technique to generate an error for a source, again by averaging the catalogue error between sources within 100 arcseconds for the particular waveband. To validate the estimation of flux uncertainties, we also chose consistent sized apertures for each wavelength.

3.4 Herschel Matching

The final step in collating all the data for each source was to match the HerMES, Far-IR data to the sample we had compiled from the NIR and optical data. Rather than download the entire HerMES catalogue, as with VIDEO and SERVS, the HerMES website⁶ has a tool for generating a catalogue of sources around an input Right Ascension and Declination, consisting of positions, fluxes, and errors for sources within a specified radius. After examining the individual images

⁵<http://www.aperturephotometry.org/aptool/>

⁶<http://hedam.lam.fr/HerMES/>

for H1, H2, and H3 (H1 being the best resolution) and calculating separations between VIDEO and HerMES positions, the sources that had a Far-IR match within 0.1 arcminutes (6 arcseconds) were noted. Optical data are important when SED fitting, as it is the most changed by extinction, while Far-IR wavelengths are less affected. This along with the fact that the HerMES bands are at wavelengths a lot longer than the other surveys, and the data has a worse resolution, led us to the decision that this extra data would not be used in the Le Phare photometric redshift estimation. This was more accurately due to the fact that most templates in Le Phare don't have far-IR sections, but also because studies have shown that Far-IR data are not particularly useful when deriving photometric redshifts, e.g. Pearson et al. (2013). This is because far-IR data produces only very coarse photometric redshift constraints.

Chapter 4

Estimating Redshifts and other Characteristics

4.1 Le Phare

As mentioned in §1.2, Le Phare (Arnouts et al., 1999) is a piece of software that fits hundreds of potential SEDs to the photometric fluxes in our sample of sources, estimating extinctions and redshifts. It requires many different settings that need to be investigated before using it to calculate redshifts. The following section will show how these factors were decided upon.

4.1.1 Templates

The first step was to choose which templates to use to fit the photometry we have assembled. Le Phare has a total of 18 potential SED packages that model galaxies as well as 4 for quasi-stellar objects (QSOs). We chose to use 3 different packages that model galaxies (AVEROIN, BC03 and CWW_KINNEY), all QSO templates that come with Le Phare, as well as a selection of SEDs that contain Galaxy and QSO templates called the POLLETTA package. These packages will be outlined in the following section.

AVEROIN is the biggest galaxy package containing 62 templates, including starburst, spiral, elliptical, and irregular galaxies taken from Coleman et al. (1980), Kinney et al. (1996), and Bruzual and Charlot (2003). This package is used by the VIDEO team as it contains a wide selection of galaxies. These templates have also been tuned with mid infrared, 3.6-4.5 μm photometry, which is helpful as these bands are used in this work. The VIDEO team also carried out their own photometric redshift fitting, validating these templates' use.

The BC03 package has 13 templates based on Bruzual and Charlot (2003) stellar population models, generated by Kauffmann et al. (2003) and Tremonti et al. (2004). These models have varying ages, two 12 Gyr templates that have exponentially declining star formation histories, and a 6 Gyr template with a constant star formation history. The last 10 templates are instantaneous burst models with differing ages of: 5, 25, 100, 290, 640, 900 Myrs, and 1.4, 2.5, 5, 11 Gyrs. Each of these 13 templates are generated with different metallicity (Z) values of 0.008, 0.02 and 0.05, giving a total of 39 templates. These templates are important as they cover all the three main commonly used star formation histories, as well as a large range of ages.

The CWW_KINNEY package contains a small selection of templates. The first 4 are also from Coleman et al. (1980), extrapolated to ultraviolet and infrared frequencies with the GISSEL code (Arnouts et al., 1999), modelling elliptical and irregular galaxies, as well as two spirals classified as Sbc and Scd. The next 6 templates were generated by Kinney et al. (1996) as well as with the AVEROIN package, using Calzetti et al. (2000), and all model starburst galaxies.

Le Phare comes with many different QSO templates, in a total of 4 packages. The first is called the MARA package (Salvato et al., 2009) and consists of 18 hybrid models based on non-active galaxies and QSOs. The next is a selection of 31 synthetic QSOs that were generated based on code by Hook et al. (1998), called the SYNTH package. The VARIOUS package is the last one containing solely QSOs, a small selection of 13 templates, consisting of composite and QSO models (Netzer et al., 2007; Cristiani et al., 2004; Rowan-Robinson et al., 2008).

As mentioned earlier, the final package, POLLETTA (Polletta et al., 2007), contains both galaxy and QSO templates. It contains 16 galaxy models, (3 ellipticals, 7 spirals and 6 starbursts), 7 QSO models (3 type 1s and 4 type 2s) as well as 2 composite templates that model starburst QSOs. This group of templates contains standard models of certain galactic types, as well as specific, well known galaxies and QSOs.

The packages that we have selected to use with Le Phare were chosen to cover as wide a range of galaxy types and QSOs as possible, because of the extreme colours of sources in our sample. Many different ages, star-formation histories, and metallicities are covered, as well as many of the different spiral and elliptical types, including irregular galaxy models. Different types of QSOs are covered, and hybrid models covering starburst QSOs as well as models generated from specific galaxies and QSOs in the literature.

4.1.2 Extinction

After choosing all our templates, there are still a few parameters that needed to be decided upon before we could run Le Phare on our sample of sources. As mentioned in §1.3 the extinction values (as given by Equation 1.6) that are applied to each of our sample of templates need to be

chosen (with our sample of templates being the Allen MW law, the Fitzpatrick LMC law, the Prevot SMC law, and the Calzetti law, as discussed in §1.3). As mentioned earlier Caputi et al. (2012) also studied $H - B2 > 4$ galaxies, choosing to test extinction values of $0.0 \leq A_V \leq 8.0$ in steps of 0.1. Wang et al. (2015), studied galaxies with the same colour cut but a different limit ($H - B2 > 2.5$), using extinction values of $0.0 \leq A_V \leq 6.0$. For our study we chose to use E_{B-V} values between 0.0 and 2.3 at increments of 0.1, corresponding to a range of $0.0 \leq A_V \lesssim 9.0$, depending on the law used.

4.1.3 Extra Parameters

Another parameter that needs to be set is by how much the flux errors that come in the source catalogues need to be increased before running Le Phare. The reason this step is carried out is to account for uncertainties in the flux calibration of the photometry and the models, due to the extremely precise nature of the templates *i.e.* the templates don't have uncertainties or scatter. Previous work has shown that even with a broad set of templates, you need to add this extra error in quadrature to generate sensible model fits (Chen et al., 2014; Acquaviva et al., 2015). The default value that Le Phare uses for this parameter is 5%, however we chose to change this value to 10% due to the high chi-squared values generated from preliminary results with Le Phare. This was thought to be most likely due to the irregularity of the SEDs of the extremely red galaxies in our sample, but also to account for different seeings, apertures, and calibration uncertainties in the different survey data that we are using.

A final change that we adjusted in the settings of Le Phare is whether or not Le Phare included emission lines when fitting (Le Phare cannot include absorption lines). As mentioned in §1.2, SEDs contain many lines, some very pronounced and some insignificant, that are used to calculate redshifts for extremely close galaxies. Due to the fact that we only have broad band photometric fluxes for my sources, and that all my band filter curves are considerably wider than emission lines, it would seem that it would not be necessary to use them in the fitting. However large emission lines such as the $H\alpha$, could increase or decrease the flux in a specific band respectively if it happened to perfectly line up (potentially because these will be the brightest ultra red galaxies found). We therefore provisionally decided to include emission lines when using Le Phare, and tested for any discrepancies between the inclusion and exclusion of these lines; finding no differences.

An example *zphota.para* file is shown in Appendix A, containing all the parameters that can be adjusted or removed all together when running Le Phare.

4.2 Running Le Phare

Now that we had collated all templates, extinction laws, A_V values and investigated other settings for Le Phare, we began to run the sample of sources through the code to generate redshifts. To start with we needed to generate theoretical magnitude libraries that are based on the filter curves for the wave-bands we are using. Le Phare works by iterating between all chosen SED templates, extinction curves, extinction values (E_{B-V}), and potential redshift values (which we chose to be in the range $0.0 \leq z \leq 8.0$ with steps of 0.1), trying to find a minimum chi-squared. Herein lay a problem however; due to the total choice of 127 galaxy templates, 51 QSO templates, and 20 composite templates, as well as 4 differing extinction laws (each with 24 A_V values) and 151 potential redshift intervals, Le Phare needed to iterate through a large number of potential best fit combinations. Due to how Le Phare is coded, if we tried to generate a magnitude library larger than approximately 1 million variations, it would break down. We therefore decided to create the libraries separately for each package of SEDs, sometimes even splitting them up further by extinction law if the specific package was too large. By default, Le Phare also runs all input QSO templates without altering the extinction law or A_V values, due to it assuming if the galaxy that is being investigated is a QSO, it is unattenuated by dust. To work around this problem, we ran all QSO templates through Le Phare as galaxies, thereby including all extinction laws and extinction values.

4.3 Output

The standard output of Le Phare is one line of values, including; best fit redshift with chi-squared values, as well as the corresponding SED model and A_V value. Due to the necessary splitting of the magnitude libraries, we needed to devise a way to merge all the outputs for each source, rather than just choosing the lowest chi-squared. The `CHL.OUT` setting, if changed to true, causes Le Phare to output all chi-squared values for each iteration of model, extinction value and redshift. After running Le Phare for my sample of sources, we grouped all the chi-squared values by redshift, and by calculating a probability with the following equation:

$$P \propto e^{-\frac{\chi^2}{2}} \quad (4.1)$$

we were able to generate a probability density function (PDF) for the whole redshift range across all models, extinction laws and A_V values. To determine if the sources in my sample were QSOs or galaxies, we also generate PDFs for their respective templates individually. For most of the sources this was a good way to identify them. However some sources could be ambiguous, so we overlaid both the QSO and Galaxy PDFs on top of the total one to see if particular peaks

came from QSOs or Galaxies, or if the total was an equal combination of both. Another test that was carried out was to generate a separate PDF for when Le Phare was ran with and without the optical data. This was a way to see if matching my sample to an optical catalogue was necessary, and if it changed the redshift output at all.

The redshift of each source will be portrayed in two ways. Firstly the redshift output from the individual, or potentially multiple, best fits from Le Phare, and secondly a percentile method that generates an error. We first converted each PDF for redshift into a Cumulative Distribution Function (CDF), and reading off the probability axis (which runs from 0 to 1) at 0.16, 0.50, and 0.84. This generates a redshift with an upper and lower limit, that can be converted into a positive and negative error. This method of determining a redshift attempts to capture some of the possible asymmetry in the PDF, however the value can sometimes differ vastly from the primary peak, as some sources contain multiple peaks in the redshift PDF. The redshifts generated from both methods are therefore presented.

4.4 Star Formation Rates

Chapter 2.3 explored what wavelengths are best for calculating a Star Formation Rate (SFR) of sources, whether it is a range or a single band. When choosing which HerMES band to use, out of 250, 350 and 500 μm , there were two factors that were considered. Firstly by looking at individual images of each band, we found that the lowest wavelength, 250 μm , was the best quality image. As determined earlier in section §2.3, this is due to the resolution, shown by the equation $\theta = \frac{1.22\lambda}{D}$, with θ as the resolution, λ the wavelength, and D the telescope diameter. As shown the lower the wavelength, the better the resolving power of the band for a specific telescope. As discussed earlier the 250 μm band corresponds to a star-formation luminosity peak at 60 μm , redshifted to ~ 3 . This band is best suited to calculate a SFR, as the other bands contain the luminosity peak at a much higher redshift. It was also found that this waveband contained the most complete flux data for our sample of sources.

To calculate the Star Formation Rate for our sources we used a program (provided by D.Smith through private communication) that converts a specified flux density (in Jy), measured at a far-infrared wavelength, to a total FIR luminosity between 8 and 1000 μm and SFR (in $M_{\odot}\text{yr}^{-1}$), based on the input redshift. We assume a Kennicutt (1998) Law for a star formation to far-infrared luminosity relation, and adjust for a Chabrier (Chabrier, 2003) Initial Mass Function (IMF). Instead of using a grey body model with a specified temperature and emissivity, we made use of the M82 SED model (Polletta et al., 2007). The downside to this model is that a single FIR flux density and redshift only outputs a single SFR. To work around this problem we first generated 100,000 randomised flux values based on the flux and error from the 250 μm , H1, HerMES band, similar to earlier when calculating colour. We then read 100,000 random values

from the redshift PDFs and ran the SFR code 100,000 times, generating a similar probability density function for SFR, including both the redshift and $250\mu m$ uncertainties. We then read off a single SFR with errors, in a similar fashion to the calculated redshift.

Chapter 5

Results

This Chapter will contain individual results for each source in our sample; including *Postage-Stamp* images for each source in every available band, best fit SEDs overlaid on photometric fluxes, as well as probability density functions (PDFs) for redshift and 2-dimensional ones for $z - A_V$. We also reproduced Figure 1.4 from Caputi et al. (2012), overlaying our sample of sources, as well as a graph with the same axes, showing all sources in the XMM field to show the irregularity of our sources. The *Postage-Stamp* images are adjusted using the FITS viewing software called ds9⁷, and are shown with a 2 arcsecond green circle centred at the Right Ascension and Declination taken from the corresponding catalogue. They are also orientated so that north is up and east is to the left. The best fit SEDs are shown using software that uses an output file generated by Le Phare, called PARSing and Plotting Spectra (PAPS⁸). This software plots the SED, including the fluxes, as well as a legend dictating the characteristics of the best fit and a sample redshift PDF. The legend contains the specific fit's model used (mdl), chi-squared value (χ^2), redshift (z), Extinction Law (ELaw), Extinction Value, E(B-V), Infrared Luminosity (Lir), and a few other values that could not be calculated here such as Age, SFR and Mass. The PDF generated by this program only includes information from the one set of fits, so isn't a good estimation of the density of probabilities. Instead we made use of the other output of Le Phare, the *chi* file, as mentioned earlier with the CHLOUT setting. There are two redshift PDFs following for each source, one including the optical data, and one without. Each PDF is also split into a sub function for redshift based on solely the Galaxy templates, solely the QSO templates, and all of them at once. This is because whether or not the best fit SED is a QSO or Galaxy template may not be the best way to determine if the source is most likely one or the other. A final way to picture the data output from Le Phare is the same way Caputi et al. (2012) did in their study, as shown in Figure 1.7. As mentioned this is a PDF the same as we have already generated for redshift, but is instead shown on a 2D plane of extinction (A_V) against redshift (z).

⁷<http://ds9.si.edu/site/Home.html>

⁸<https://kenai.com/projects/paps>

Source	IDs			RA	Dec	$H - B2$
	CFHTLS	VIDEO	SERVS	(Degrees)	(Degrees)	Colour
XMM 1	1021135	1020268	44273	36.0412	-5.5211	4.83±0.15
XMM 2	1255483	1246051	388221	34.2132	-4.9774	4.34±0.05
XMM 3	1279111	1268713	176707	36.8094	-4.9286	4.19±0.01
XMM 4	1347192	1334334	442973	34.4794	-4.7899	4.24±0.12
XMM 5	1586372	1564484	595331	35.0370	-4.3053	4.30±0.03
XMM 6	1676938	1651840	603486	35.9080	-4.0869	4.20±0.11
ES1 1	-	1140842	128833	10.0845	-44.4562	4.68±0.65
ES1 2	-	1142103	137276	10.0367	-44.4508	4.28±0.15
CDFS 1	-	1108936	454777	52.2380	-28.6866	4.60±0.18
Optical Fluxes (μJy)						
	u	g	r	i	z	
XMM 1	0.021±0.045	0.106±0.037	0.053±0.069	-	0.138±0.251	
XMM 2	0.011±0.048	0.012±0.037	0.126±0.063	0.648±0.081	0.443±0.257	
XMM 3	0.362±0.045	0.511±0.037	0.834±0.065	-	3.081±0.254	
XMM 4	0.043±0.045	0.004±0.036	0.006±0.067	0.098±0.079	0.154±0.255	
XMM 5	0.263±0.048	0.369±0.039	0.476±0.066	0.779±0.081	1.076±0.254	
XMM 6	0.002±0.047	0.135±0.038	0.200±0.066	0.440±0.081	0.403±0.254	
	b	v	r			
ES1 1	-0.018±0.009	0.043±0.013	0.006±0.018			
ES1 2	-0.011±0.009	0.009±0.013	0.006±0.018			
VIDEO Fluxes (μJy)						
	Z	Y	J	H	K	
XMM 1	-	0.393±0.086	0.529±0.126	1.456±0.207	3.518±0.277	
XMM 2	1.056±0.012	1.634±0.081	-	4.716±0.202	8.635±0.258	
XMM 3	2.901±0.013	5.501±0.081	9.189±0.119	16.080±0.196	31.220±0.257	
XMM 4	0.110±0.012	0.236±0.080	-	1.772±0.203	4.259±0.259	
XMM 5	1.054±0.021	1.649±0.081	3.732±0.123	6.939±0.198	11.278±0.260	
XMM 6	-	0.554±0.082	0.850±0.121	2.061±0.200	5.597±0.263	
ES1 1	-0.075±0.059	-0.135±0.091	0.212±0.231	0.299±0.188	1.316±0.250	
ES1 2	0.037±0.059	0.105±0.091	0.465±0.231	1.301±0.188	2.938±0.250	
CDFS 1	-	-	0.755±0.059	0.826±0.382	2.262±0.397	
SERVS Fluxes (μJy)		HerMES Fluxes (mJy)			Separation	
	B1	B2	H1	H2	H3	(arcseconds)
XMM 1	61.728±0.935	124.480±0.987	40.32±5.66	31.87±4.70	3.78±9.45	0.36
XMM 2	108.643±0.839	258.304±0.854	10.97±5.69	11.87±4.46	1.02±4.61	0.27
XMM 3	315.239±0.929	759.134±1.264	0.74±5.67	-	-	0.19
XMM 4	61.053±0.532	88.193±0.648	42.67±5.65	41.70±4.58	29.23±4.87	0.81
XMM 5	119.264±0.828	363.530±0.925	9.37±5.66	0.47±4.46	-	0.10
XMM 6	52.842±0.652	98.426±0.996	34.85±5.67	30.60±4.94	24.52±5.82	0.52
ES1 1	14.983±0.832	22.381±0.632	-	-	-	-
ES1 2	30.065±0.762	67.465±0.933	50.10±4.86	1.98±8.67	-	0.04
CDFS 1	15.198±0.746	57.151±0.767	19.87±3.82	3.49±5.27	-	0.03

TABLE 5.1: Complete list of the data for all 9 Extremely Red Galaxies in our sample. Shown in the first section is the CFHTLS (where appropriate), VIDEO and SERVS IDs, the Right Ascension (RA) and Declination (Dec), as well as the H-B2 colours with. This second part shows the optical fluxes of each source in μ Jy whether from CFHTLS or ESIS with dashes corresponding to a band without any coverage for a particular source. Following this is the VIDEO flux section, all values again in μ Jy. The final section shown the SERVS and HerMES fluxes for all sources, in μ Jy for SERVS and mJy for HerMES. Note that a dash for the HerMES fluxes does not correspond to no coverage for that source, rather no flux value being present in the catalogue. The final column is the separation between the VIDEO RA and Dec and the best match in the HerMES catalogue in arcseconds.

Source	Probability		Best Fit				Percentile		SFR
	Colour	Separation	A_V	Redshift	Model	Law	A_V	Redshift	$M_{\odot}\text{yr}^{-1}$
XMM 1	1.00	1.00	5.89	0.63	(a)	LMC/MW	$5.72^{+0.43}_{-0.68}$	$0.60^{+0.20}_{-0.11}$	$128.4^{+85.2}_{-41.9}$
XMM 2	1.00	1.00	3.72	0.51	(a)	LMC/MW	$3.71^{+0.15}_{-0.04}$	$0.46^{+0.04}_{-0.04}$	$22.0^{+14.9}_{-13.3}$
XMM 3	1.00	1.00	0.27	1.12	(b)	SMC	$0.24^{+0.17}_{-0.24}$	$1.08^{+0.67}_{-0.07}$	$-3.9^{+48.9}_{-49.0}$
XMM 4	0.98	1.00	1.09	1.35	(b)	SMC	$0.95^{+0.14}_{-0.13}$	$1.32^{+0.17}_{-0.11}$	$451.9^{+103.9}_{-84.8}$
XMM 5	1.00	1.00	0.27	1.85	(b)	SMC	$0.07^{+0.05}_{-0.05}$	$1.57^{+0.09}_{-0.06}$	$136.2^{+99.1}_{-92.4}$
XMM 6	0.98	1.00	2.72	0.30	(a)	SMC	$0.99^{+1.00}_{-0.58}$	$1.77^{+4.61}_{-1.61}$	$340.4^{+234.4}_{-337.9}$
			0.27	1.75	(b)	SMC			
ES1 1	0.91	0.99	7.90	1.42	-	-	$3.10^{+1.82}_{-1.88}$	$2.76^{+4.04}_{-1.23}$	-
			5.06	2.50	-	-			
			2.63	4.60	-	-			
ES1 2	0.98	0.99	4.81	1.98	(c)	SMC	$4.19^{+0.16}_{-0.29}$	$2.06^{+0.07}_{-0.05}$	$1032.1^{+143.6}_{-135.6}$
			5.11	2.13	(d)	SMC			
CDF5 1	0.94	0.99	4.90	1.24	(a)	LMC/MW	$5.29^{+0.59}_{-0.71}$	$2.84^{+1.03}_{-0.48}$	$681.7^{+335.2}_{-251.1}$
			1.62	2.43	(b)	SMC			
			5.43	2.97	(e)	SMC			
Model	(a)	Type 2 QSO from the VARIOUS Package, that models IRAS 09104+4109							
	(b)	Type 2 Torus QSO model from the POLLETTA Package, modelling SWIRE J104409.95+585224.8							
	(c)	Hybrid QSO-Galaxy Model from the MARA package							
	(d)	Instantaneous Starburst Galaxy Model from the BC03 Package (Age of 640 Myrs, Metallicity of 0.05)							
	(e)	Template from the POLLETTA package that models a Sc galaxy							

TABLE 5.2: Results for all sources in our sample, firstly including the probability of colour and separation. Each potential best fit that generated a corresponding peak (or sub-peak) in the source's PDF is shown, with the E_{B-V} , converted A_V , redshift and model used. The percentile redshift and star formation rate is also given, as calculated through the method discussed in Chapters 4.3 and 4.4 respectively. Finally the models corresponding to the letters given for each source are shown at the bottom.

The probabilities are shown from the colour-bar to the right of the diagrams. We will also use the B2 magnitude as an indicator for the brightness of the source. Next, the SFR is shown as generated using the method described in Chapter 4.4, using the redshift PDF for all models. The information for all the sources in our sample are collated in Table 5.1, while the probabilities, best-fit solutions, percentile A_V and redshifts values, as well as the SFRs are shown in Table 5.2.

5.1 Notes on Individual Objects

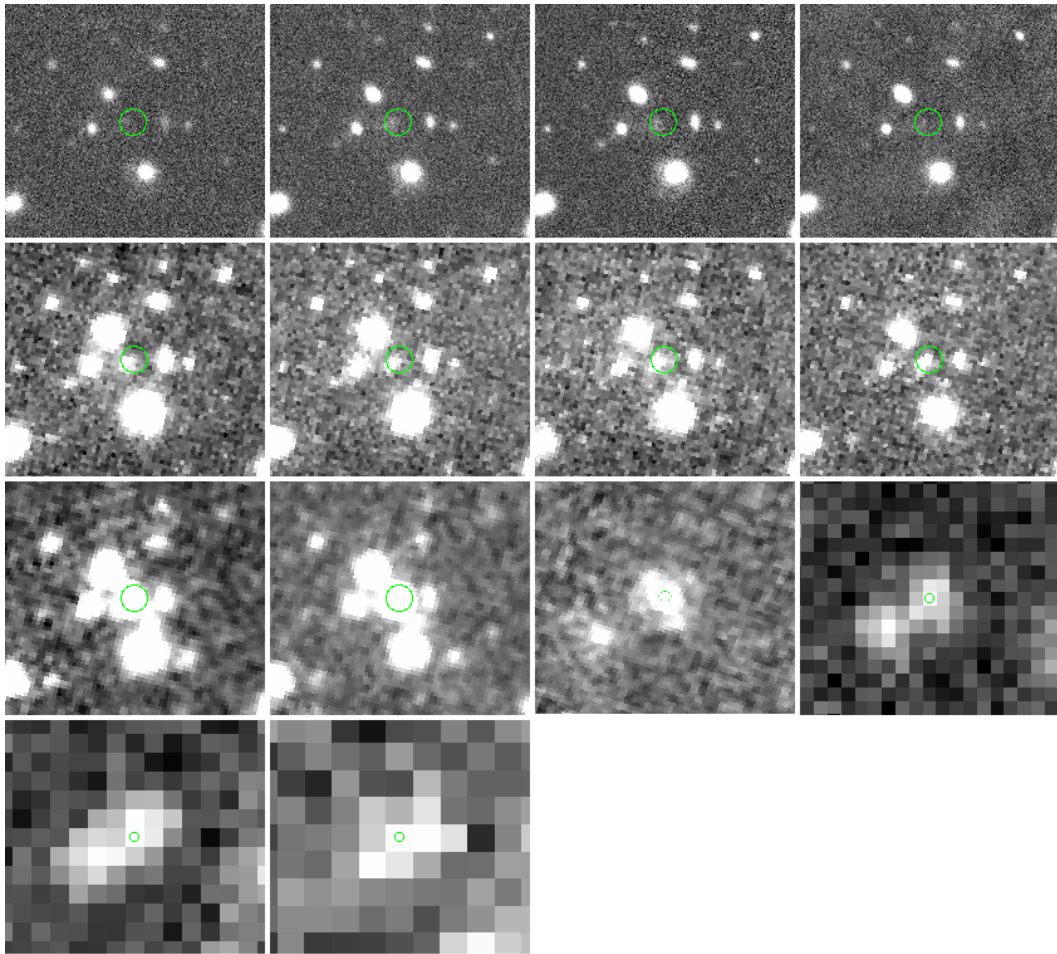
5.1.1 XMM 1

The XMM and ES1 fields covered by VIDEO and SERVS both overlap by approximately 4.5 deg^2 , and the XMM field goes to a slightly greater depth; it was therefore expected to generate the largest sample of ERGs. The first source, named XMM 1, is the reddest galaxy in our selection (with a H-B2 colour of 4.83 ± 0.15), and is also one of the faintest with a B2 magnitude of 18.66 ± 0.01 . This source is covered by CFHTLS (as with all sources in the XMM field), except i band, as well as having flux values in all three HerMES bands, however there is no Z coverage for the XMM3 tile (see the right panel in Figure 3.3). Through manual inspection of the Postage Stamp images in Figure 5.1(a), we see a clear source that is very faint but visible in the optical, and increasingly bright up to the SERVS bands. As seen there is some slight overlap between neighbouring sources in B1 and B2, however the aperture size chosen enables only the intensity of the ERG to be measured. For the HerMES bands, H1, H2, and H3, we can see due to the lower resolution of Herschel, the matched Far-IR counterpart of XMM 1 is generated from the nearby sources, even though the RA and Dec taken from VIDEO does match up with a source in H1. As discussed in §3.4, we matched our sample to the HerMES data within 6 arcseconds, but the best match is a source at 0.36 arcsecond separation.

The best fit SED shown in Figure 5.1(b) gave a redshift of 0.63 with an E_{B-V} value of 1.90 using either the LMC or MW extinction law, as both generated the same χ^2 value of 17.3. The model used for this fit is from the VARIOUS package; a Type 2 QSO that models IRAS 09104+4109, taken from Vignali et al. (2011). Looking at Figure 5.1(b) differences between this model and the photometric fluxes, in particular at wavelengths below $0.7 \mu\text{m}$, are apparent, potentially due to the lower SNR of the optical fluxes. However we do note that this template is the most featureless out of the best fits for our whole sample, and is also highly irregular at $\lambda < 1.0 \mu\text{m}$, especially the straight, peaked section of the model at $0.0 \mu\text{m} < \lambda < 0.5 \mu\text{m}$. Differences between the model and photometric fluxes at these wavelengths will be discussed in §6.4.

As shown by the two different redshift PDFs, Figures 5.2(a) and 5.2(b) with and without fitting the optical data respectively, there is no discernible difference between the outputs. The PDF also shows a very strong primary peak, with a smaller bump at a greater redshift. The method described in Chapter 4.3, used to calculate the percentiles, gave a value of $0.60_{-0.11}^{+0.02}$ for redshift and an A_V value of $5.72_{-0.68}^{+0.43}$ for XMM 1. It is also noted that the contribution to the PDF from galaxy templates only leads to a strongly disfavoured solution at $z \sim 1.7$, shown as a the red dotted line. The $z - A_V$ PDFs both using and not using the optical data are shown in Figure 5.2(c) and 5.2(d) respectively. We note that these PDFs line up with the redshifts output in Figures 5.2(a) and 5.2(b), however the extinction is less well constrained, as the values span a

range of $\Delta A_V \sim 2.0$. These PDFs as expected do not change significantly with the inclusion of the optical data, however there are slight alterations. The SFR for this source was calculated at $132.4^{+78.0}_{-36.8}$.



(a) Postage Stamp Images

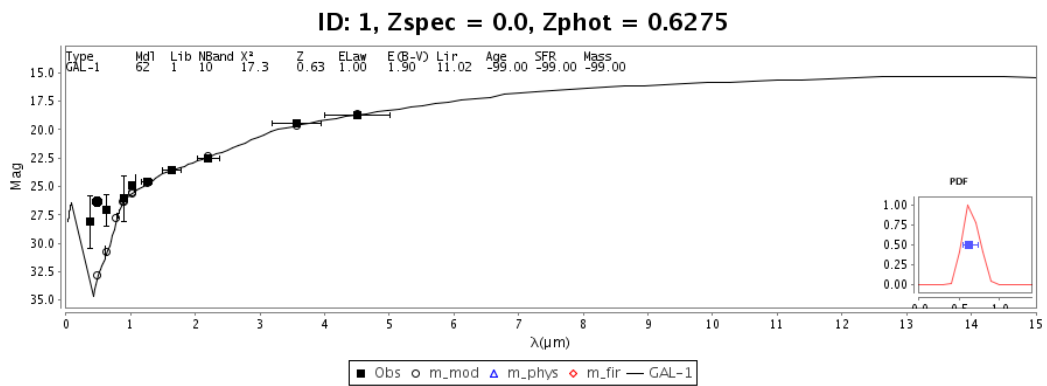


FIGURE 5.1: Two figures for XMM 1, firstly (a) shows postage stamp images reading from the top left in u, g, r, z, Y, J, H, K, B1, B2, $24\mu m$, H1, H2 and H3, the green circle in each image has a radius of 2 arcseconds. (b) shows the best fit SED.

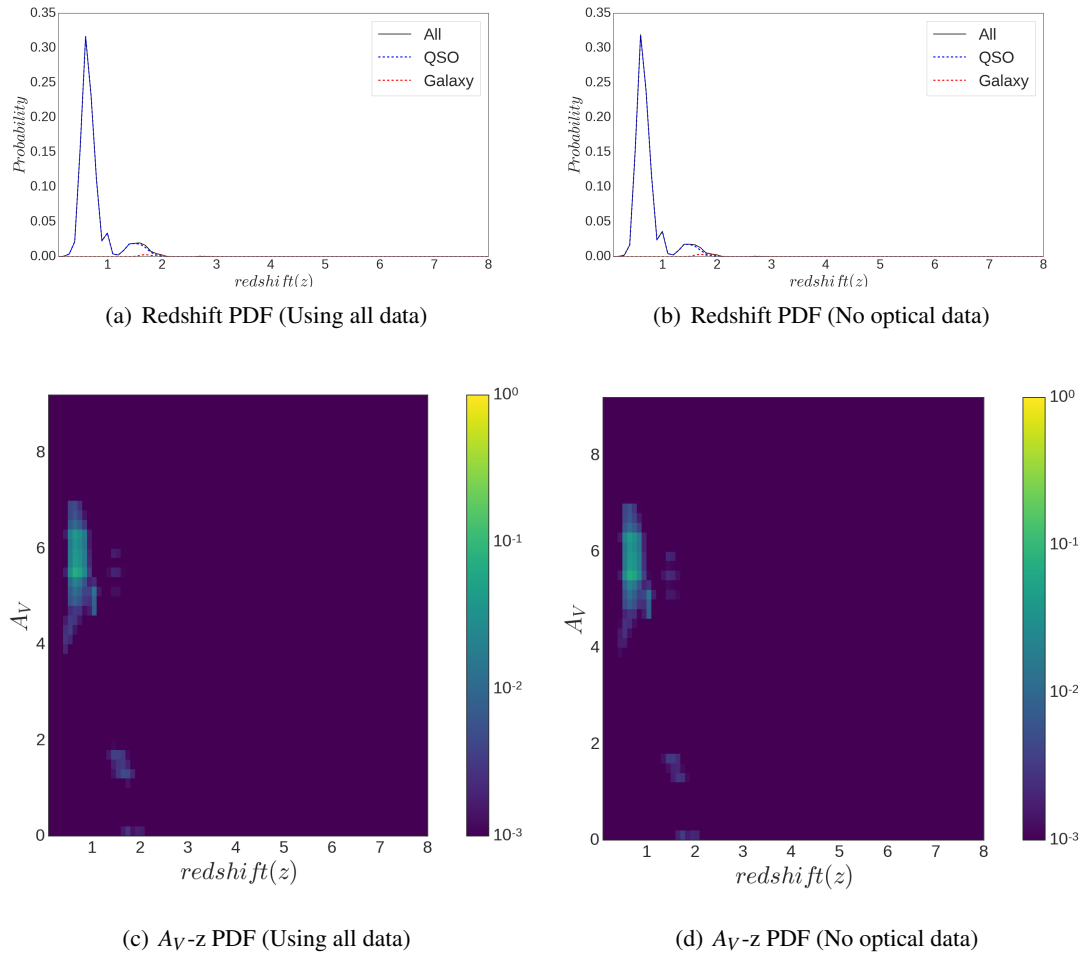


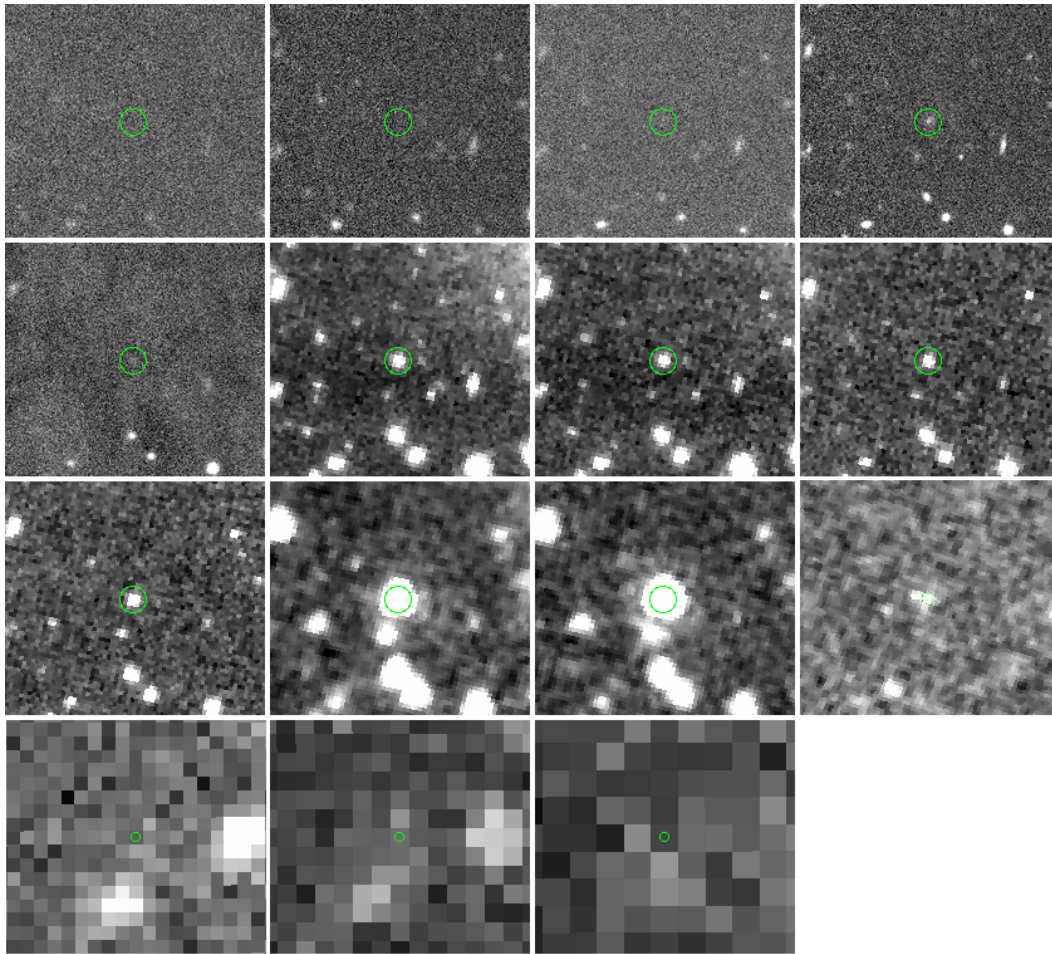
FIGURE 5.2: Four figures for XMM 1; (a) is the redshift PDFs using the optical data and (b) not using the optical data. The black solid line, the blue dashed line and the red dashed line are the probability contributions from all the templates, only the QSO templates, and only the Galaxy templates respectively. (c) and (d) are the redshift(z)- A_V 2-variable PDFs upon using and not using the extra data. The colour-bar indicates the probability in each cell.

5.1.2 XMM 2

The next ERG, XMM 2, is one of average brightness in our sample with a B2 magnitude of 17.870 ± 0.004 , and has an average H-B2 colour of 4.34 ± 0.05 . It has full optical coverage and all three Far-IR fluxes, however as with there being no Z coverage for the XMM1 tile, there is no J coverage for the XMM3 tile, leading to no J flux for this source (see Figure 3.3). Looking at Figure 5.3(a), we see that this source is well isolated from nearby sources, and is well matched between CFHTLS, VIDEO and SERVS. Even though there is a matched source at a separation of 0.27 arcseconds, upon inspection of the HerMES images it seems that there is no source present. We will however still carry out the Star Formation calculations.

The best fit for this source gives a similar redshift of 0.51 and E_{B-V} of 1.20, again using LMC or MW extinction law. Again this fit makes use of the Type 2 QSO model taken from Vignali et al. (2011) and actually fits the optical data better, however this is more likely due to the even lower SNR of the fluxes.

Looking at the redshift PDFs as before, Figures 5.4(a) and 5.4(b) show a slight difference, however they both consist of a strong, solitary peak that gives a redshift of $0.46^{+0.04}_{-0.04}$ with the optical data, which agrees with the best fit redshift value of 0.51. For this source there is a negligible contribution to the PDFs from the Galaxy templates, leading to the conclusion that this source is a QSO. The $z - A_V$ PDFs shown in Figures 5.4(c) and 5.4(d) are some of the most featureless, as there is a single probable area with a value of $3.71^{+0.15}_{-0.04}$, and very little difference between the two. The SFR for this source was relatively low, at $25.1^{+7.6}_{-6.6}$.



(a) Postage Stamp Images

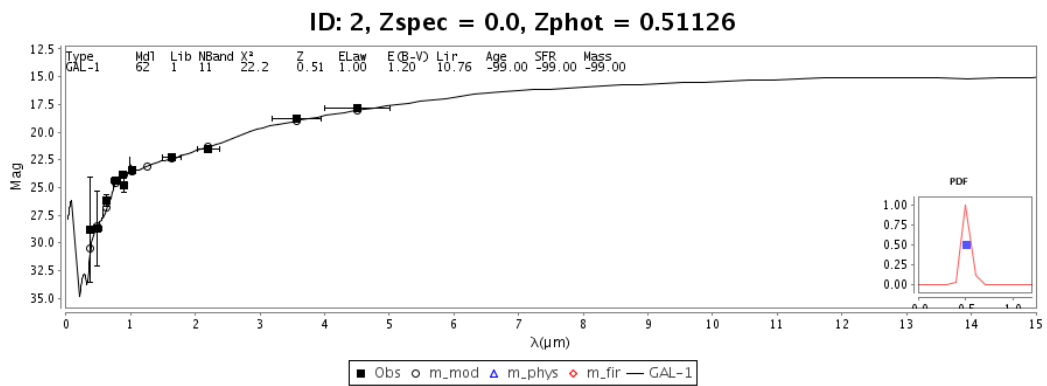


FIGURE 5.3: Two figures for XMM 2, firstly (a) shows postage stamp images reading from the top left in u, g, r, i, z, Z, Y, H, K, B1, B2, 24 μ m, H1, H2 and H3, the green circle in each image has a radius of 2 arcseconds. (b) shows the best fit SED.

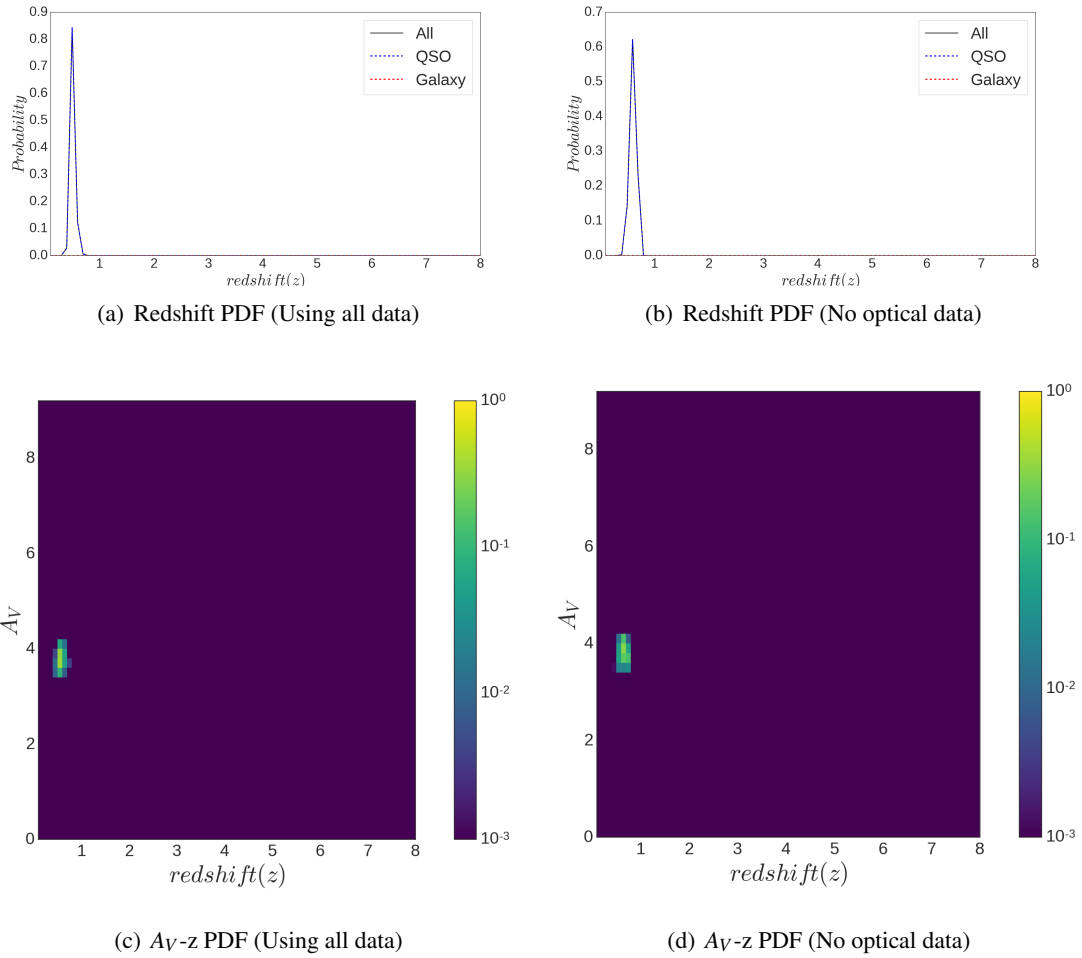


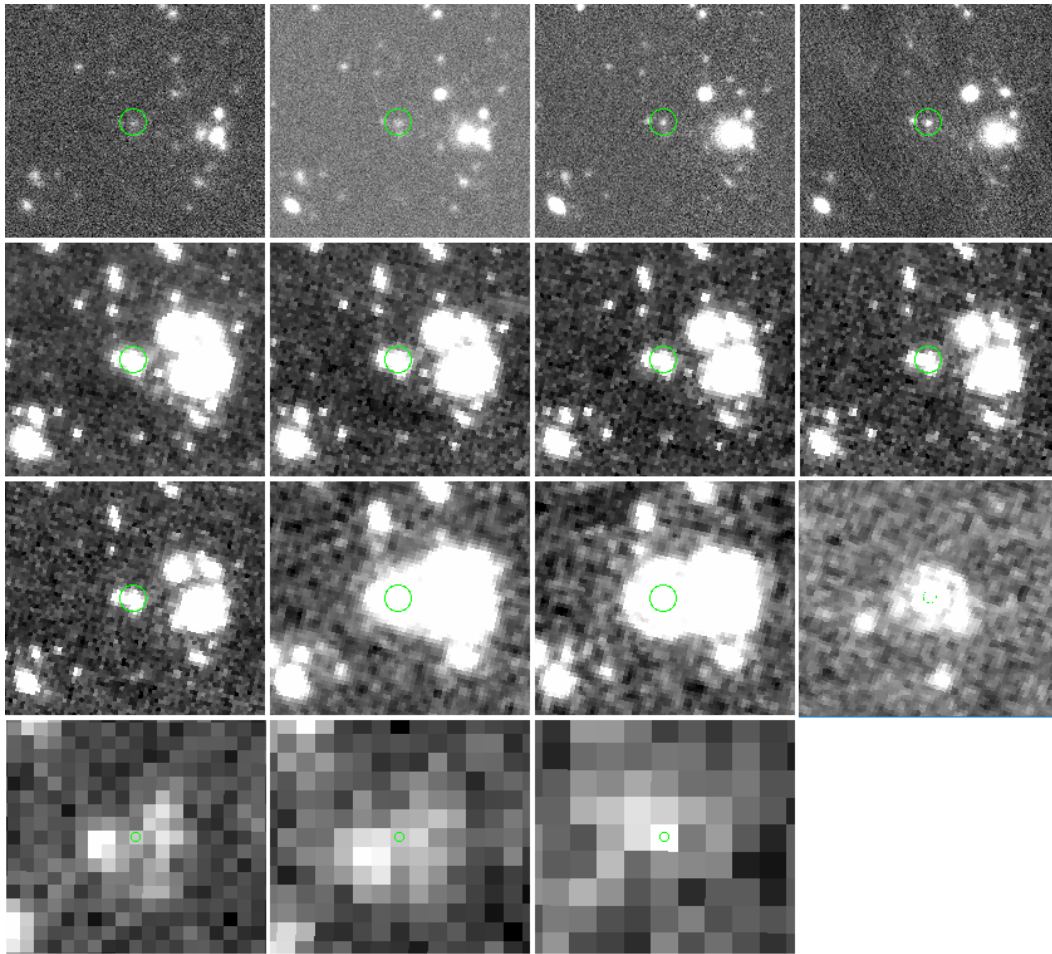
FIGURE 5.4: Four figures for XMM 2; (a) is the redshift PDFs using the optical data and (b) not using the optical data. The black solid line, the blue dashed line and the red dashed line are the probability contributions from all the templates, only the QSO templates, and only the Galaxy templates respectively. (c) and (d) are the redshift(z)- A_V 2-variable PDFs upon using and not using the extra data. The colour-bar indicates the probability in each cell.

5.1.3 XMM 3

The third source in our sample is the brightest but bluest ERG, with a B2 magnitude and H-B2 colour of 16.690 ± 0.004 and 4.19 ± 0.01 respectively. It is covered by all optical bands except the i band, and the first source with all VIDEO fluxes. It has a H1 flux with an extremely low SNR and no H2 or H3 fluxes in the catalogue. Upon examination of Figure 5.5(a) we see many things. Firstly this source is the brightest in all bands, especially in the optical, leading to a very clear source in u, g, r, and z. Next the VIDEO images start to show neighbouring galaxies blending together, notably the source in our sample with the fainter source to the left. This is not a problem with the VIDEO data, however the considerable worsening of this blending, as well as the increased size of the aperture for SERVS, leads us to query how accurate the given fluxes are. Finally the H1 and H2 HerMES images are centred between two increased areas of intensity, however as we matched a source at a separation of 0.19, we will continue with the Star Formation estimation.

As shown earlier, the first two sources best fit to QSOs with redshifts around 0.5, relatively high extinctions, and used the same model. This source however differs, as it has a slightly higher redshift of 1.12 and E_{B-V} value of 0.1 using the SMC law. The model used is the Torus template from the POLLETTA package, used to fit Type 2 QSO, and seems to match the optical data a lot better. This corresponds to the model used to fit SWIRE J104409.95+585224.8 in Polletta et al. (2006). We note that this template contains a lot more features than the Type 2 one used for XMM 1 and 2. In comparison to the best fit shown in Figure 5.1(b) for XMM 1, this best fit, shown in Figure 5.5(b), seems to be a more accurate fit, but generates a higher χ^2 . Due to the poorly modelled B2 flux (with the largest SNR), this generates a larger χ^2 than the low SNR optical fluxes in XMM 1.

The redshift PDFs, Figures 5.6(a) and 5.6(b), change significantly upon the inclusion of the optical fluxes, however as you can see the redshift actually becomes more poorly constrained. Figure 5.6(b) consists of a single peak at $z \sim 0.75$, while Figure 5.6(a) has a primary peak at $z \sim 1$, with secondary structure up to $z \sim 2.5$. This primary peak does line up with the best fit redshift, and generates a percentile redshift of $1.08^{+0.67}_{-0.07}$. In XMM 1 and 2, the inclusion of the extra data did not change the PDFs, with XMM 3 however there was a clear change, potentially due to the higher SNR of this data *forcing* Le Phare to constrain the fluxes. The $z - A_V$ PDFs, Figures 5.6(c) and 5.6(d) show probable areas that line up with the redshift PDFs, and a most likely A_V that is at $0.24^{+0.17}_{-0.24}$. Looking at Figure 5.6(c) specifically, we note an increase in redshift leads to a slight increase in extinction, in contrast to Figure 1.7 from Caputi et al. (2012). This source generated the lowest SFR, with a value of $4.78^{+20.2}_{-19.8}$.



(a) Postage Stamp Images

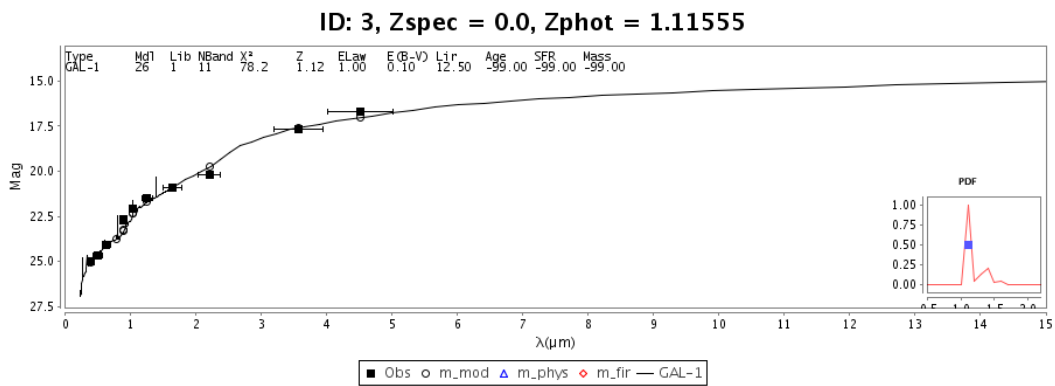


FIGURE 5.5: Two figures for XMM 3, firstly (a) shows postage stamp images reading from the top left in u, g, r, z, Z, Y, J, H, K, B1, B2, $24\mu\text{m}$, H1, H2 and H3, the green circle in each image has a radius of 2 arcseconds. (b) shows the best fit SED.

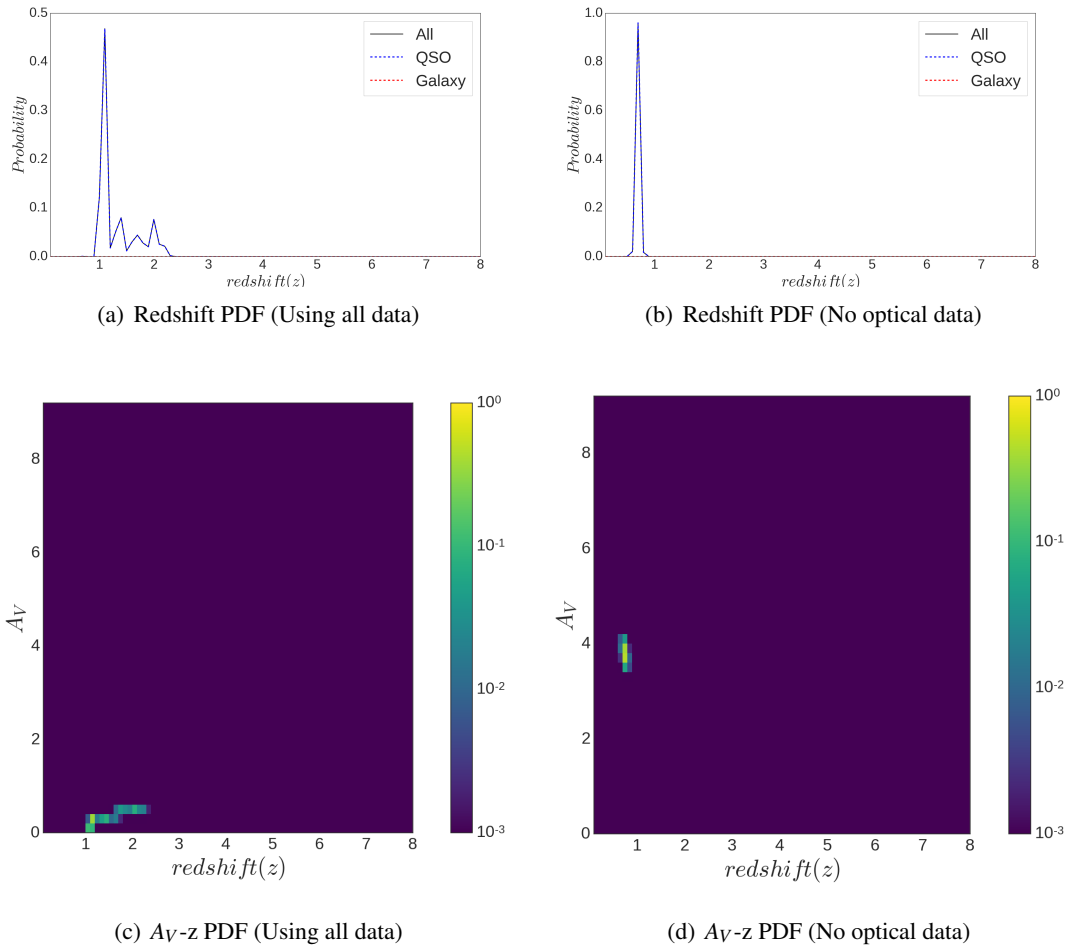


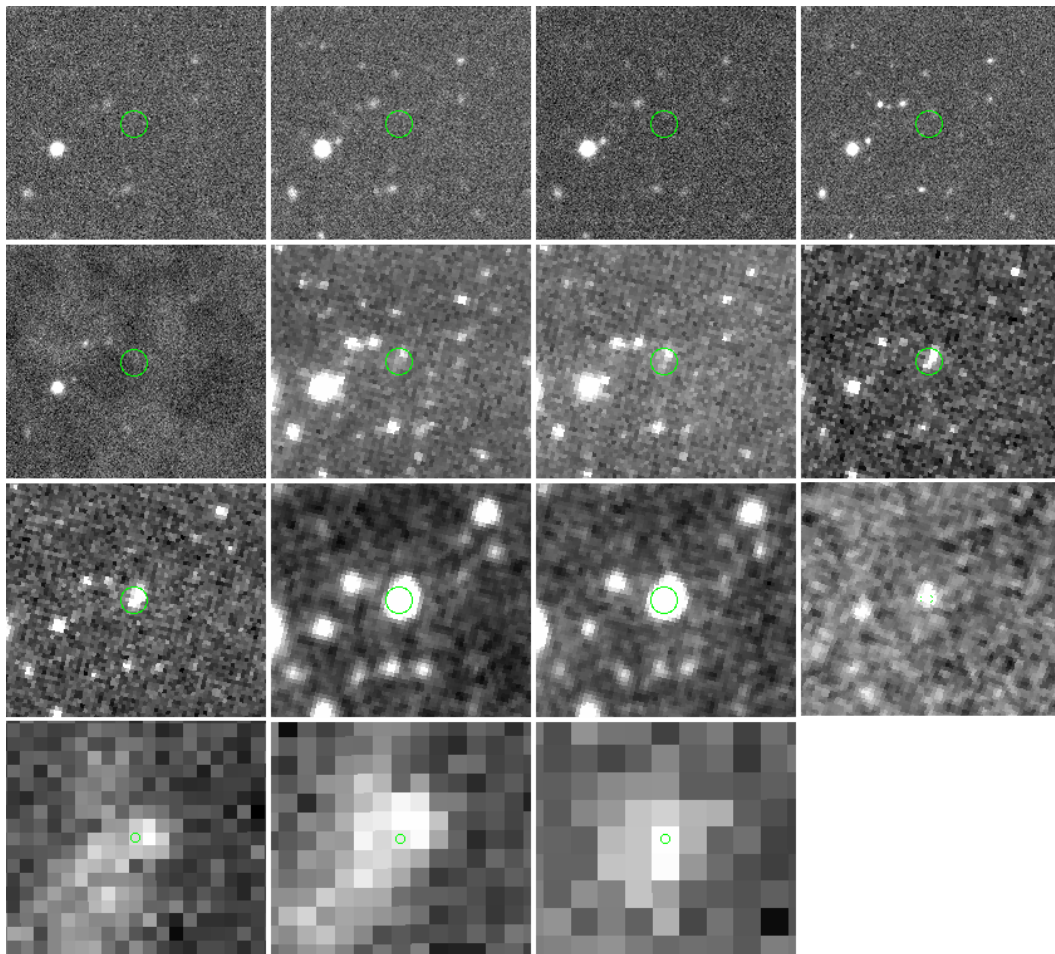
FIGURE 5.6: Four figures for XMM 3; (a) is the redshift PDFs using the optical data and (b) not using the optical data. The black solid line, the blue dashed line and the red dashed line are the probability contributions from all the templates, only the QSO templates, and only the Galaxy templates respectively. (c) and (d) are the redshift(z)- A_V 2-variable PDFs upon using and not using the extra data. The colour-bar indicates the probability in each cell.

5.1.4 XMM 4

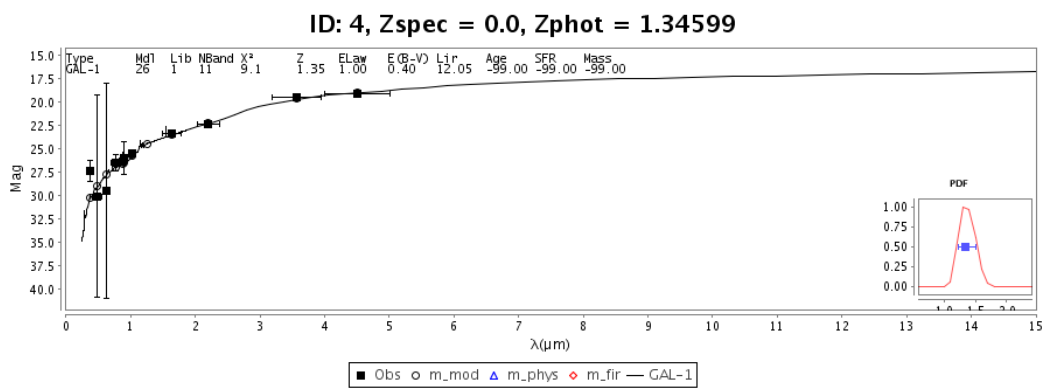
XMM 4 is one of the faintest ERGs in our sample, with a B2 magnitude of 19.03 ± 0.01 , and again relatively blue with a H-B2 colour of 4.24 ± 0.12 . It has coverage in each of the optical bands, good Far-IR fluxes, but no J coverage. Looking at Figure 5.7(a) we can barely see a source in the optical images, and even though this target is relatively isolated, it appears that the source may be extended to the north and west of the VIDEO position, notably the H band, possibly due to a neighbouring source. The HerMES match for XMM 4 is one of the more believable ones, as there are no bright neighbouring sources, and with a separation of 0.81 arcseconds, the area of high intensity lines up in the postage stamps images.

Similar to XMM 3, this source has a best fit redshift of 1.35 and low E_{B-V} value of 0.4, using the SMC law. Looking at Figure 5.7(b), this source uses the Torus Type 2 template from POLLETTA, and again fits the optical section of the SED better.

Looking at Figures 5.8(a) and 5.8(b), we see no difference in the two PDFs upon the inclusion of the extra, optical data. Even though the QSO templates make up the dominant contribution to the redshift PDF, we do notice small galaxy *bump* at $z \sim 1.8$ and a smaller secondary peak at $z \sim 1.7$. The percentile redshift generated from these PDFs is $1.32^{+0.17}_{-0.11}$, which agrees with the best fit value. The $z - A_V$ PDFs (Figures 5.8(c) and 5.8(d)) match the redshift PDFs, and the A_V value of $0.95^{+0.14}_{-0.13}$ which also lines up with the SED best fit solution. The higher redshift peak just below ~ 3 has a higher value for extinction, which does not agree to the relation found in Caputi et al. (2012). With a value of $446.4^{+96.8}_{-67.0}$, this source had the highest SFR in the XMM field.



(a) Postage Stamp Images



(b) SED

FIGURE 5.7: Two figures for XMM 4, firstly (a) shows postage stamp images reading from the top left in u, g, r, i, z, Z, Y, H, K, B1, B2, 24 μ m, H1, H2 and H3, the green circle in each image has a radius of 2 arcseconds. (b) shows the best fit SED.

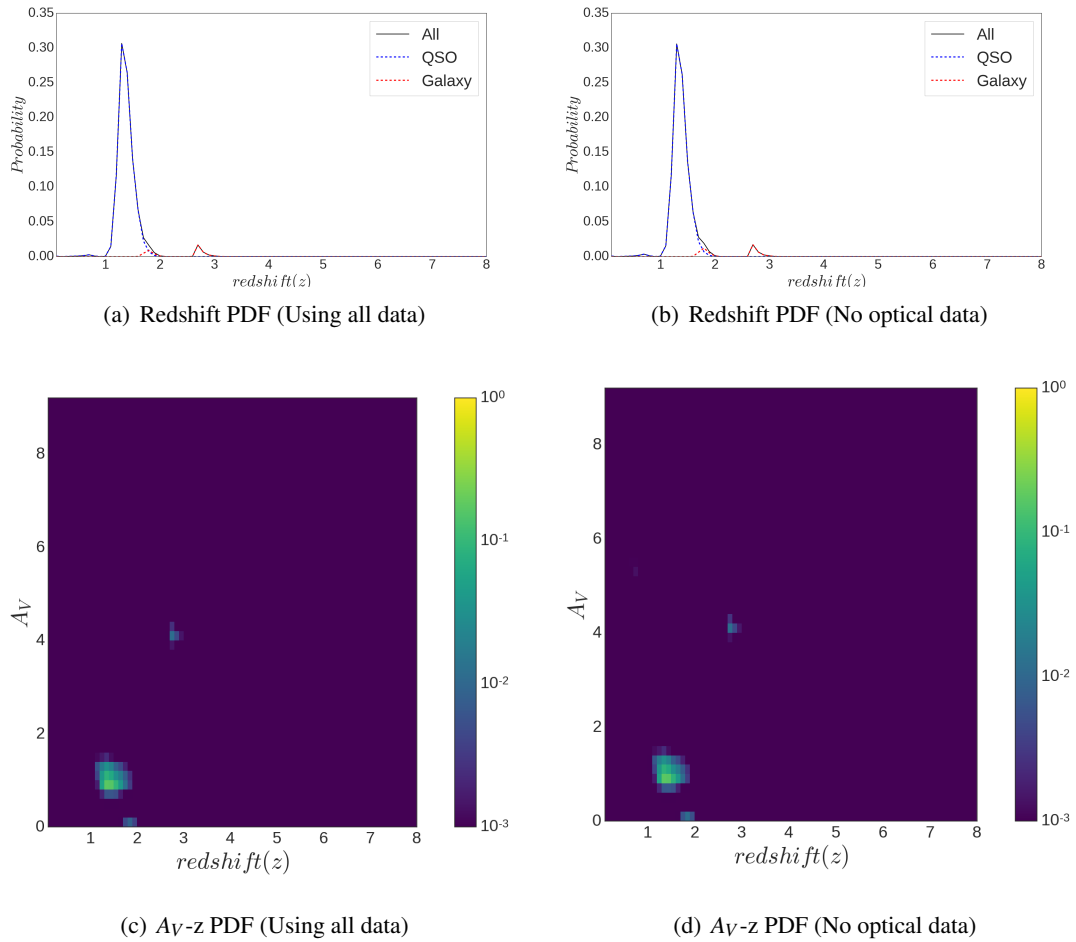


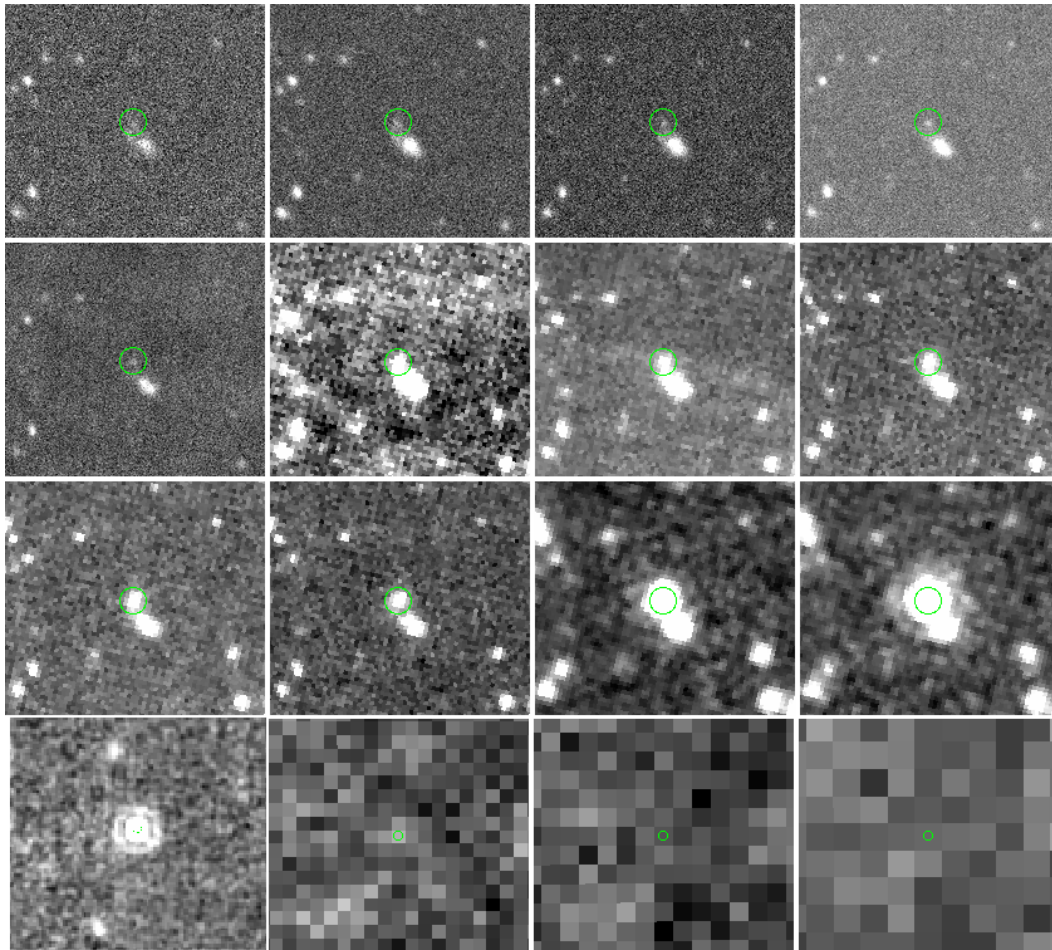
FIGURE 5.8: Four figures for XMM 4; (a) is the redshift PDFs using the optical data and (b) not using the optical data. The black solid line, the blue dashed line and the red dashed line are the probability contributions from all the templates, only the QSO templates, and only the Galaxy templates respectively. (c) and (d) are the redshift(z)- A_V 2-variable PDFs upon using and not using the extra data. The colour-bar indicates the probability in each cell.

5.1.5 XMM 5

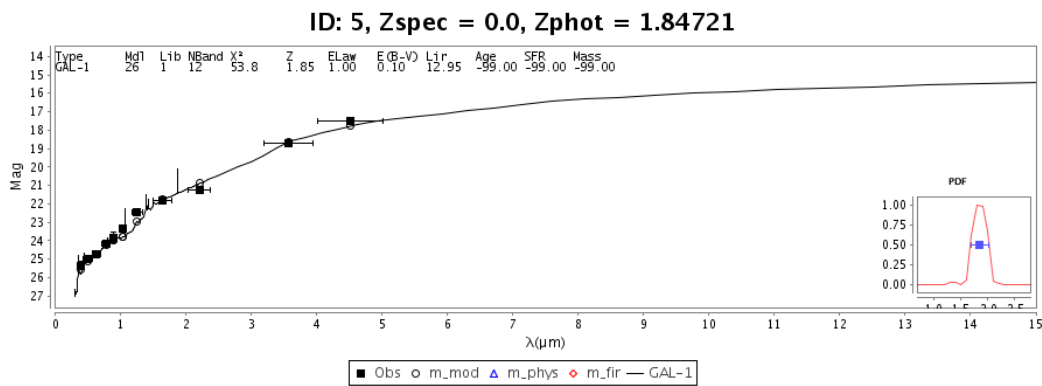
The next source, XMM 5, is the second brightest in our sample with a B2 magnitude of 17.500 ± 0.004 , and has a H-B2 colour of 4.30 ± 0.03 . This source has coverage across all optical and VIDEO bands, and is only missing a H3 flux. Looking at Figure 5.9(a), we can again see a clear source in the optical data, as this target is sufficiently bright. The VIDEO images show a slight blending with a nearby source with increasing wavelength, however the aperture size chosen for this survey was 2 arcseconds, so is sufficiently small to only include intensity from the ERG. In the SERVS images, we see that the source in our sample overwhelms the neighbouring source, therefore it is unlikely that blending from neighbouring sources has a significant influence on our photometry. The HerMES match for this source gave a separation of 0.10 arcseconds, and from Figure 5.9(a) we can see this lines up with a source.

As with XMM 3 and XMM 4, the best fit for this source (Figure 5.9(b)) uses the same Torus template from POLLETTA, generating our highest redshift of 1.85 in the XMM field and lowest E_{B-V} value of 0.1 with the SMC law. Similar to XMM 3, this source matches the optical data well, but does generate a relatively high χ^2 i.e. blending is likely to be an issue.

This source has the largest difference between redshifts when choosing to include the optical data or not, as shown in the two PDFs (Figures 5.10(a) and 5.10(b)). Instead of Le Phare outputting a primary peak at redshift ~ 0.7 , the best fit is at 1.85, again as with XMM 3, this is potentially due to the high SNR of the optical data. The redshift calculated for this source is $1.57^{+0.09}_{-0.06}$, which does not quite line up with the best fit value, while the A_V calculated value of $0.07^{+0.05}_{-0.05}$ shows a similar discrepancy. The contribution from the Galaxy templates for this source, as with all XMM sources so far, is negligible. Finally, looking at the $z - A_V$ PDFs, Figures 5.10(c) and 5.10(d), we see that the probable areas follow the same redshift as the earlier PDFs. This XMM source had an average SFR, with a value of $147.4^{+45.8}_{-43.7}$.



(a) Postage Stamp Images



(b) SED

FIGURE 5.9: Two figures for XMM 5, firstly (a) shows postage stamp images reading from the top left in u, g, r, i, z, Z, Y, J, H, K, B1, B2, 24 μ m, H1, H2 and H3, the green circle in each image has a radius of 2 arcseconds. (b) shows the best fit SED.

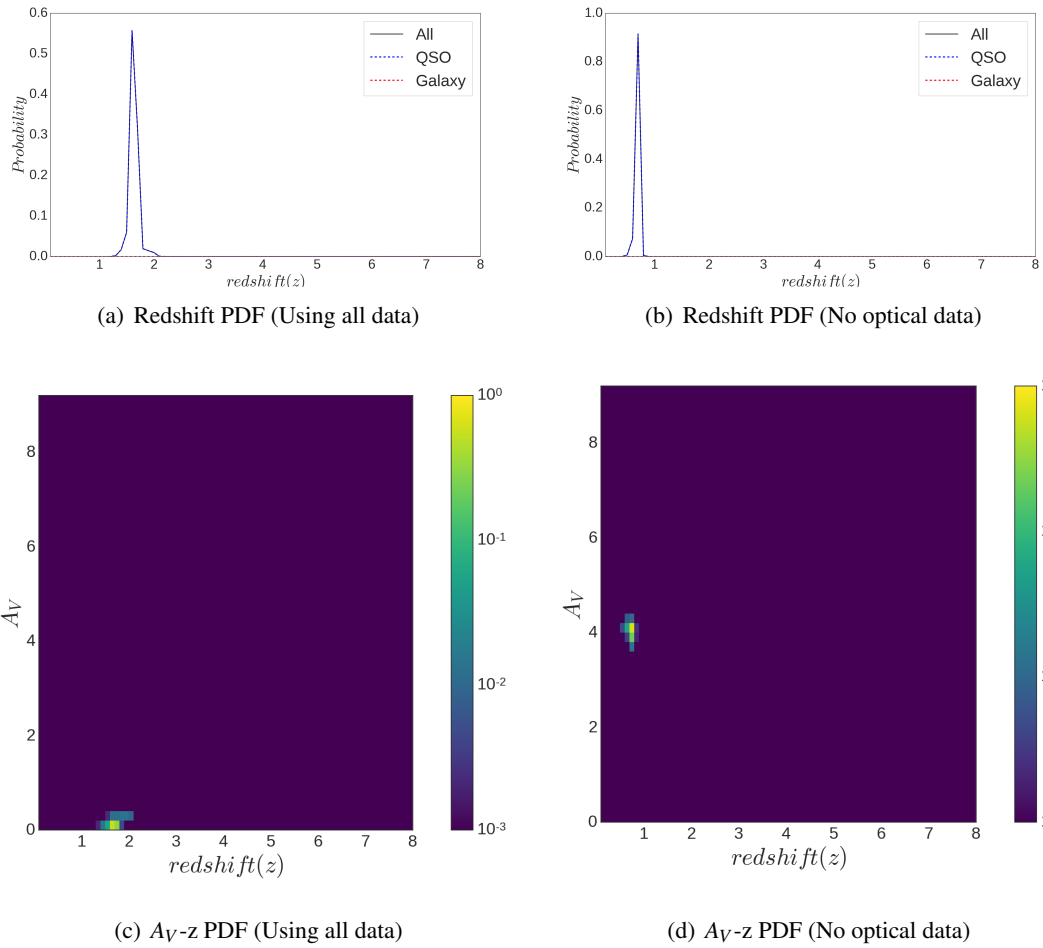


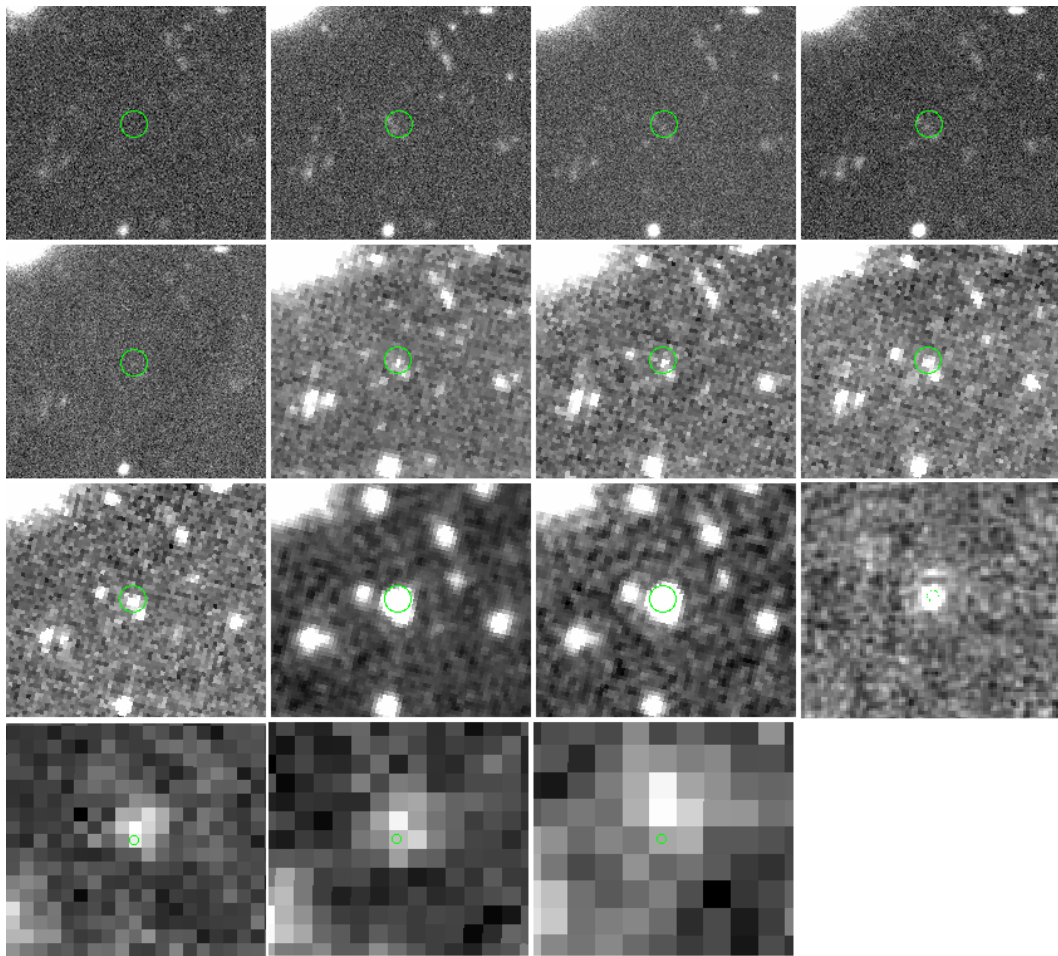
FIGURE 5.10: Four figures for XMM 5; (a) is the redshift PDFs using the optical data and (b) not using the optical data. The black solid line, the blue dashed line and the red dashed line are the probability contributions from all the templates, only the QSO templates, and only the Galaxy templates respectively. (c) and (d) are the redshift(z)- A_V 2-variable PDFs upon using and not using the extra data. The colour-bar indicates the probability in each cell.

5.1.6 XMM 6

Our final source in the XMM field, XMM 6, is relatively faint and blue (with a B2 magnitude of 18.92 ± 0.01 and a H-B2 colour of 4.20 ± 0.11), and has all coverage except in the VIDEO Z band, again due to the XMM3 tile not covering this field. The optical images in Figure 5.11(a) show a very faint source towards the longer wavelengths, with VIDEO however we do notice the source in our sample is potentially contaminated by a neighbouring source. However as earlier, the size of the apertures chosen may help us to mitigate the impact of the neighbouring source, especially since our target overwhelms the nearby one in SERVS. The HerMES match is at a separation of 0.52 arcseconds and does line up with a source in the H1 band image.

This source is one of the most interesting as PAPS actually shows 2 best fit SEDs. This first gives a redshift of 0.30 and E_{B-V} of 1.00, while the second is at a redshift of 1.75 and a E_{B-V} value of 0.1, both using the SMC extinction law. It is interesting as the first fit using the same model as XMM 1 and 2 from Vignali et al. (2011), while the second is the Torus model used to fit XMM 3, 4, and 5. The fact that this source is relatively faint means we cannot determine which of the fits is more likely. This is likely due to the similarity of the templates at NIR wavelengths, but also due to the low SNR of the u band flux (the area where the templates most differ).

When examining the two PDFs, in Figures 5.12(a) and 5.12(b), we note that both have 3 peaks at approximate redshifts of 0.3, 1.2 and 1.8, and when including the optical data, the strength of these peaks changes. The best fits in Figure 5.11(b) gave a lower χ^2 for the higher of the two redshifts, however the PDF including all the data shows the primary peak as the lowest of the three redshifts. In contrast, the PDFs without the extra data shows the peak at redshift 1.2 as the primary one. There is a strange feature in Figure 5.12(a), a constant probability for redshift beyond $z \sim 3.5$, due to the fact that the templates are truncated at short wavelengths. We will discuss this in more detail in §6.2. The redshift we calculated using our method is $1.77^{+4.61}_{-1.61}$, while the A_V calculated is $0.99^{+1.00}_{-0.58}$. The large error in this value comes from the extra structure as mentioned, but also from the multiple peaks with similar strengths. As with many sources in the XMM field in our sample, there is a negligible addition from the Galaxy templates. When looking at Figures 5.12(c) and 5.12(d), the PDFs for the $z - A_V$ plane, we see that they match the redshifts from the best fits. We can also see with this source how the extra data tightens the probability of the redshift - extinction, however it does generate a more obvious constant probability above $z \sim 3.5$. The SFR rate for this source is the second highest in the XMM field, with a value of $390.0^{+168.1}_{-383.2}$.



(a) Postage Stamp Images

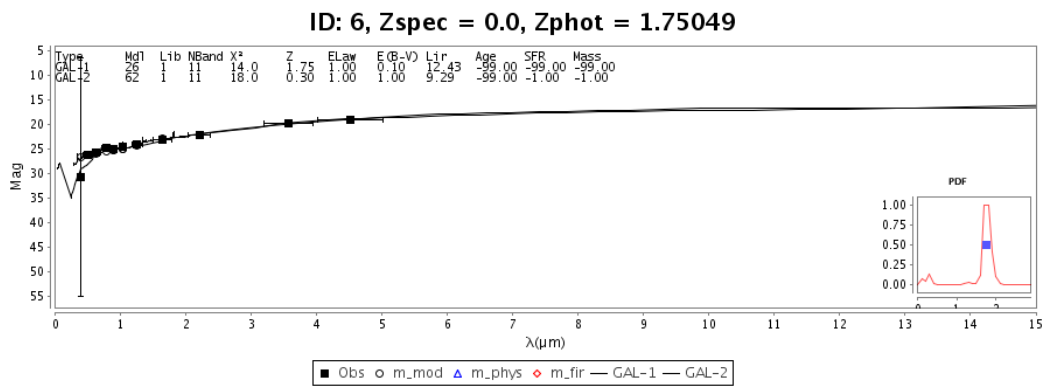


FIGURE 5.11: Two figures for XMM 6, firstly (a) shows postage stamp images reading from the top left in u, g, r, i, z, Y, J, H, K, B1, B2, 24 μ m, H1, H2 and H3, the green circle in each image has a radius of 2 arcseconds. (b) shows the best fit SED.

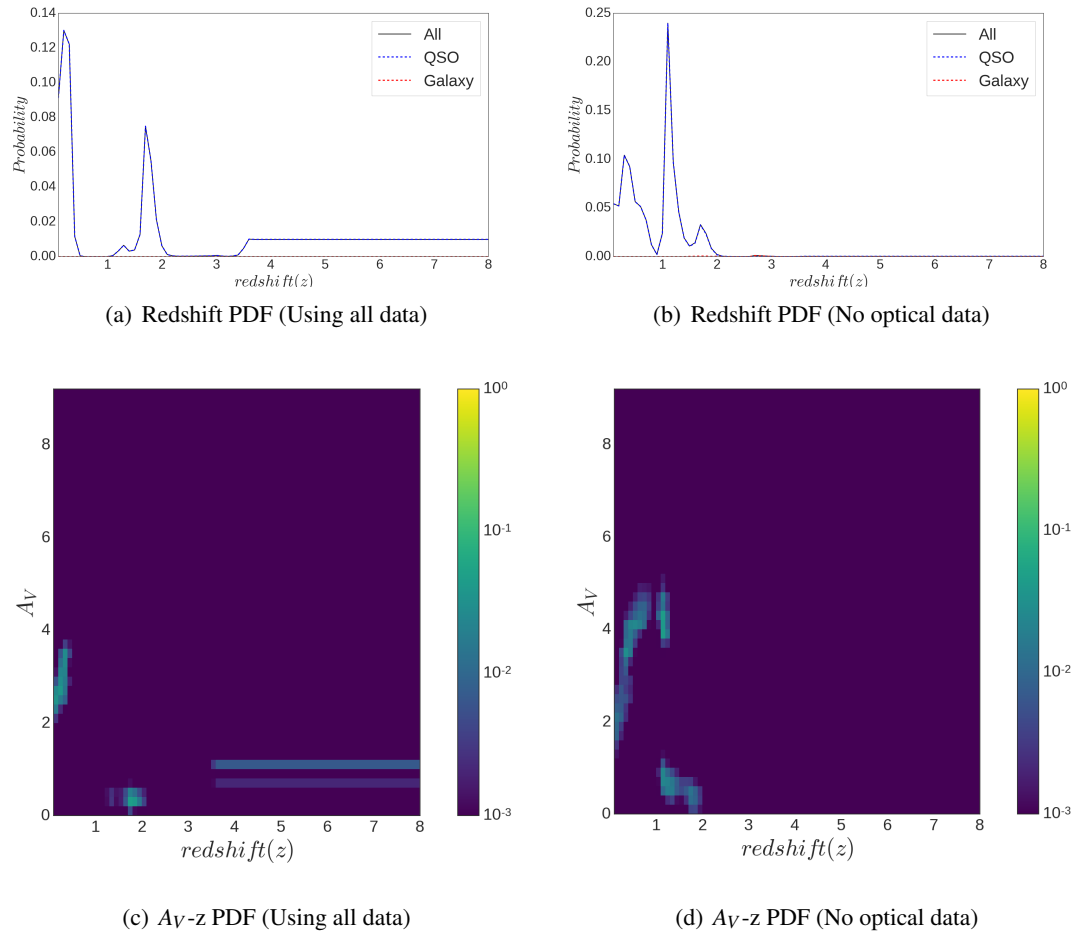
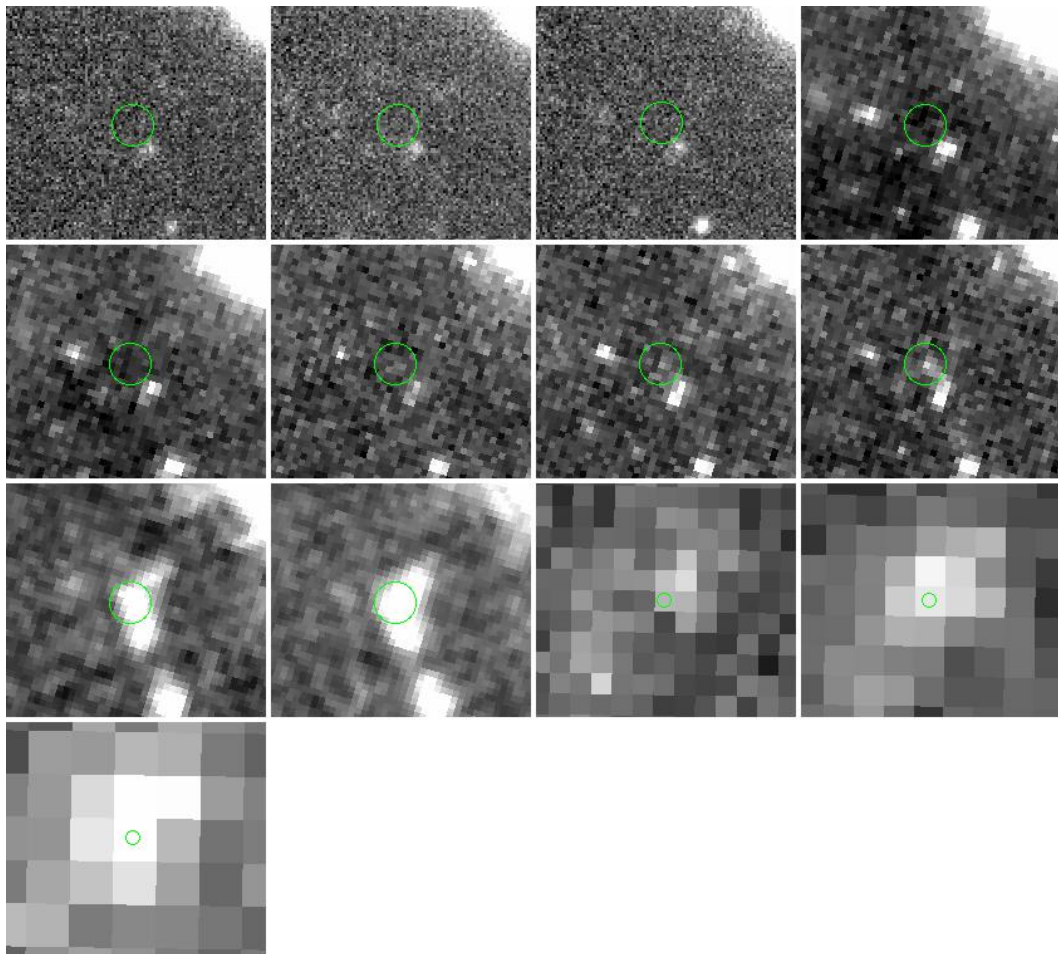


FIGURE 5.12: Four figures for XMM 6; (a) is the redshift PDFs using the optical data and (b) not using the optical data. The black solid line, the blue dashed line and the red dashed line are the probability contributions from all the templates, only the QSO templates, and only the Galaxy templates respectively. (c) and (d) are the redshift(z)- A_V 2-variable PDFs upon using and not using the extra data. The colour-bar indicates the probability in each cell.

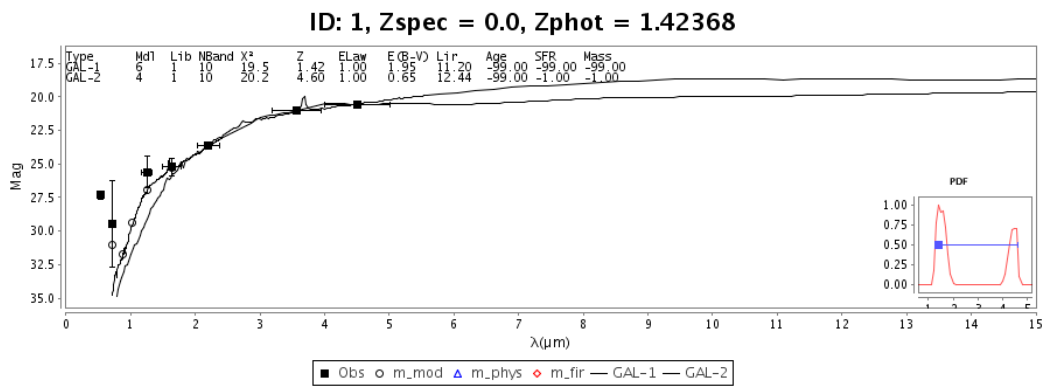
5.1.7 ES1 1

The first source in the ES1 field, ES1 1, is the faintest and second reddest source in our sample, with a B2 magnitude of 20.53 ± 0.03 and a H-B2 colour of 4.68 ± 0.65 , but also has the highest error on this value. The extra data from ESIS, provided by Mattia Vaccari, covered both the sources in our sample in the ES1 field, however the two sources were too faint to be present in the catalogues. As discussed, we extracted fluxes using APT and averaged around the source to generate flux uncertainties. The flux extracted for the v, Z, and Y bands gave us the first negative fluxes in our sample, they do not correspond to a negative intensity, rather the influence of noise in the image on a small intrinsic flux density creates a negative value. ES1 1 is also the only source in our sample that does not have a HerMES match within 5 arcseconds, even though it is covered by the field and does seem to have a source in the centre of the H1, H2, and H3 images, therefore it is also the only source without a SFR.

Negative fluxes do not generate a magnitude as it is based on a logarithmic scale, and from looking at Figure 5.13(b) you can see therefore that they are not shown in the SED fitting. We tested their inclusion by running Le Phare with negative fluxes against setting the code to assume no coverage in these bands. We found that that outputs were identical, leading us to the conclusion that Le Phare does not include negative flux values in its fitting. Due to the faintness of this source, it also has most poorly constrained redshift in our sample. When looking at Figures 5.14(a) and 5.14(b) we can see two evident peaks, as well as a large probability tail at $z > 4$. These peaks correspond to best fit redshifts of 1.42 and 2.50, with E_{B-V} values of 1.95 and 1.25 respectively, with the tail starting at a redshift $\gtrsim 4.60$ and $E_{B-V} \lesssim 0.65$. The percentile redshift for this source is $2.76_{-1.23}^{+4.04}$, although it does not tell us much about the target, with the A_V value of $3.10_{-1.88}^{+1.82}$ containing similarly large errors. We note that this is the first source in our sample where the Galaxy templates are more probable than the QSO templates. The inclusion of the optical data for this source does change the PDF marginally, however we can't draw any conclusions on its effectiveness, potentially due to Le Phare not constraining the SED to the optical data very well, as seen in Figure 5.13(b). The best fit SED is shown in Figure 5.13(b), corresponding to the starburst model for NGC 6090 in the Polletta package (Polletta et al., 2007), however all the χ^2 values for the best fit in each package were between 19 and 21. The extra PDFs, Figures 5.14(c) and 5.14(d), don't add much more information, however we do notice the constant redshift probability has a similar structure to XMM 6. It is noted that for this source, the higher redshift peaks correspond to lower extinctions, in a similar fashion to the relation found in Caputi et al. (2012).



(a) Postage Stamp Images



(b) SED

FIGURE 5.13: Two figures for ES1 1, firstly (a) shows postage stamp images reading from the top left in b, v, r, Z, Y, J, H, K, B1, B2, H1, H2 and H3, the green circle in each image has a radius of 2 arcseconds. (b) shows the best fit SED.

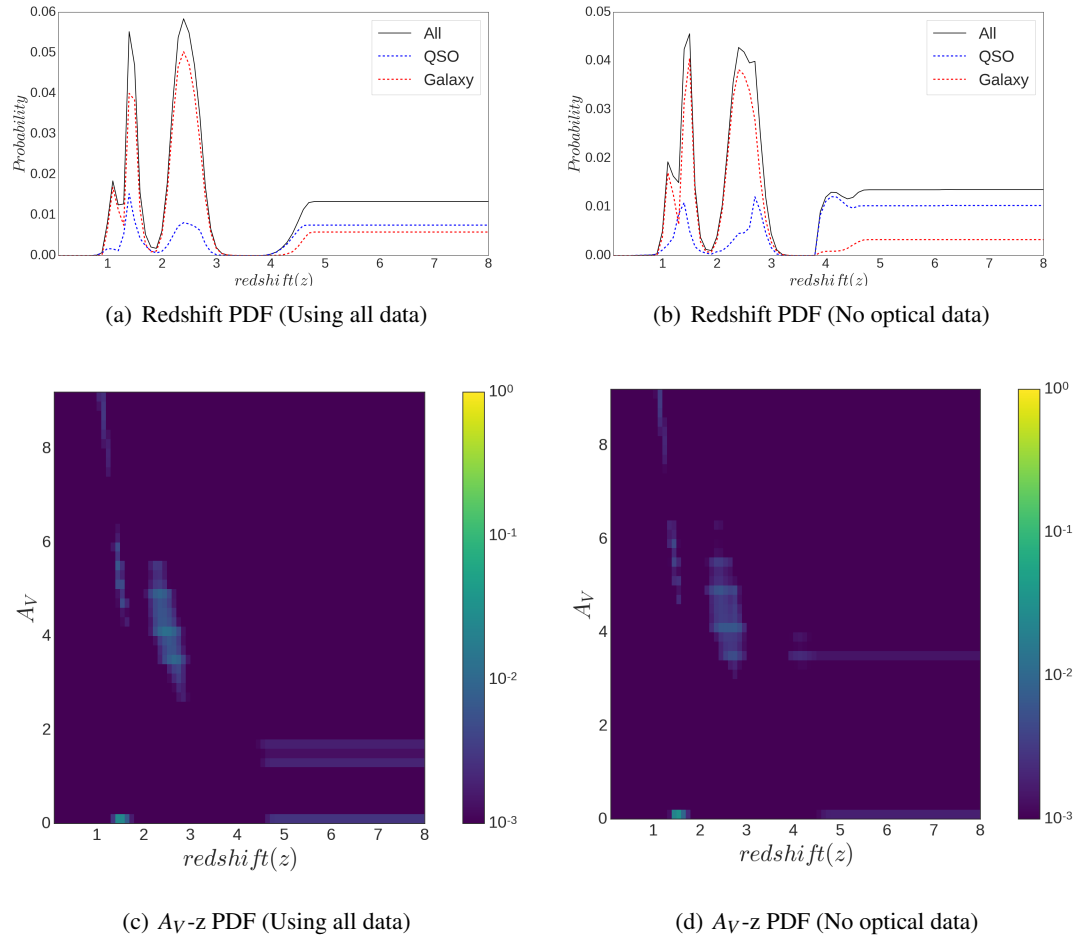
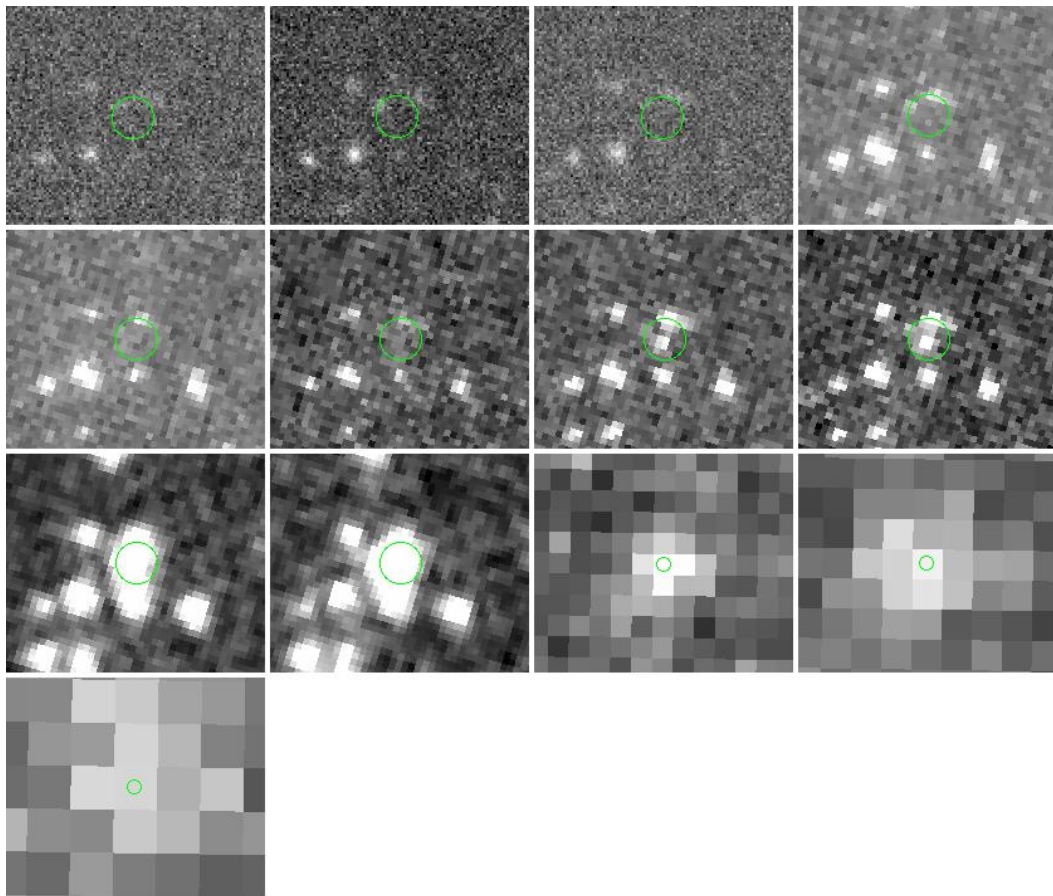


FIGURE 5.14: Four figures for ES1 1; (a) is the redshift PDFs using the optical data and (b) not using the optical data. The black solid line, the blue dashed line and the red dashed line are the probability contributions from all the templates, only the QSO templates, and only the Galaxy templates respectively. (c) and (d) are the redshift(z)- A_V 2-variable PDFs upon using and not using the extra data. The colour-bar indicates the probability in each cell.

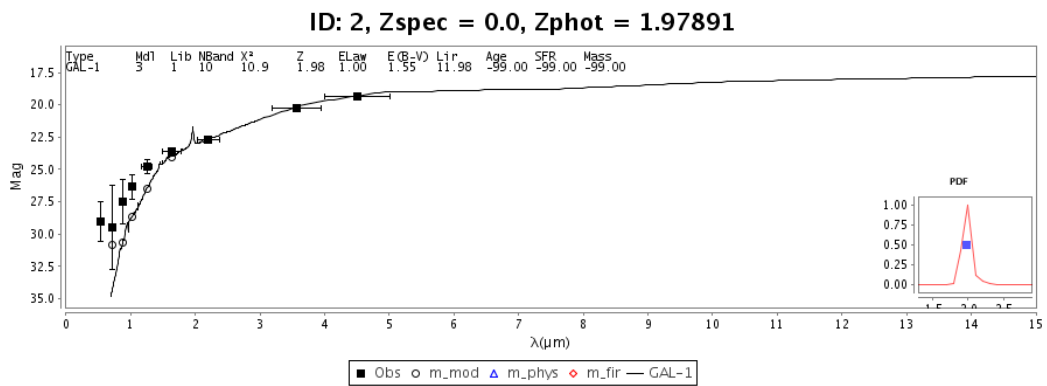
5.1.8 ES1 2

ES1 2 is lot brighter and slightly bluer than ES1 1 (with a B2 magnitude and H-B2 colour of 19.33 ± 0.02 and 4.28 ± 0.15 respectively), and only has one negative flux in the v band. It was still too faint to be present in the extra catalogues obtained, however the extracted fluxes in b and r are believable, even if they have low SNR. Looking at Figure 5.15(a) we can see that the targeted source is most evident in the K and H band. However due to the extreme redness, the B1 and B2 images show some contamination from neighbouring sources. The HerMES match is at 0.04 arcseconds, and looking at the respective bands, there is definitely a strong source, however it is potentially a merging of nearby sources.

Putting aside concerns about the impact of nearby sources on the photometry, this source is a lot better constrained, with a redshift estimate, again using the percentiles from the PDF of $2.06^{+0.07}_{-0.05}$, and even though the optical data does not fit the best SED well, as shown in Figure 5.15(b), it tightens the PDF generated with the inclusion of the data, as seen when comparing Figures 5.16(a) and 5.16(b). ES1 2 seems that it is more likely to be best modelled by Galaxy templates, owing to the greater contribution from them in Figure 5.16(a), however the best fit shown in Figure 5.15(b) is actually based on a hybrid model in the MARA package. The more prominent peak from the Galaxy templates, as shown in Figure 5.16(a), comes from a instantaneous starburst model in the BC03 package, with an age of 640 Myrs and metallicity of 0.05. These two fits are at redshifts of 1.98 and 2.13, and E_{B-V} values of 1.55 and 1.65 respectively. The last two graphs for this sources, Figures 5.16(c) and 5.16(d), show more conclusively that the extra data tightens the probability $z - A_V$ plane, and generates a A_V value of $4.19^{+0.16}_{-0.29}$. This source had the highest H1 flux, and generated the highest SFR rate in our sample, with a rate of $1046.5^{+106.1}_{-109.0}$.



(a) Postage Stamp Images



(b) SED

FIGURE 5.15: Two figures for ES1 2, firstly (a) shows postage stamp images reading from the top left in b, v, r, Z, Y, J, H, K, B1, B2, H1, H2 and H3, the green circle in each image has a radius of 2 arcseconds. (b) shows the best fit SED.

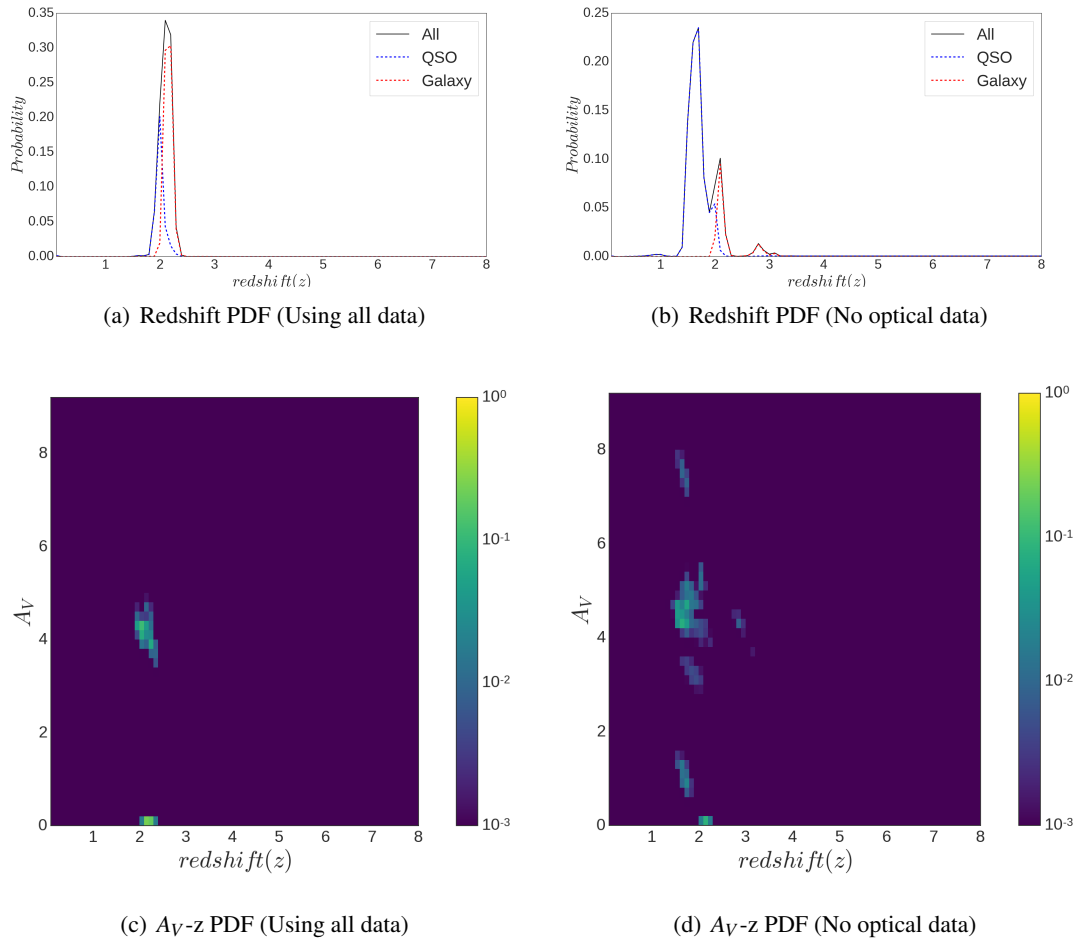
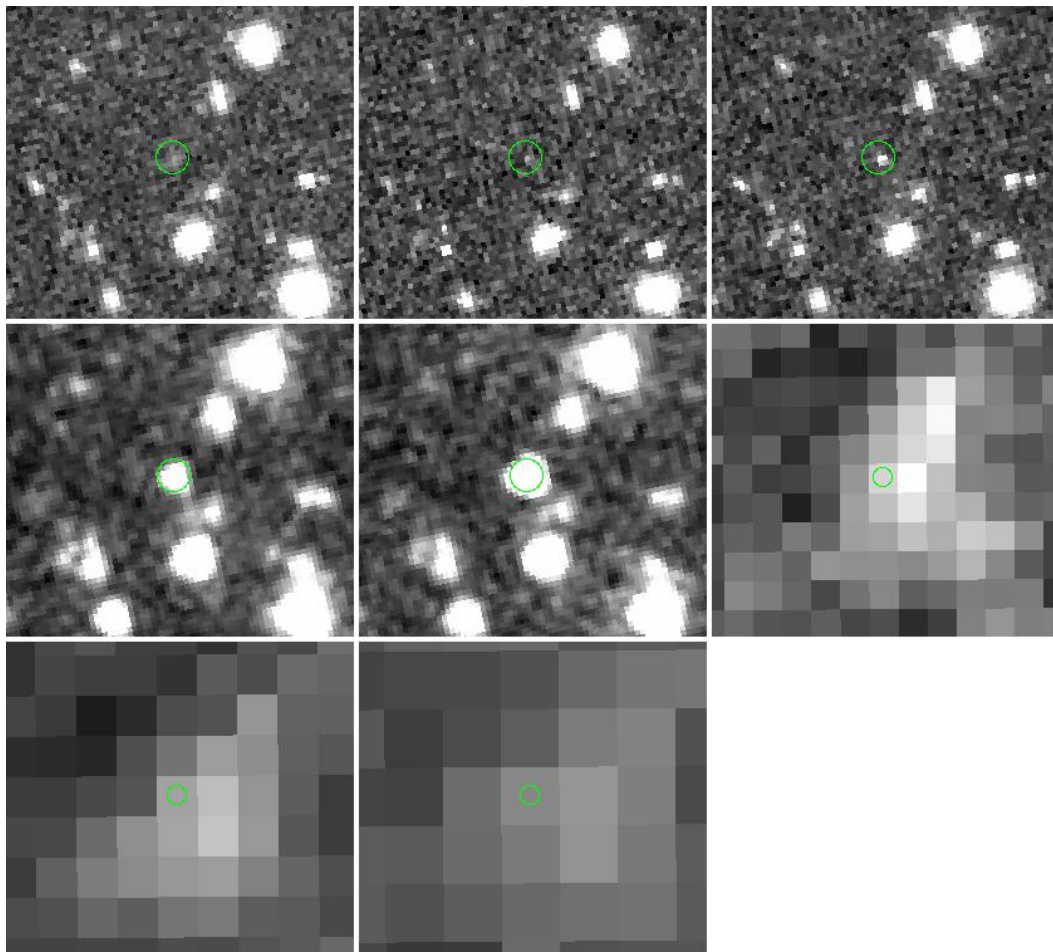


FIGURE 5.16: Four figures for ES1 2; (a) is the redshift PDFs using the optical data and (b) not using the optical data. The black solid line, the blue dashed line and the red dashed line are the probability contributions from all the templates, only the QSO templates, and only the Galaxy templates respectively. (c) and (d) are the redshift(z)- A_V 2-variable PDFs upon using and not using the extra data. The colour-bar indicates the probability in each cell.

5.1.9 CDFS 1

The last source in our sample is also the only one in the CDFS field, it is the second faintest source with a B2 magnitude of 19.51 ± 0.01 , and has the 3rd reddest H-B2 colour of 4.60 ± 0.18 . CDFS 1 has the least amount of data for any source in our sample, as there is no coverage in any optical survey and also it lies in an area where both the Z and Y bands do not cover. Looking at Figure 5.17(a), the target is isolated, and has a match to a HerMES source at a separation of 0.03 arcseconds. The Herschel images do show a source at the centre, however is likely to be from many nearby targets.

This source has 3 best fit peaks and unlike ES1 1, the χ^2 values from each best fit are sufficiently varied so we can identify what the peaks correspond to. CDFS 1 has two QSO peaks at redshifts of 1.24 and 2.43 corresponding to E_{B-V} values of 1.80 and 0.40, and one galaxy peak at redshift 3.39 and E_{B-V} 1.90. The SED fit with the lowest χ^2 (corresponding to the lower redshift QSO peak), as shown in Figure 5.17(b), is again the Type 2 QSO from the VARIOUS package that models IRAS 09104+4109, while the higher redshift peak is the best fit from the Type 2 QSO in the POLLETTA package. The 3rd peak in the PDF for as mentioned is a galaxy template from the POLLETTA that models Sc spiral galaxy. The redshift calculated for this source is $2.84^{+1.03}_{-0.48}$, calculated from the percentiles from the PDF shown in Figure 5.18(a). The same method generated an A_V value of $5.29^{+0.59}_{-0.71}$. We do note a constant probability beyond redshift 4, similar to XMM 6 and ES1 1 in Figure 5.18(a), however it is not present in Figure 5.18(b). The $z - A_V$ PDF in Figure 5.18(b) shows likely locations for the redshifts and extinctions that lines up with all the peaks shown in Figure 5.18(a). We note the red-lined Galaxy sub-peak lines up with the extinction peak below $A_V \sim 0.5$, however is of slightly smaller strength than the QSO peak at an extinction value of ~ 5 . CDFS 1 generated the highest redshift in our sample, and had a relatively average H1 flux, which lead to the second highest SFR value of $687.1^{+291.2}_{-213.8}$.



(a) Postage Stamp Images

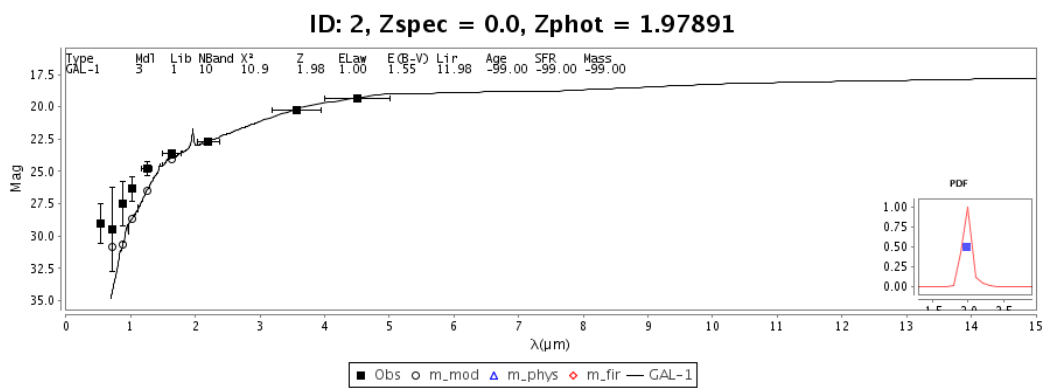
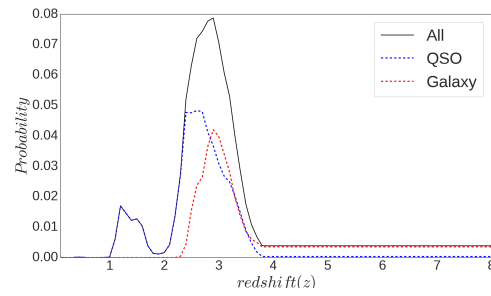


FIGURE 5.17: Two figures for CDFS 1, firstly (a) shows postage stamp images reading from the top left in J, H, K, B1, B2, H1, H2 and H3, the green circle in each image has a radius of 2 arcseconds. (b) shows the best fit SED.



(a) Redshift PDF

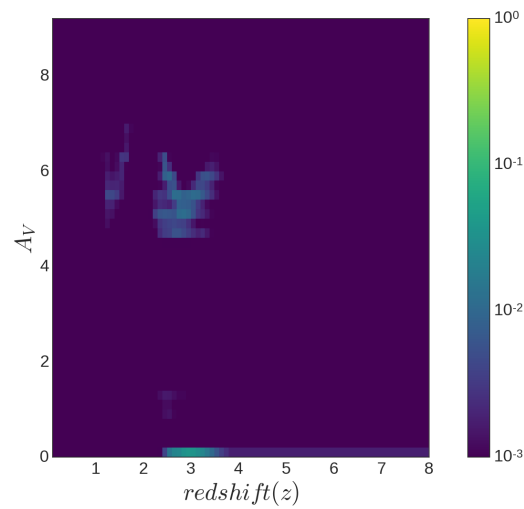
(b) A_V - z PDF

FIGURE 5.18: Two figures for CDFS; (a) is the redshift PDF, with the black solid line, the blue dashed line and the red dashed line are the probability contributions from all the templates, only the QSO templates, and only the Galaxy templates respectively. (b) is the redshift(z)- A_V 2-variable PDF with the colour-bar representing the probability.

Chapter 6

Discussion

6.1 What are the Reddest Galaxies in the Universe?

In applying a $H - B2 > 4$ colour cut to all sources in the VIDEO survey, we attempted to identify the brightest, reddest galaxies. As shown in §1.4, the sample in Caputi et al. (2012) contained 17 ERGs, $\sim 23\%$ at low redshift between $0.7 < z < 1$ with $A_V > 5.0$, $\sim 65\%$ in the middle sub-sample between $3 < z < 5$ and $1.1 < A_V < 4.2$, and finally $\sim 12\%$ greater the 6 redshift with extinction values ~ 1 . Our sample of sources has an average B2 magnitude of 18.67 ± 0.01 , which in comparison to the average of the sample in Caputi et al. (2012) of 22.42 ± 0.03 , is significantly brighter. These ERGs are thought to be the some of the rarest galaxies in the Universe, so as discussed earlier, we made use of surveys covering ~ 4 times the area as Caputi et al. (2012).

The first thing to note when looking at the best fits of our sample of sources, is that the brightest 6 sources (the 6 in the XMM field), are QSOs and not fit with Galaxy templates. We can see this from the fact that the best fit templates are all QSO models, and from the redshift probability density functions for each source, shown in Figures 5.2(a), 5.4(a), 5.6(a), 5.8(a), 5.10(a), and 5.12(a). The contribution to the redshift probability density function from the Galaxy templates are negligible for these sources, meaning that as well as the fact that the best fit for each source is a QSO, the probability that they are not modelled by Galaxy templates is approaching 100%. It is important to investigate which templates are used for these best-fit solutions, and as shown Le Phare outputs only two best models for the XMM sample of sources. These are the Type 2 dusty Torus template, from the POLLETTA package, used to model SWIRE J104409.95+585224.8 in Polletta et al. (2006) and the Type 2 QSO template that models IRAS 09104+4109 in Vignali et al. (2011). On the other hand the 3 faintest sources in our sample, the 2 in the ES1 field and the 1 in the CDFS field, were not found to be modelled exclusively by QSO templates. Figure 5.14(a), the PDF for ES1 1, is the least well constrained, but based on our data and the Le Phare

fitting is more likely a galaxy than a QSO. ES1 2 is best modelled by a QSO template but is more likely a galaxy, as seen in Figure 5.16(a). We note that the best fit QSO template used for this source is a hybrid model, and the galaxy template is a instantaneous starburst model, a clear change from the first 6 sources in our sample. The final source in our sample, CDFS 1, is similar to our sample of sources from XMM, as the 2 best fit QSOs use the same two Type 2 models. There is a smaller galaxy peak in the PDF generated from a starburst model, a similar template used to generate the galaxy peak in the PDF for ES1 2.

All the best fit models that are used to fit all our sources in our sample, along with the output parameters, are shown in Table 5.2 The ERGs found in our sample of galaxies are among the reddest, brightest objects in the universe, and are extremely rare. We chose Le Phare to make use of lots of QSO and Galaxy templates, and ran the fitting with a large range of redshifts and extinctions, however any problems with the fittings and output parameters will be discussed in in the following section.

6.2 Redshifts and Extinctions

The most important parameter that we used Le Phare to estimate was redshift. All of our sources are found to have best fit solutions between $0.4 < z < 3.0$, and looking again at Figures 5.2(a), 5.4(a), 5.6(a), 5.8(a), 5.10(a), 5.12(a), 5.14(a), 5.16(a), and 5.18(a), you can see the most likely redshifts for each source. There were two ways in which we recorded the redshifts; firstly the best fits from the individual fit from Le Phare, and secondly the percentiles of the redshift distribution, both shown in Table 5.2 (see §4.3). 78% of our sample of sources (XMM 1, XMM 2, XMM 3, XMM 4, XMM 5, ES1 2, and CDFS1) gave a primarily single peaked PDF that lines up with the best fit solution output from Le Phare. This group can be further spilt into redshift sub-groups of 2 sources (22% of the full sample) at $0 < z < 1$, 3 sources (33%) between $1 < z < 2$ and 2 sources (22%) at $2 < z < 3$. The last two sources in our sample (XMM 6 and ES1 1) are less well constrained, however XMM 6 is most likely in the 1st redshift range, while ES1 1 is equally probable to be in the 2nd and 3rd range. This is in direct contradiction with Caputi et al. (2012) as only 25% of the sources in their sample were below a redshift of 3 compared to our result that all sources are much more likely to lie below a redshift of 3. Caputi et al. (2012) also showed an inverse correlation between redshift and extinction for the ERGs, i.e. the high redshift sub-sample of sources had low extinction values and vice-versa. Looking at the best fit A_V values output from Le Phare, even though all the sources are found to be low redshift, relative to Caputi et al. (2012), the E_{B-V} values vary significantly; they range between 0.10 and 1.95 (corresponding to A_V values between 0.27 and 7.90). By following Caputi et al. (2012), we generated probability density functions in 2 dimensions, both extinction and redshift as shown in Figures 5.2(c), 5.4(c), 5.6(c), 5.8(c), 5.10(c), 5.12(c), 5.14(c), 5.16(c), and

5.18(b), giving us more insight into where our sources lie on this plane. Looking at these most probable locations for the redshift/extinctions we see that 3 sources are between $0.0 < A_V < 2.0$, 2 between $2.0 < A_V < 4.0$, 3 between $4.0 < A_V < 6.0$, 0 with $A_V > 6.0$, and XMM 6 either in the 1st or 2nd extinction range depending on the best fit chosen (though more likely in the 2nd based on the strength of the redshift PDF peak).

The $z - A_V$ PDF is a good way to see where the most likely redshifts and extinctions lie, however there are features present for each source that need to be explored. The main irregular feature that stands out is present 3 sources (XMM 6, ES1 1, and CDFS 1) beyond ~ 3 redshift, and upon further investigation was visible, but not statistically significant, unless we showed very low probabilities. This feature is a constant probability relation to extinction, across all redshifts $\gtrsim 3$. The reason behind this relates to the discussion in §6.1; the fact that Le Phare’s best fits only make use of 2 QSO templates. These templates are fairly simple, but are also truncated below a specific wavelength. Upon the manual inspection of the SED files that come with Le Phare, we noticed that the templates that Le Phare used for the best fits’ started at $\sim 0.1 \mu m$, so when they were redshifted up the optical data lay outside of the range. This led to the conclusion that all redshifts are equally likely beyond ~ 3 . Looking at the $z - A_V$ PDF taken from Caputi et al. (2012) (Figure 1.7), we can see that there is an approximate $A_V \propto \frac{1}{z}$ relation for the probability of some of the sources. Herein lies another difference between Caputi’s sample and most of our sample, only XMM 4 has two areas in the $z - A_V$ PDF that have an inverse relation, where as a few show the opposite relation, notably ES1 1. This is potentially due to the fact that Caputi’s sources were extremely faint whilst ours are approximately 3.75 magnitudes brighter. Bright galaxies are less likely to be at extremely high redshifts ($\gtrsim 2$), so our sources are much more likely to be extremely red due to very large extinction (as deduced so far).

In addition to extracting galaxies with colours of $H - B2 > 4$, Caputi et al. (2012) postulated the use of 2 other NIR bands to potentially determine which ERGs were at $z > 6$, before any SED fitting was carried out (as shown in Figure 1.4). To explore this we generated two new graphs with the same axes. Figure 6.1 is a copy of Figure 1.4, with the original Caputi et al. (2012) data present, along with our sample of sources. As you can see from Figure 6.1, only CDFS 1 for our sample does **not** lie in the $H - K_s \lesssim 1.7$, $K_s - [3.6] \gtrsim 2.1$ area in the top left of the graph. Again due to the fact that all our sample of sources are at $z < 3$ seems to either in-validate the postulated extra colour cut from Caputi et al. (2012) or show that it does not work for all ERGs, especially the extremely bright ones in our sample. Figure 6.2 is the same colour-colour plot as Figure 6.1, however all sources present in the VIDEO and SERVS catalogue that have 5σ detections in H, K_s , B2, and B2 are plotted. You can see that our sample of sources does occupy a particularly irregular section of the plot, compared to the majority of the survey.

As mentioned earlier in §1.4, Wang et al. (2015) also attempted to apply an extra colour-cut using the the NIR bands we have used here, to split their sources into 2 further sub-groups.

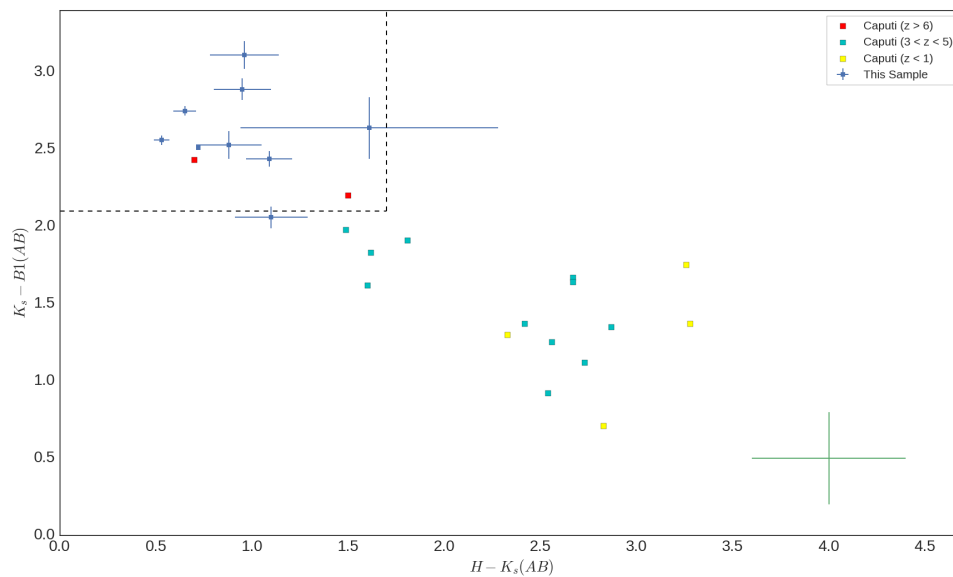


FIGURE 6.1: Copy of Caputi Colour-Colour Plot with our sample of sources

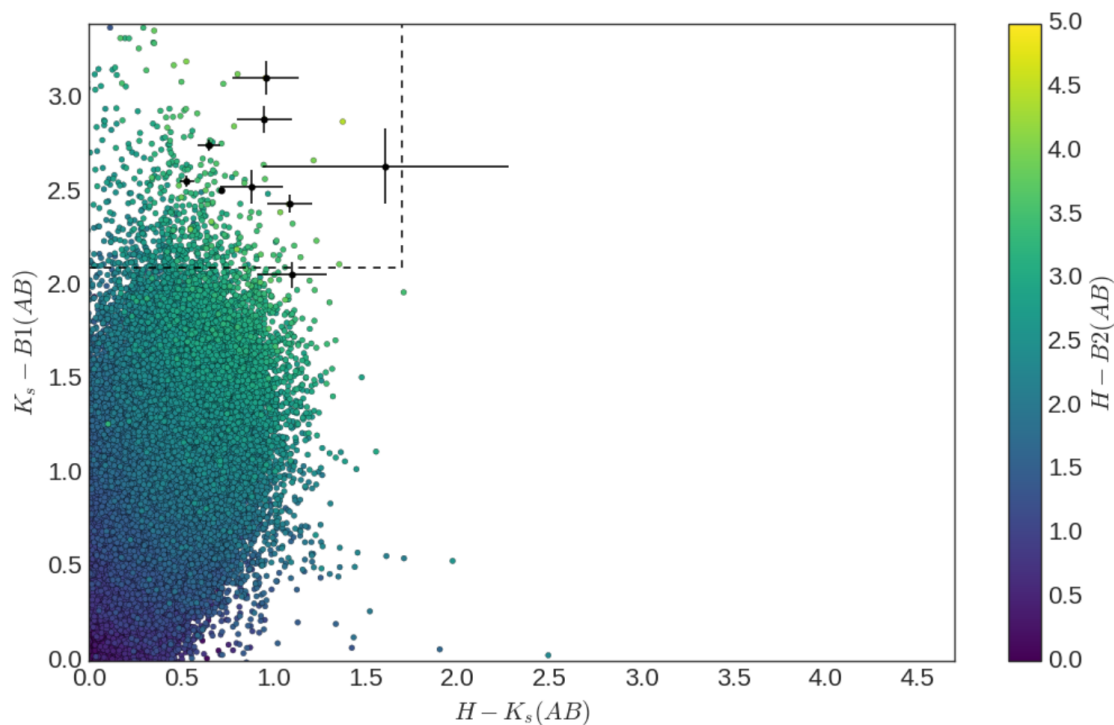


FIGURE 6.2: Same Colour-Colour Plot as Caputi (as shown in Figure 1.4) but with all sources in VIDEO Survey with our sample shown in black. This graph has the same axis limits to show the comparison to Figure 6.1, as well as the postulated area for high redshift ERGs as discussed in §6.2.

They first extracted all sources with $H - B2 > 2.25$ (the same colour as this work and Caputi, but a different limit), then using the extra J band, split the sample into JH-blue and JH-red. The dashed line, shown in Figure 1.5, separates these two groups, and is given by:

$$\begin{aligned} JH - blue : H - B2 &> 2 \times (J - H) + 1.45 \\ JH - red : H - B2 &\leq 2 \times (J - H) + 1.45 \end{aligned} \tag{6.1}$$

Wang et al. (2015) showed that by using this cut, the JH-blue group was made up of a larger proportion of sources with $z > 3.0$, while JH-red had more with $z < 3.0$. As you can see in Figure 1.5, the JH-blue sources have very small J-H colours often below 0, and due to the extreme extinction present, our sample of sources have small positive J-H colours, between 0.1 and 1.1. Due to the extremely large $H - [4.5]$ colours these ERGs would therefore technically lie in the JH-blue sub-group, however they are much more irregular than the sample presented in Figure 1.5 and lie to the top of the graph. Our sample of sources all gave best fits at $z < 3$, in contradiction to the postulated colour cut shown in Equation 6.1, put forward in Wang et al. (2015).

Many sources in our sample have shown a slight issue with neighbouring sources. XMM 1, ES1 1, and ES1 2 show blending in the SERVS bands, while XMM 4, and XMM 6 show potentially multiple small sources very close together in the VIDEO bands. Looking at the postage stamp images for XMM 3 in Figure 5.5(a), we can see two sources in the optical, that merge into 1 in the VIDEO and SERVS images. If the SED at the optical wavelengths has a different object in than the NIR, it could lead to strange PDF behaviour. We note that especially for this source the optical data does not follow the best fit template, potentially due to this reason.

6.3 Star Formation Rate

The Star Formation Rate (SFR) was the next thing that was calculated for each source in our sample. As you can see from the values in Table 5.2 for SFR, our sample contains a wide range of results, with an average rate of 349^{+58}_{-66} . This is due to the varied flux values used to generate these SFRs, taken from the H1 band. Each source, except ES1 1, has a HerMES match within 5 arcseconds, however as you can see from the postage stamp images, Figure 5.1(a), 5.3(a), 5.5(a), 5.7(a), 5.9(a), 5.11(a), 5.15(a), and 5.17(a), the Far-IR images have very low resolution. It seems that from the HerMES images reliable fluxes could not be extracted as they seem to be from a combination of sources close by, as there are also multiple obvious sources in the Optical

Survey, VIDEO, and SERVS, within the same field. However the catalogues are generated based on $24\mu\text{m}$ positions taken from SPIRE photometry (Oliver et al., 2010) so are much more reliable. The catalogue based on the $24\mu\text{m}$ was the third data release from HerMES (DR3), however second release (DR2) did not include this prior and only gave 5 FIR matches. These were XMM 1, 2, 4, 6, and ES1 2. We note the 3 sources not present in DR2 do not line up with a source in the H1, H2, and H3 bands as expected. Unfortunately at the time of writing, the $24\mu\text{m}$ catalogues were not available for the ES1 and CDFS fields and therefore not presented in the postage stamp images. Higher resolution FIR data would be particularly useful for generating a reliable SFR, as we note our calculated results have large errors. $850\mu\text{m}$ data would be particularly useful as the negative K correction would mitigate the redshift uncertainty of the sources in our sample (Blain et al., 1999).

6.4 Investigation of the Usefulness of the Optical Data

Whether or not the optical data, matched with the VIDEO and SERVS data, was necessary and/or useful was explored thoroughly. We generated redshift and $z - A_V$ PDFs, both using and not using the optical data with Le Phare. Half the sources, XMM 1, XMM 2, XMM 4, and ES1 1 have only a small or no change to the calculated redshifts and extinction values. For XMM 1 there is no change between Figures 5.2(a) and 5.2(b) or between Figures 5.2(c) and 5.2(d), as with XMM 4 between Figures 5.8(a) and 5.8(b) or between Figures 5.8(c) and 5.8(d). For XMM 2, looking at the changes between Figures 5.4(a) and 5.4(b), you can see the only redshift peak shifts slightly to a lower redshift. For the $z - A_V$ PDFs for XMM 2, Figures 5.4(c) and 5.4(d), we note again that the main peak moves to a lower redshift upon the inclusion of the optical data. Finally for ES1 1, the two main redshift peaks do not change upon the inclusion of the optical fluxes, potentially due to the faintness of this source.

For the other 3 XMM sources and the second ES1 source, using the optical data with Le Phare changes the redshifts and extinctions calculated. XMM 3 appears to cause the PDF to become less constrained when using the optical data. The solitary pronounced peak around an A_V of 5 become less evident, while the area above an A_V of 8 and at $z \sim 1$ becomes more pronounced, as you can see when looking at the differences between Figures 5.6(a) and 5.6(b) and Figures 5.6(c) and 5.6(d). Looking at the changes for XMM 5, between Figures 5.10(a) and 5.10(b) and between 5.10(c) and 5.10(d), we notice a similar change, like that present in XMM 3. Potentially due to the 2 equally likely best fit templates, XMM 6 shows a lot of differences between using and not using the Optical data. Both Figures 5.12(a) and 5.12(b) have 3 peaks at $z < 2$, and looking at the differences you can see the main peak in Figure 5.12(b) at $z \sim 1.3$ shrinks, while the peaks at $z \sim 1.7$ and 0.5 increase upon the inclusion of the extra data. Finally for ES1 2, looking at Figure 5.16(b) we can see a large peak at $z \sim 1.5$ and 2 smaller peaks at $z \sim 2$, and

upon comparison to Figure 5.16(a) we see that the first peak disappears when using the optical data, whereas the 2nd and 3rd peaks increase in probability. Even though this changes the amount of prominent peaks from 1-2, we can see through comparison of Figures 5.16(c) and 5.16(d) that the $A_V - z$ space definitely becomes more constrained.

XMM 3, 5, and 6, give the most differing redshift results when we include the extra, optical data, and these are also the sources that Le Phare used the Torus Type 2 QSO template from the POLLETTA package as the best fit. As you can see from Figures 5.5(b), 5.9(b), and 5.11(b), the optical data fits the lower end of the SED well. On the other hand XMM 1 and 2 use the Type 2 QSO template from Vignali et al. (2011), with the Optical data a lot more poorly constrained (due to the poor quality of the template at UV wavelengths). Finally, XMM 4 uses the Type 2 template from POLLETTA, however the redshift is unaltered with the Optical data due to the large errors on the data, as seen towards the left of Figure 5.7(b). We therefore conclude that it is necessary to more accurately calculate redshifts for these sources, but only when an accurate template is used and the data has good SNR, especially towards the lower wavelengths. The possibility that this sample of sources contains QSOs that are highly irregular, and are poorly constrained when SED fitting is carried out with this selection of templates, has more evidence here.

Caputi et al. (2012) used 17 band photometry (U through 8.0 μm) to calculate their photometric redshifts, however they only present flux values for 6 bands, Z, J, H, Ks, 3.6 μm , and 4.5 μm for each source. The inclusion of the optical data for this work shows that Caputi et al. (2012) believed it was important in deducing redshifts, however over half the sample were undetected in Z, and were therefore undetected in the optical (due to the large red colours). Caputi et al. (2012) also presented no results for the fitting carried out with and without the optical data, so no comparison can be made here.

6.5 Extinction Laws

As discussed in §1.3, it is currently very challenging to explicitly measure the extinction law of a far away galaxy; it has only been done accurately for a few nearby galaxies. In our fitting with Le Phare, we made use of 4 laws, the Allen MW law, the Fitzpatrick LMC law, the Prevot SMC law, and the Calzetti starburst law. The best fit solutions for XMM 1, XMM 2, and the first two fits from XMM 6 and CDFS 1 gave the same χ^2 values when either the LMC or MW were used, due to the fact that these two laws are very similar, as shown in Figure 1.3, while XMM 3, 4, 5, ES1 2, and the second fits from XMM 6 and CDFS 1 used the SMC law. We note that the Type 2 QSO template from Vignali et al. (2011) exclusively uses the LMC or MW law, while the other Type 2 template from POLLETTA uses the SMC law. One thing that is important to note is that the Calzetti Law, thought to model high redshift starburst galaxies, gave the highest

χ^2 values in our analysis, and is therefore the worst of the four extinction laws used for our purposes.

Chapter 7

Simulations

7.1 Query

The final stage of this work was to examine simulations based on the Virgo Millennium Database⁹. We carried out a query for $H - B2 > 4.0$ galaxies that were sufficiently bright to be detected in SERVS (which has a limit of $2\mu Jy$ at a wavelength of $4.5\mu m$). We looked at the latest model lightcones from the Henriques simulation (Henriques et al., 2015), using the following query:

```
select c.*, g.stellarmass, g.coldgas, g.sfr, g.quasarAccretionRate,
        g.radioAccretionRate
  from Henriques2015a.cones.MRscPlanck1_<BC03 or M05>_0<Cone Number> c
    , Henriques2015a..MRscPlanck1 g
 where g.galaxyId = c.galaxyId and c.i2 < 24.0 and c.H - c.i2 > 4.0
```

where $\langle BC03 \text{ or } M05 \rangle$ was replaced with either BC03 or M05 depending on whether we chose the stellar population models from Bruzual and Charlot (2003) or those from Maraston et al. (2009). The Maraston models are generally redder due to their recipe for generating the stars, so would potentially be a better fit for our inquiry. Each set of simulations has 24 individual circular cones with a opening angle of 2 degrees, and is selected by changing $\langle \text{Cone Number} \rangle$ to numbers running from 01 to 24. As there are 24 cones with a diameter of 2 degrees, this generates a total simulation area of 75.4 deg^2 , ~ 6 times larger than the area used in our analysis. Once the query was run, we calculated a density of sources, comparing it to that determined from our work, and discussed any difference between the two values. We then explored the properties of any sources found based on our parameters.

⁹<http://gavo.mpa-garching.mpg.de/MyMillennium>

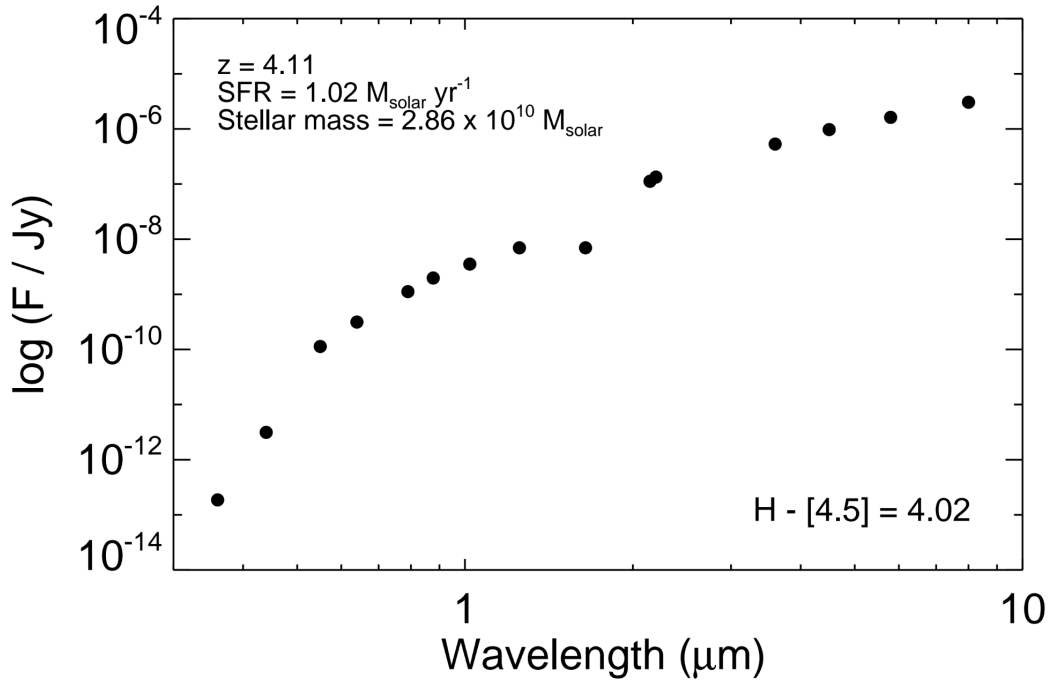


FIGURE 7.1: Spectral Energy Distribution in Flux (Jy) against Wavelength (μm) for the only galaxy extracted from simulation. The redshift (z), Star Formation Rate (SFR), Stellar mass, and $H - B2$ colour are all shown.

7.2 Findings

When we ran each of the cones with the BC03 SED models, the simulations output zero extremely red galaxies. On the other hand the Maraston templates output 1 ERG in cone 16. The galaxy has a H magnitude of 27.95 and a corresponding B2 magnitude of 23.92, which is at least 8.6 magnitudes fainter than ever source in our sample. This was a normal, extremely dusty, passive galaxy with a H-B2 colour of 4.02, a stellar mass of $2.9 \times 10^{10} M_{\odot}$, a SFR of $1.02 M_{\odot} \text{ yr}^{-1}$, and is at redshift 4.11. We note also that according to the simulation this galaxy does not have an AGN (i.e it is not a QSO). Comparing Figure 7.1, the SED for the simulated source, and our brightest source for example (XMM 3), shown in Figure 5.5(b), we do see a similar shape of the photometric flux distribution. From this result, we determine that the density of ERGs in the latest simulations is $0.013/\text{deg}^2$, which is extremely low compared to the value of $0.75/\text{deg}^2$ obtained through our analysis. Caputi et al. (2012) found a ERG density of $\sim 5.7/\text{deg}^2$, with sources at an average B2 magnitude of 22.42 ± 0.03 , which is still brighter than the only source found in the simulation. Comparing Caputi et al. (2012) to the simulation results you could conclude that the simulation databases are missing many galaxies with the colour investigated, due to the brightness of the sources found. However after the work done in this study, we can also conclude that they are missing many, bright, obscured QSOs, even though they predict at least one source ~ 5.5 magnitudes fainter than those investigated here.

Chapter 8

Conclusions

Using $1.65\mu\text{m}$ (H-band) data from the *Visible and Infrared Survey Telescope for Astronomy* (VISTA, Emerson et al., 2004) Deep Extragalactic Observations (VIDEO) survey (Jarvis et al., 2013), and $4.5\mu\text{m}$ (B2-band) data from the *Spitzer* (Werner et al., 2004) Extragalactic Representative Volume Survey (SERVS, Mauduit et al., 2012), near-IR and mid-IR surveys respectively, a sample of 9 extremely red galaxies with $H - B2$ colours greater than 4 was constructed with an average B2 magnitude of 18.67 ± 0.01 , with a maximum of 11 total wavebands (depending on the coverage available). The galaxies in the sample were ~ 3.75 magnitudes brighter than those investigated in Caputi et al. (2012), a study that used deep data from the *Hubble Space Telescope* CANDELS (Grogin et al., 2011) survey and the *Spitzer* SED (Ashby et al., 2013) survey to generate a similar sample of 17 ERGs across 17 total wavebands, with an average B2 magnitude of 22.42 ± 0.03 . The sample was matched to optical data from both the *Canada-France-Hawaii Telescope* Legacy Survey (CFHTLS) and the *European Southern Observatory* Spitzer Imaging Extragalactic Survey (ESIS, Berta et al., 2008) to increase the amount of photometric fluxes available for calculations. Using Le Phare (Arnouts et al., 1999), a Spectral Energy Distribution (SED) fitting program, the redshifts of all the sources were estimated by minimising the Chi-Squared between the photometric fluxes and a total of 127 galaxy, 53 QSO, and 18 hybrid models. The 6 brightest sources in the sample, all of which lie in the XMM field of the VIDEO survey, were found to be modelled exclusively by two QSO models, which were also used as the best fits for the source in the CDFS field. The final two sources were found in the ES1 field and are more likely to be modelled by galaxy templates. This is in contradiction to the Caputi et al. (2012) study that found all sources were galaxies, and not QSOs. In examining the Probability Density Functions (PDFs) generated, the redshifts of all the sources were found to lie below ~ 3 . More specifically 2 sources were found to lie between $0 < z < 1$, 3 sources between $1 < z < 2$, and 2 between $2 < z < 3$, with the one of the sources most likely in the first redshift sub-group and the final one equally likely to be in the second or third sub-group. This differs from the Caputi et al. (2012) study, which found that only $\sim 25\%$ of sources were at a

redshift below 3. 2-dimensional PDFs for redshift and dust extinction (A_V) were also created, and the best fit A_V values were split into 4 sub-groups. 2 sources were between $2.0 < A_V < 4.0$, 3 between $4.0 < A_V < 6.0$, 0 between $6.0 < A_V < 8.0$, and 3 at $A_V > 8.0$, with the final source either in the third or final sub-group. No sources were found to lie below and A_V value of 2. Caputi et al. (2012) also showed a wide range of extinction values for their sample of ERGs, with the highest redshift sources below $A_V \sim 1$, and many sources above $A_V \sim 5.0$. In addition to calculating the redshift and extinctions, Caputi et al. (2012) also postulated that a specific area of a colour-colour plot (specifically with colours of $H - K_s \lesssim 1.7$ and $K_s - [3.6] \gtrsim 2.1$) could be used to cut out all $H - B2 > 4$ ERGs at a redshift greater than 6. This study found that while 8 out of 9 sources in the sample lay in this area and as mentioned, none had redshifts even greater than ~ 3 . The usefulness of the optical data was investigated and found that half the sources' redshift and extinctions changed significantly upon the inclusion of the extra data, while the other half didn't change at all. It was noted that the results calculated did not change when the sources had poor signal to noise ratio (SNR) or the best fit model was of poor quality. Using far-IR data from the *Herschel* Multi-tiered Extragalactic Survey (HerMES, Oliver et al., 2012), 8 sources in the sample were found to have matches within 5 arcseconds, and a Star Formation Rate (SFR) was calculated. These rates were found to widely vary across the sample, with an average value of 360_{-58}^{+47} . A slight anti-correlation between the B2 brightness of the source and the SFR calculated was noted, mainly due to the causality relation between H1 flux and SFR. As a final step in this work was to examine Henriques et al. (2015) Simulations based on the Virgo Millennium Database. A query was carried out to extract all $H - B2 > 4.0$ sources from the database that were sufficiently bright to be detected in SERVS. It was found that the simulations generated these specific coloured ERGs with a density ~ 58 times less than that found in this work.

Chapter 9

Future Work

There are numerous exciting steps that could be done if future work was to be carried on this sample of sources. Firstly, due to the irregularity of the targets, more SED fitting would definitely be useful. This would require the use of other models, such as the Maraston set of models (Maraston et al., 2009), thought to model redder sources. The models used in this study were slightly limited towards the bluer end of the spectrum, so increasing the variety of the templates used could address this issue.

The simulation query that was carried out gave a red source with the Maraston templates but not the BC03 templates. This suggests that Thermally Pulsing Asymptotic Giant Branch (TP-AGB) stars (Rosenfield et al., 2014) may produced redder templates and influence the photometric redshifts determined. It would be of particular interest to see if our sample of sources were still found to be QSOs if the Maraston templates were used.

Secondly, Le Phare can be very useful in calculating redshifts for sources with only photometric fluxes, however as discussed it can be limited in its effectiveness. The main problem we found with this program was the maximum size of the library allowed, leading to the splitting up of our selection of templates, and therefore requiring Le Phare to be run 10 times for each catalogue of sources (for varying template packages and extinction laws). Using a different program, one that was designed to fit QSO templates rather than galaxy templates, could potentially make it much easier to carry out the SED fitting on the photometry.

Finally, unlike Caputi et al. (2012), the sources in this sample are sufficiently bright to be followed up with spectroscopy, which could either validate or contradict the redshifts determined from the SED fitting. Spectroscopy is the most reliable method of determining the true nature of sources. Future spectrographs such as The WEAVE-LOFAR Survey (Smith et al., 2016) would be particularly useful, as our sample of galaxies are most likely radio sources, due to the QSO nature and large SFRs calculated from Herschel.

Appendices


```

# 0[-def]: Energy, 1: Nb of photons
FILTER_CALIB 0 # 0[-def]: fnu=ctt
# 1 : nu.fnu=ctt
# 2 : fnu=nu
# 3 : fnu=Black Body @ T=10000K
# 4 : for MIPS (leff with nu fnu=ctt and
flux with BB @ 10000K
FILTER_FILE es1_video_spitzer_all.filt # output name of filter's file ->

#####
# THEORETICAL MAGNITUDES #
# $LEPHAREDIR/source/mag_star -c $LEPHAREDIR/config/zphot.para (star only)#
# help: $LEPHAREDIR/source/mag_star -h (or -help) #
# $LEPHAREDIR/source/mag_gal -t (Q or G) -c $LEPHAREDIR/config/zphot.para #
# (for gal. & QSO) #
# help: $LEPHAREDIR/source/mag_gal -h (or -help) #
#####
#
#----- From STELLAR LIBRARY
STAR_LIB_IN LIB_STAR # Input STELLAR LIBRARY in $LEPHAREWORK/lib_bin/
STAR_LIB_OUT STAR_VIDEO # Output STELLAR MAGN -> $LEPHAREWORK/lib_mag/
#
#----- From QSO LIBRARY
QSO_LIB_IN LIB_QSO # Input QSO LIBRARY in $LEPHAREWORK/lib_bin/
QSO_LIB_OUT QSO_VIDEO # Output QSO MAGN -> $LEPHAREWORK/lib_mag/
#
#----- From GALAXY LIBRARY
#GAL_LIB_IN LIB_BC032 # Input GAL LIBRARY in $LEPHAREWORK/lib_bin/
#GAL_LIB_OUT BC032_VIDEO1 # Output GAL LIBRARY -> $LEPHAREWORK/lib_mag/
#GAL_LIB_IN LIB_CWV # Input GAL LIBRARY in $LEPHAREWORK/lib_bin/
#GAL_LIB_OUT CWV_VIDEO # Output GAL LIBRARY -> $LEPHAREWORK/lib_mag/
#GAL_LIB_IN LIB_AVEROIN # Input GAL LIBRARY in $LEPHAREWORK/lib_bin/
#GAL_LIB_OUT AVEROIN_VIDEO1 # Output GAL LIBRARY -> $LEPHAREWORK/lib_mag/
#GAL_LIB_IN LIB_POLLETTA # Input GAL LIBRARY in $LEPHAREWORK/lib_bin/
#GAL_LIB_OUT POLLETTA_VIDEO # Output GAL LIBRARY -> $LEPHAREWORK/lib_mag/
#GAL_LIB_IN LIB_QSO
#GAL_LIB_OUT QSO_VIDEO1
#
#----- MAG + Z_STEP + EXTINCTION + COSMOLOGY
MAGTYPE AB # Magnitude type (AB or VEGA)
Z_STEP 0.1,8.,0.1 # dz, zmax, dzsup(if zmax>6)
COSMOLOGY 70,0.3,0.7 # H0,om0,lbd0 (if lb0>0->om0+lbd0=1)
MOD_EXTINC 0,26,0,26 # model range for extinction
EXTINC_LAW LMC_Fitzpatrick.dat,MW_Allen.dat # ext. law (in $LEPHAREDIR/ext/*)
#EXTINC_LAW LMC_Fitzpatrick.dat,MW_Allen.dat,calzetti.dat,SMC_prevot.dat
# ext. law (in $LEPHAREDIR/ext/*)
EB_V 0.0,0.05,0.1,0.15,0.2,0.25,0.3,0.35,0.4,0.45,0.5,0.55,0.6,
0.65,0.7,0.75,0.8,0.85,0.9,0.95,1.0,1.05,1.1,1.15,1.2,1.25,1.3,1.35,
1.4,1.45,1.5,1.55,1.6,1.65,1.7,1.75,1.8,1.85,1.9,1.95,2.0,2.05,2.1,
2.15,2.2,2.25,2.3
# E(B-V) (<50 values)
EM_LINES YES
# Z_FORM 8,7,6,5,4,3 # Zformation for each SED in GAL_LIB_IN
#
#----- ASCII OUTPUT FILES OPTION

```

```

LIB_ASCII      YES          # Writes output in ASCII
                                # in working directory

#
#####
#          PHOTOMETRIC REDSHIFTS          #
# $LEPHAREDIR/source/zphot -c $LEPHAREDIR/config/zphot.para          #
# help: $LEPHAREDIR/source/zphot -h (or -help)          #
#####
#
#
#-----      Input Catalog Informations
CAT_IN        $LEPHAREWORK/xmm/esiall.in # Input catalog (full path)
INP_TYPE      F              # Input type      (F:Flux or M:MAG)
CAT_MAG       AB            # Input Magnitude (AB or VEGA)
CAT_FMT       MEME          # MEME: (Mag,Err)i
                                # MME: (Mag)i,(Err)i
CAT_LINES     1,100000      # MIN and MAX RANGE of ROWS used in input cat [def:-99,-99]
CAT_TYPE      LONG          # Input Format      (LONG,SHORT-def)
CAT_OUT       $LEPHAREWORK/xmm/zphot.out # Output catalog (full path)
PARA_OUT      $LEPHAREDIR/config/zphot_output.para # Ouput parameter (full path)
#
BD_SCALE      0              # Bands used for scaling
                                # (Sum 2^n; n=0->nbd-1, 0[-def]:all bands)
GLB_CONTEXT   -1            # Overwrite Context (Sum 2^n; n=0->nbd-1,
                                # 0      : all bands used,
                                # -1[-def]: used context per object
# FORB_CONTEXT -1          # context for forbidden bands
ERR_SCALE     0.1,0.1,0.1,0.1,0.1,0.1,0.1,0.1,0.1,0.1,0.1,0.1 # errors per band added in quadrature
#ERR_FACTOR   1.5          # error scaling factor 1.0 [-def]
#
#-----      Theoretical libraries
ZPHOTLIB      POLLETTA_VIDEO # Library used for Chi2 (max:3)
ADD_EMLINES   YES
#
#####      PHOTOMETRIC REDSHIFTS OPTIONS      #####
# FIR LIBRARY
FIR_LIB       NONE
FIR_LMIN      7.0           # Lambda Min (micron) for FIR analysis
FIR_CONT      -1
FIR_SCALE     -1
FIR_FREESCALE YES          # ALLOW FOR FREE SCALING
FIR_SUBSTELLAR NO
# PHYSICAL LIBRARY with Stochastic models from BC07
PHYS_LIB      NONE
PHYS_CONT     -1
PHYS_SCALE    -1
PHYS_NMAX     100000
#
#-----      Priors
# MASS_SCALE   6.,16.       # Lg(Scaling) min,max [0,0-def]
MAG_ABS       -10.,-26.    # Mabs_min , Mabs_max [0,0-def]
MAG_REF       4            # Reference number for band used by Mag_abs
# ZFORM_MIN    5,5,5,5,5,3,1 # Min. Zformation per SED -> Age constraint
Z_RANGE       0.,99.99     # Z min-max used for the Galaxy library

```

```

EBV_RANGE      0,2,3          # E(B-V) MIN-MAX RANGE of E(B-V) used
# NZ_PRIOR     4,2,4          # I Band for prior on N(z)
#
#-----      Fixed Z   (need format LONG for input Cat)
ZFIX           NO           # fixed z and search best model [YES,NO-def]
#
#-----      Parabolic interpolation for Zbest
Z_INTERP      YES          # redshift interpolation [YES,NO-def]
#
#-----      Analysis of normalized ML(exp-(0.5*Chi^2)) curve
#-----      Secondary peak analysis
DZ_WIN        0.5          # Window search for 2nd peaks [0->5;0.25-def]
MIN_THRES     0.1          # Lower threshold for 2nd peaks[0->1; 0.1-def]
#
#-----      Probability (in %) per redshift intervals
# PROB_INTZ    0,0.5,0.5,1.,1.,1.5  # even number
#
#####      ABSOLUTE MAGNITUDES COMPUTATION      #####
#
MABS_METHOD 1      # 0[-def] : obs->Ref
                  # 1 : best obs->Ref
                  # 2 : fixed obs->Ref
                  # 3 : mag from best SED
                  # 4 : Zbin
MABS_CONTEXT    -1          # CONTEXT for Band used for MABS

MABS_REF        4          # 0[-def]: filter obs chosen for Mabs :
                  # ONLY USED IF MABS_METHOD=2
MABS_FILT       1,2,3,4    # Chosen filters per redshift bin (MABS_ZBIN)
                  # ONLY USED IF MABS_METHOD=4
MABS_ZBIN       0,0.5,1,1.5,2,3,3.5,4 # Redshift bins (even number)
                  # ONLY USED IF MABS_METHOD=4
#####      OUTPUT SPECTRA      #####
#
SPEC_OUT       YES        # spectrum for each object? [YES,NO-def]
CHI2_OUT       YES        # output file with all values : z,mod,chi2,E(B-V),...
                  # BE CAREFUL can take a lot of space !!

#####      OUTPUT PDZ ANALYSIS
PDZ_OUT        NONE       # pdz output file name [def-NONE]
                  # add automatically PDZ_OUT[.pdz/.mabsx/.mod/.zph]
PDZ_MABS_FILT  2,10,14    # MABS for REF FILTERS to be extracted
#
#####      FAST MODE : color-space reduction      #####
#
FAST_MODE      NO         # Fast computation [NO-def]
COL_NUM        3         # Number of colors used [3-def]
COL_SIGMA      3         # Enlarge of the obs. color-errors[3-def]
COL_SEL        AND       # Combination between used colors [AND/OR-def]
#
#####      MAGNITUDE SHIFTS applied to libraries  #####
#
# APPLY_SYSSHIFT 0.       # Apply systematic shifts in each band
                        # used only if number of shifts matches
                        # with number of filters in the library
#

```

```
##### ADAPTIVE METHOD using Z spectro sample   ###
#
AUTO_ADAPT NO      # Adapting method with spectro [NO-def]
ADAPT_BAND 4,2,4   # Reference band, band1, band2 for color
ADAPT_LIM 18,22.0 # Mag limits for spectro in Ref band [18,21.5-def]
ADAPT_POLY 1      # Number of coef in polynom (max=4) [1-def]
ADAPT_METH 1      # Fit as a function of
                  # 1 : Color Model [1-def]
                  # 2 : Redshift
                  # 3 : Models
ADAPT_CONTEXT -1  # Context for bands used for training
                  # -1[-def] used context per object
ADAPT_ZBIN 0.01,6 # Redshift's interval used for training
                  # [0.001,6-Def]
ADAPT_MODEBIN 1,1000 # Model's interval used for training
                  # [1,1000-Def]
ERROR_ADAPT NO    # [YES,NO-def]
                  # Add error in quadrature according to
                  # the difference between observed
                  # and predicted apparent magnitudes
```

Bibliography

- Acquaviva, V., Raichoor, A., and Gawiser, E., 2015. Simultaneous estimation of photometric redshifts and sed parameters: Improved techniques and a realistic error budget. *The Astrophysical Journal*, 804(1):8.
- Allen, C.W., 1976. Astrophysical quantities.
- Arnouts, S., Cristiani, S., Moscardini, L., et al., 1999. Measuring and modelling the redshift evolution of clustering: the hubble deep field north. *Monthly Notices of the Royal Astronomical Society*, 310:540.
- Ashby, M.L.N., Willner, S.P., Fazio, G.G., et al., 2013. Seds: The spitzer extended deep survey. survey design, photometry, and deep irac source counts. *The Astrophysical Journal*, 769(1):80.
- Becker, R.H., Fan, X., White, R.L., et al., 2001. Evidence for reionization at $z \approx 6$: Detection of a Gunn-Peterson trough in a $z=6.28$ quasar. *The Astronomical Journal*, 122(6):2850.
- Berta, S., Rubele, S., Franceschini, A., et al., 2008. VizieR online data catalog: Esis bvr catalog, elais-s1 (berta+, 2006). *VizieR Online Data Catalog*, 345.
- Blain, A.W., Smail, I., Ivison, R.J., et al., 1999. The history of star formation in dusty galaxies. *Monthly Notices of the Royal Astronomical Society*, 302.
- Bruzual, G. and Charlot, S., 2003. Stellar population synthesis at the resolution of 2003. *Monthly Notices of the Royal Astronomical Society*, 344(4):1000.
- Calzetti, D., Armus, L., Bohlin, R.C., et al., 2000. The dust content and opacity of actively star-forming galaxies. *The Astrophysical Journal*, 533(2):682.
- Calzetti, D., Harris, J., Gallagher, John S., I., et al., 2004. The ionized gas in local starburst galaxies: Global and small-scale feedback from star formation. *The Astronomical Journal*, 127:1405.

- Calzetti, D., Kinney, A.L., and Storchi-Bergmann, T., 1994. Dust extinction of the stellar continua in starburst galaxies: The ultraviolet and optical extinction law. *The Astrophysical Journal*, 429:582.
- Caputi, K.I., Dunlop, J.S., McLure, R.J., et al., 2012. The nature of extremely red $h-[4.5]$ galaxies revealed with SEDs and CandelS. *The Astrophysical Journal*, 750(1):L20.
- Chabrier, G., 2003. Galactic stellar and substellar initial mass function. *Publications of the Astronomical Society of the Pacific*, 115(809):763.
- Chen, B.Q., Liu, X.W., Yuan, H.B., et al., 2014. A three dimensional extinction map of the galactic anticentre from multi-band photometry. *Monthly Notices of the Royal Astronomical Society*, 443(2):1192.
- Coleman, G.D., Wu, C.C., and Weedman, D.W., 1980. Colors and magnitudes predicted for high redshift galaxies. *The Astrophysical Journal Supplement Series*, 43:393.
- Cristiani, S., Alexander, D.M., Bauer, F., et al., 2004. The space density of high-redshift QSOs in the GOODS survey. *The Astrophysical Journal*, 600(2):L119.
- Daddi, E., Cimatti, A., Renzini, A., et al., 2004. A new photometric technique for the joint selection of star-forming and passive galaxies at $1.4 < z < 2.5$. *The Astrophysical Journal*, 617(2):746.
- Dickinson, M., Giavalisco, M., and Team, G., 2003. The great observatories origins deep survey. page 324. eprint: arXiv:astro-ph/0204213.
- Dunlop, J.S., 2013. Observing the first galaxies. *arXiv:1205.1543 [astro-ph]*, 396:223.
- Emerson, J.P., Sutherland, W.J., McPherson, A.M., et al., 2004. The visible & infrared survey telescope for astronomy. *The Messenger*, 117:27.
- Fitzpatrick, E.L., 1986. An average interstellar extinction curve for the large magellanic cloud. *The Astronomical Journal*, 92:1068.
- Franx, M., Labbe, I., Rudnick, G., et al., 2003. A significant population of red, near-IR selected high redshift galaxies. *The Astrophysical Journal*, 587(2):L79.
- Gordon, K.D., Clayton, G.C., Misselt, K.A., et al., 2003. A quantitative comparison of SMC, LMC, and Milky Way UV to NIR extinction curves. *The Astrophysical Journal*, 594(1):279.
- Grogin, N.A., Kocevski, D.D., Faber, S.M., et al., 2011. CandelS: The cosmic assembly near-infrared deep extragalactic legacy survey. *The Astrophysical Journal Supplement Series*, 197(2):35.
- Helou, G., 1986. The IRAS colors of normal galaxies. *The Astrophysical Journal Letters*, 311:L33.

- Henriques, B., Thomas, P., Oliver, S., et al., 2009. Monte carlo markov chain parameter estimation in semi-analytic models of galaxy formation. *Monthly Notices of the Royal Astronomical Society*, 396(1):535.
- Henriques, B.M.B., White, S.D.M., Thomas, P.A., et al., 2015. Galaxy formation in the planck cosmology - i. matching the observed evolution of star formation rates, colours and stellar masses. *Monthly Notices of the Royal Astronomical Society*, 451(3):2663.
- Hook, I.M., Shaver, P.A., and McMahon, R.G., 1998. The evolution of radio-loud quasars at high redshift. *arXiv:astro-ph/9801213*.
- Hwang, H.S. and Geller, M.J., 2013. Dust-obscured galaxies in the local universe. *The Astrophysical Journal*, 769(2):116.
- Ilbert, O., Arnouts, S., McCracken, H.J., et al., 2006. Accurate photometric redshifts for the cfht legacy survey calibrated using the vimos vlt deep survey. *Astronomy and Astrophysics*, 457:841.
- Jarvis, M.J., Bonfield, D.G., Bruce, V.A., et al., 2013. The vista deep extragalactic observations (video) survey. *Monthly Notices of the Royal Astronomical Society*, 428:1281.
- Kauffmann, G., Heckman, T.M., Tremonti, C., et al., 2003. The host galaxies of agn. *Monthly Notices of the Royal Astronomical Society*, 346(4):1055.
- Kennicutt, Robert C., J., 1998. The global schmidt law in star-forming galaxies. *The Astrophysical Journal*, 498:541.
- Kessler, M.F., Steinz, J.A., Anderegg, M.E., et al., 1996. The infrared space observatory (iso) mission. *Astronomy and Astrophysics*, 315:L27.
- Kinney, A.L., Calzetti, D., Bohlin, R.C., et al., 1996. Template ultraviolet to near-infrared spectra of star-forming galaxies and their application to k-corrections. *The Astrophysical Journal*, 467:38.
- Kroese, D.P., Brereton, T., Taimre, T., et al., 2014. Why the monte carlo method is so important today. *Wiley Interdisciplinary Reviews: Computational Statistics*, 6(6):386.
- Laher, R.R., Gorjian, V., Rebull, L.M., et al., 2012. Aperture photometry tool. *Publications of the Astronomical Society of the Pacific*, 124(917):737.
- Lawrence, A., Warren, S.J., Almaini, O., et al., 2007. The ukirt infrared deep sky survey (ukidss). *Monthly Notices of the Royal Astronomical Society*, 379(4):1599.
- Maraston, C., Stromback, G., Thomas, D., et al., 2009. Modeling the color evolution of luminous red galaxies - improvements with empirical stellar spectra. *Monthly Notices of the Royal Astronomical Society: Letters*, 394(1):L107.

- Mauduit, J.C., Lacy, M., Farrah, D., et al., 2012. The spitzer extragalactic representative volume survey (servs): survey definition and goals. *Publications of the Astronomical Society of the Pacific*, 124(917):714.
- Netzer, H., Lutz, D., Schweitzer, M., et al., 2007. Spitzer quasar and ulirg evolution study (quest): ii. the spectral energy distributions of palomar-green quasars. *The Astrophysical Journal*, 666(2):806.
- Oke, J.B. and Gunn, J.E., 1983. Secondary standard stars for absolute spectrophotometry. *The Astrophysical Journal*, 266:713.
- Oliver, S., Frost, M., Farrah, D., et al., 2010. Specific star formation and the relation to stellar mass from $0 < z < 2$ as seen in the far-infrared at 70 and 160 μm . *Monthly Notices of the Royal Astronomical Society*, 405.
- Oliver, S.J., Bock, J., Altieri, B., et al., 2012. The herchel multi-tiered extragalactic survey: Hermes. *Monthly Notices of the Royal Astronomical Society*, 424(3):1614.
- Pearson, E.A., Eales, S., Dunne, L., et al., 2013. H-atlas: estimating redshifts of herchel sources from sub-mm fluxes. *Monthly Notices of the Royal Astronomical Society*, 435(4):2753.
- Pierre, M., Lidman, C., Hunstead, R., et al., 2001. The first iso ero: a dusty quasar at $z = 1.5$. *Astronomy and Astrophysics*, 372(3):L45.
- Polletta, M., Tajer, M., Maraschi, L., et al., 2007. Spectral energy distributions of hard x-ray selected active galactic nuclei in the extlessi extgreaterxmm-newton extless/i extgreater medium deep survey. *The Astrophysical Journal*, 663(1):81.
- Polletta, M., Wilkes, B.J., Siana, B., et al., 2006. Chandra and spitzer unveil heavily obscured quasars in the swire/chandra survey. *The Astrophysical Journal*, 642(2):673.
- Pound, R.V. and Rebka, G.A., 1960. Apparent weight of photons. *Physical Review Letters*, 4:337.
- Pozzetti, L. and Mannucci, F., 2000. Extremely red galaxies: age and dust degeneracy solved ? *Monthly Notices of the Royal Astronomical Society*, 317(1):L17.
- Prevot, M.L., Lequeux, J., Maurice, E., et al., 1984. The typical interstellar extinction in the small magellanic cloud. *Astronomy and Astrophysics*, 132.
- Rosenfield, P., Marigo, P., Girardi, L., et al., 2014. Evolution of thermally pulsing asymptotic giant branch stars. iv. constraining mass loss and lifetimes of low mass, low metallicity agb stars. *The Astrophysical Journal*, 790(1):22.
- Rowan-Robinson, M., Babbedge, T., Oliver, S., et al., 2008. Photometric redshifts in the swire survey. *Monthly Notices of the Royal Astronomical Society*, 386:697.

- Salvato, M., Hasinger, G., Ilbert, O., et al., 2009. Photometric redshift and classification for the xmm-cosmos sources. *The Astrophysical Journal*, 690(2):1250.
- Seaton, M.J., 1979. Interstellar extinction in the uv. *Monthly Notices of the Royal Astronomical Society*, 187(1):73P.
- Serjeant, S., 2010. *Observational Cosmology*. Cambridge University Press.
- Smith, D.J.B., Best, P.N., Duncan, K.J., et al., 2016. The weave-lofar survey.
- Taylor, M.B., 2005. Topcat & stil: Starlink table/votable processing software. volume 347, page 29.
- Tremonti, C.A., Heckman, T.M., Kauffmann, G., et al., 2004. The origin of the mass-metallicity relation: Insights from 53,000 star-forming galaxies in the sloan digital sky survey. *The Astrophysical Journal*, 613(2):898.
- Vignali, C., Piconcelli, E., Lanzuisi, G., et al., 2011. On the nature of the absorber in iras 09104+4109: the x-ray and mid-infrared view: An x-ray and mid-ir view of iras 09104+4109. *Monthly Notices of the Royal Astronomical Society*, 416(3):2068.
- Walborn, N.R., 1990. Contemporary optical spectral classification of the ob stars: A digital atlas. *Publications of the Astronomical Society of the Pacific*, 102(650):379.
- Wang, T., Elbaz, D., Schreiber, C., et al., 2015. Infrared color selection of massive galaxies at z extgreater 3. *arXiv:1512.02656 [astro-ph]*.
- Werner, M.W., Roellig, T.L., Low, F.J., et al., 2004. The spitzer space telescope mission. *The Astrophysical Journal Supplement Series*, 154:1.
- Wolf, C., Dye, S., Kleinheinrich, M., et al., 2001. Deep bvr photometry of the chandra deep field south from the combo-17 survey. *Astronomy and Astrophysics*, 377(2):442.
- Xiang, F.Y., Li, A., and Zhong, J.X., 2011. A tale of two mysteries in interstellar astrophysics: The 2175 angstrom extinction bump and diffuse interstellar bands. *The Astrophysical Journal*, 733(2):91.